Traceable low-current measurements towards the realisation of the ampere in the new SI

Doctoral Dissertation
Doctoral Program in Metrology (31st cycle)

Traceable low-current measurements towards the realisation of the ampere in the new SI

Ilaria Finardi

* * * * * *

Supervisors
Luca Callegaro, Supervisor
Massimo Ortolano, Co-supervisor

Doctoral examination committee
Dr. Stephen Giblin, Referee, National Physical Laboratory, Teddington, England
Dr. Martin Götz, Referee, Physikalisch-Technische Bundesanstalt, Braunschweig, Germany
Prof. Salvatore Baglio, Università degli Studi di Catania, Catania, Italy
Dr. Emanuele Enrico, Istituto Nazionale di Ricerca Metrologica, Torino, Italy
Dr. François Piquemal, Laboratoire National de Métrologie et d'essais, Paris, France

Politecnico di Torino
August 1, 2019

I hereby declare that the contents and organisation of this dissertation constitute my own original work and does not compromise in any way the rights of third parties, including those relating to the security of personal data.

Ilaria Finardi
Turin, August 1, 2019

Summary

This work is focused on DC low current measurements in the frame of the new International System of Units (SI). All the units of new SI, that will be implemented starting from the 20 May 2019, are based on fundamental constants of nature. The new definition of the ampere is based on the assignment of an exact value to the elementary charge e. Single-electron devices are a possible realization of this new definition due to their ability to transfer an integer number of charges in a controlled way.

Transresistance amplifiers are commonly employed to measure the current produced by single-electron devices, which is usually below the nanoampere level. In this dissertation two amplifiers are investigated: the commercial FEMTO DDPCA-300 and the advanced Ultrastable Low-noise Current Amplifier (ULCA).

The FEMTO DDPCA-300, embedded in a simple temperature control system, achieves a resolution around 15 times better than the uncontrolled case. The amplifier gain is calibrated by using a set-up which employs the capacitance-charging method, achieving an accuracy of the order of 10^{-5}. The set-up is especially design and built for the calibration of transresistance amplifiers with currents in the range from 100 fA to 100 pA.

On the other hand, the resolution of the ULCA can be enhanced by a factor of around four by shielding it in a Mu-metal box. By using a 14 bit cryogenic current comparator (CCC), the overall transresistance gain of the ULCA can be calibrated with a relative uncertainty in the 10^{-8} range.

The final part of this dissertation is dedicated to the work done in the measurement of a single-electron pump, based on GaAs/AlGaAs heterostructure, generating a nominal current of 100 pA. New features of the experimental set-up are introduced in order to perform a high accuracy measurement. The outcome of a 16 hours measurement is presented: the current produced by the pump is measured with a preliminary accuracy of 9×10^{-8}. This result, which is beyond the state of the art, is a big step towards the adoption of single-electron pumps as quantum current standards.

Acknowledgements

I would like to express my appreciation to my supervisor, Luca Callegaro, for the planning and the development of my work through these years.

I am also particularly grateful to my co-supervisor, Massimo Ortolano, for all the fruitful discussions and for supporting me patiently during the writing of this dissertation.

Thanks to Emanuele Enrico and Luca Croin for their collaboration during the years of research in INRiM. The technical assistance of Vincenzo D'Elia and Danilo Serazio was also very important for the realization of many ideas contained in these pages.

I would like to offer my special acknowledgements to the PTB colleagues I met in Braunschweig: Franz Josef Ahlers, Hans Werner Schumacher, Hansjörg Scherer, Martin Götz, Eckart Pesel, Niels Ubbelohde, Dario Maradan and Thomas Gerster.

As a friend more than a colleague, I would like to thank Jonas Herick for the great time we spent together.

Finally, I would like to thank all my loved ones who always believed in me and supported me everyday in this journey.

To M...

Contents

List of Tables

List of Figures

Preface

The work presented in this dissertation was carried out in two different national metrology institutes: the Istituto Nazionale di Ricerca Metrologica (INRiM), Turin, Italy, and the Physikalisch-Technische Bundesanstalt (PTB), Braunschweig, Germany.

In fact, between September 2017 and June 2018, I had the opportunity to work as a guest researcher at the PTB headquarters in Braunschweig. In particular, I spent the first three months with the Department of Electrical Quantum Metrology and the remaining six with the Department of Semiconductor Physics and Magnetism.

The dissertation reports in chapter 1 a brief overview of the electrical units in the frame of the new International System of Units, finally approved in November 2018. In the same chapter, it is also included a description of one of the most important metrological experiments: the Quantum Metrology Triangle (QMT).

Chapter 2 introduces three common techniques for the measurement of DC low currents: the transresistance amplifier, the voltage-resistance method and the cryogenic current comparator.

Chapter 3 describes two specific models of transresistance amplifiers: the FEMTO DDPCA-300 and the Ultrastable Low-noise Current Amplifier (ULCA). The same chapter also presents the results of a noise characterization that I performed on the two amplifiers. The FEMTO amplifier was placed in a temperature control system specifically developed and built to improve its offset stability. The results have been published in [23]. The ULCA was shielded in different configurations to find the one yielding the minimum noise and interference contribution coming from the external environment. The results obtained with this analysis were exploited to integrate two ULCAs in the set-up for the single-electron experiment described in chapter 6.

Chapter 4 presents the calibration procedure of the amplifiers. The FEMTO was calibrated by means of a purpose-built system that I studied and developed during the first years of research at INRiM. This system employs the capacitance-charging method: this work and its results have been published in [136, 141]. They

were also the subject of a talk delivered at the conference URSI 2017[1], allowing me to win the Young Scientist Award 2017. For what concerns the ULCA, I attended to its calibration by using the 14 bit cryogenic current comparator located in the PTB laboratories.

Chapter 5 is dedicated to the single-parameter pumping process of a GaAs-based single-electron pump used in the experiment described in following chapter.

All chapter 6 is addressed to the work done in the implementation of the single-electron experiment. First of all, an overview of the entire experiment is provided: the set-up includes two standard ULCAs and two Programmable Josephson Voltage Standards (PJVSs) to perform a potentiometric measurement of the ULCAs output voltages.

Then, the new features of the experiment are described: the so-called *cross-switch chip* and the cabling system of the cryogenic probe employed to measure the pump. This cabling system was specifically designed to perform high accuracy measurements of the current produced by single-electron pumps. I was deeply involved both in the construction and in the characterization of this new system.

The chapter finally presents an analysis of the resolution of the measurement, which shows an improvement over the state of the art. For what concerns my role in this analysis, I developed the Matlab software used for the data analysis and interpreted the results.

[1] XXXII International Union of Radio Science and General Assembly and Scientific Symposium in Montréal, Canada, 23 August 2017.

Chapter 1

Electrical units in the old and new SI

The International System of Units (Système international d'unités, SI) is founded on seven base units: metre, kilogram, second, ampere, kelvin, mole and candela, which correspond to the base quantities of length, mass, time, electric current, thermodynamic temperature, amount of substance and luminous intensity.

Since its formal adoption in 1960 by the 11th Conference on Weights and Measures (Conférence générale des poids et mesures, CGPM), the SI has provided consistency and uniformity in measurements [156].

Thanks to great scientific and technological efforts done by the National Metrology Institutes (NMIs), the definitions of the units have been changed over the years, leading to considerable improvements both in accuracy and reproducibility.

With the aim of further improving the realization accuracy of the units, on 16 November 2018, during the 26th CGPM, a revision of the SI was unanimously approved. This revision will be implemented on 20 May 2019 [150].

In this new SI, whose schematic representation is reported in figure 1.1, the definitions of the units are established on the exact values of certain fundamental constants, that is, with no uncertainty, bringing to an end the era of using physical artefacts to define measurement units, including the kilogram at last.

In fact, until the implementation of the new SI, the definition of the kilogram has remained unchanged since its adoption in 1889: the kilogram being the last base unit based on an artefact as a consequence.

Since 1889 the international prototype kilogram has been kept in Sèvres, where the International Bureau of Weights and Measures (Bureau international des poids et mesures, BIPM) is located. Unfortunately, this artefact is susceptible to change its mass over time [168, 171, 169, 170] and its instability spreads among other SI units whose definition depends on the kilogram such as, for instance, the ampere.

The ampere is the electrical base unit of the SI and its current definition is based on the kilogram through the derived unit newton:

Figure 1.1: Representation of the seven base units and their corresponding fundamental constants in the new SI, from [160].

> The ampere is that constant current which, if maintained in two straight parallel conductors of infinite length, of negligible circular cross-section, and placed 1 m apart in vacuum, would produce between these conductors a force equal to 2×10^{-7} newton per metre of length. [152]

This definition is unsatisfactory because suffers from the drift and the changes of the international prototype over the time and because it is difficult to realize with an accuracy acceptable for the contemporary and future metrology. In fact, until now, the realization of the ampere is possible only in an indirect way by combining the realizations of other units as the watt, the ohm, and the volt [39]. However, the limitation on the accuracy of the realization of the volt limits also that of the indirect realization of the ampere to around 3×10^{-7} [78, 79].

The new definition of the kilogram will be instead based on the fixed value of the Planck constant h with zero uncertainty assigned. The definition of the ampere in the new SI will be based on the elementary charge e, also considered without uncertainty, as follows:

> The ampere, symbol A, is the SI unit of electric current. It is defined by taking the fixed numerical value of the elementary charge e to be $1.602\,176\,634 \times 10^{-19}$ when expressed in the unit C, which is equal to A s, where the second is defined in terms of $\Delta\nu_{\mathrm{Cs}}$. [149]

One of the proposed realizations of this new definition employs single-electron devices [153] which, finally, allows the realization of the ampere in a direct way. In fact, single-electron devices are able to transport a number n of elementary charges e with a frequency f, thus producing an ideal current nef.

However, the requirements for realizing a quantum current standard for primary metrology demand that the magnitude of the current generated to be reasonably high, 100 pA or greater, to achieve enough resolution, and a total relative counting

error of 10^{-7} or smaller, in order to replace the realization of the ampere through the combinations of the realizations of the watt, ohm and volt [157].

Among the most promising candidates to realize the new ampere, there are the so-called single-electron turnstiles and the single-electron pumps: the former demand a voltage bias to operate, whereas the latter do not. These devices can be realized either with metal-oxide or semiconductor-based nano-structure: in both cases, the pumping principle is based on the tunnelling of the electrons through tunnel barriers combined with the *Coulomb blockade* effect (further discussions in [24, 40]).

Despite good results obtained with metal-oxide pumps in the electron transfer accuracy [65, 63], they are limited in the operating frequency (and thus in the current output level) due to their fixed tunnel barrier height. On the other hand, in semiconductor-based pumps, the tunnel barriers can be created electrostatically by applying external voltages to gates [28].

Initially, semiconductor-based pumps demonstrated quantized currents with driving frequencies up to 1 GHz [155] by tuning the height of the barriers surrounding a quantum dot. Later, it was proved that a quantized current could be generated by modulating just one of the barriers, performing the so-called *single-parameter pumping* [32, 115]. This technique turned out to be a remarkable improvement towards the realization of a quantum current standard with high output current, allowing parallelization of multiple pumps [71].

Thus, two decades of scientific efforts in combining both high current output and accuracy have brought the current produced close to the target [45]: semiconductor-based pumps have shown a relative uncertainty of 1.6×10^{-7} for a current of 96 pA [121] and 2.7×10^{-7} for 160 pA [13]. For what concerns the metallic hybrid turnstile [77], also driven by high-frequency modulation of only one gate electrode [72, 73], their parallelization produced a maximum value of 170 pA [54], while the best relative uncertainty is at the level of 1×10^{-4} [55]. Hence, the possibility to establish a quantum current standard based on single-electron transport (SET) effect has now gained prominence. The advantage to having a quantum current standard will also reduce the uncertainty on low-current measurements which are involved in several industrial and medical applications.

In the field of electrical metrology, the new SI will also bring the improvement of the units volt and ohm. Since the 1980s, the development of the Josephson voltage standard (JVS, see appendix A) and of the quantum Hall resistance (QHR) standard has allowed the reproducibility of voltage and resistance with an uncertainty better than parts in 10^9 [52] [24, Ch. 4], which is orders of magnitude better than the corresponding realization uncertainties of the SI units of volt and ohm. The realization of the SI volt can be achieved by means of a mercury electrometer [78] or by a voltage balance [79]: in both cases, total relative uncertainties of 2.7×10^{-7} were obtained. For what concerns the realization of the SI ohm, a total relative uncertainty of 2×10^{-8} was achieved by employing the Thompson-Lampard calculable

capacitor [37, 80].

To keep uniformity among the reference standards and to benefit from the exceptional reproducibility of the Josephson effect and quantum Hall effect, in 1988, the International Committee for Weights and Measures (Comité international des poids et mesures, CIPM) endorsed the best experimental data available at the time for K_{J} and R_{K}, as agreed-upon values to be employed starting from 1st January 1990 [164] for the evaluation of Josephson and quantum Hall measurements [162]. These conventional values were denoted as $K_{\text{J-90}}$ and $R_{\text{K-90}}$, respectively:

$$K_{\text{J-90}} = 483\,597.9\,\mathrm{GHz/V} \tag{1.1}$$

$$R_{\text{K-90}} = 25\,812.807\,\Omega. \tag{1.2}$$

By means of $K_{\text{J-90}}$ and $R_{\text{K-90}}$ it was possible to obtain reproducible scales for voltage and resistance: voltage V_{90} and resistance R_{90} as

$$V_{90} = \frac{k f_{\mathrm{J}}}{K_{\text{J-90}}} \tag{1.3}$$

$$R_{90} = \frac{R_{\text{K-90}}}{i}, \tag{1.4}$$

where k and f_{J} are the step number and the Josephson operating frequency for V_{90} respectively, while i is the quantum Hall effect plateau number.

The introduction of $K_{\text{J-90}}$ and $R_{\text{K-90}}$ embodies the big dilemma of the modern electrical metrology because it created units outside the SI. Over time, new and more accurate determinations of K_{J} and R_{K} created a discrepancy between the conventional values and the SI values which in 2017 was 106.665×10^{-9} in case of the volt and 17.793×10^{-9} for the resistance [153].

With the new SI based on the exact values of h and e, also K_{J} and R_{K} will be exact: the JVS and QHR become realizations of the SI units volt and ohm, respectively. The conventional values $K_{\text{J-90}}$ and $R_{\text{K-90}}$ will be abolished.

1.1 Quantum Metrology Triangle

Due to the metrological importance of the JVS, QHR standard and quantum current standard, a consistency test called *Quantum Metrology Triangle* (QMT), was proposed for the first time in 1985 [167]. The purpose of QMT is to determine possible experimental corrections to the constituting relations at the base of the standards.

Figure 1.2 gives a pictorial representation of the QMT: the test consists of the combination of the Josephson, the quantum Hall and the single-electron transport effects by means of Ohm's law. In particular, the quantities involved in the QMT are

shown at the vertices of a triangle, while the edges represent the effects linking one quantity to another. The voltage generated by the Josephson effect, the quantized

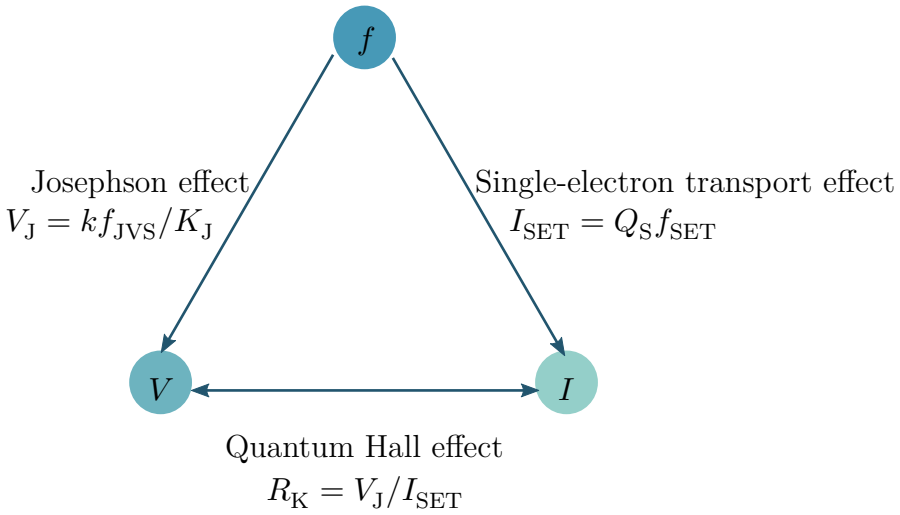

Figure 1.2: A symbolic representation of the QMT: the Josephson, the quantum Hall and the single-electron transport effects are linked via the Ohm's law.

Hall resistance and the current generated by single-electron counting are combined.

The constitutive relations of the three quantum standards can be written acknowledging possible deviations from idealities. The constants K_J, R_K, and Q_S (representing the charge quanta) are considered as empirical quantities to be determined experimentally. For each of them, the quantities ε_J, ε_K, and ε_S parametrize these deviations. Therefore, the constitutive relations of the quantum electrical standards can be expressed as

(i) A JVS driven at frequency f_J and operating on the kth step generates the voltage

$$V_{JVS} = kf_J/K_J \tag{1.5}$$

with

$$K_J = \frac{2e}{h}(1+\varepsilon_J). \tag{1.6}$$

(ii) A QHR standard quantized on the ith plateau has resistance

$$R_{QHR} = R_K/i \tag{1.7}$$

with

$$R_K = \frac{h}{e^2}(1+\varepsilon_K). \tag{1.8}$$

(iii) A quantum current standard driven by frequency f_{SET} generates the current

$$I_{\mathrm{SET}} = Q_{\mathrm{S}} f_{\mathrm{SET}} \tag{1.9}$$

with

$$Q_{\mathrm{S}} = -e(1 + \varepsilon_{\mathrm{S}}). \tag{1.10}$$

Using Ohm's law $V = RI$, the equations (1.5), (1.7) and (1.9) can be combined in a relation that can be checked experimentally

$$K_{\mathrm{J}} R_{\mathrm{K}} Q_{\mathrm{S}} = ik \frac{f_{\mathrm{J}}}{f_{\mathrm{SET}}}. \tag{1.11}$$

Equation (1.11) reports the result of a general experiment of QMT: if the product of the empirical constants is equal to the product of two integer numbers and the ratio of two frequencies, the consistency of the quantum effects is proved. Since (1.11) is dimensionless, the results of any QMT experiments are not affected by the system of units adopted. Furthermore, thanks to the extremely low uncertainty achieved in measuring frequency, the right-hand side of the equation can be known with exceptional accuracy.

Combining (1.6), (1.8) and (1.10) with (1.11) and approximating at first order in the deviations, it follows

$$\frac{K_{\mathrm{J}} R_{\mathrm{K}} Q_{\mathrm{S}}}{2} \approx -(1 + \varepsilon_{\mathrm{J}} + \varepsilon_{\mathrm{K}} + \varepsilon_{\mathrm{S}}). \tag{1.12}$$

Let us call $\Delta_{\mathrm{QMT}} = \varepsilon_{\mathrm{J}} + \varepsilon_{\mathrm{K}} + \varepsilon_{\mathrm{S}}$ the deviation of the QMT result from unity.

If the measured Δ_{QMT} is compatible with zero within its experimental uncertainty, it is commonly said that the QMT *closes*, i.e. the corrections on the quantum effects are not necessary at a confidence level equal to its relative uncertainty. Otherwise, the QMT *does not close* and at least one of the three quantum standards, which cannot be identified, has a significant correction term and this would suggest an incomplete modelling of the realizations of the underlying quantum phenomena. A detailed review of the status of the individual edges can be found in [59].

Closing the QMT with a total relative uncertainty of few parts in 10^7 is considered as a relevant improvement in the adjustment of the empirical costants [19], the ultimate target to produce a metrological impact being one part in 10^8 [59, 50, 61, 39].

The QMT experiment can be implemented in two ways: the *indirect* QMT, or "charge" variant, and the *direct* QMT also called "current" variant.

The idea of the indirect variant is to accumulate the charge quanta, transferred by a single-electron device, on the electrodes of a cryogenic capacitor having a value traceable to a QHR. The voltage produced can then be measured with a voltmeter traceable to the JVS. For the first time, this QMT variant was proposed and followed by the National Institute of Standards and Technology (NIST) with the name

of electron-counting capacitance standard (ECCS) [60, 64]. After many years of research and development on the ECCS experiment, NIST obtained the first result of a closed QMT with a relative accuracy of 9.2×10^{-7} [59, 62, 60]: the best outcome achieved until now. A similar ECCS experiment was also pursued at PTB which was able to close the QMT with an accuracy of 1.7×10^{-6} [58, 66]. In both the ECCS experiments implemented at NIST and at PTB, dedicated measurements were carried out to detect single-electron transfer errors by performing a preliminary "shuttle pumping" experiment [63, 58]. This operation allows to estimate the contribution of the pump error to the ECCS uncertainty assessment.

Over the years, other NMIs were involved in similar experiments as, for instance, the Van Swinden Laboratorium (VSL) and the National Physical Laboratory (NPL) [19].

The direct variant of the QMT is based on the current produced by a single-electron device, a resistor traceable to QHR and a voltage measurement traceable to the JVS. Owing to the low current generated, a current amplification is necessary. The Laboratoire National de Métrologie et d'Essais (LNE) worked on a direct QMT achieving a value of $Q_S/e - 1 = (-5 \pm 13) \times 10^{-6}$ [69].

A detailed review of the status of the QMT experiments can be found in [19].

Chapter 2

DC low current measurements

As discussed in chapter 1, single-electron experiments are a possible realization of the new definition of the ampere: typically, the currents generated in these experiments are below the nA level. This chapter presents methods for the measurement of low DC currents.

The transresistance amplifier, one of the main elements of this dissertation, is introduced in section 2.1; section 2.2 deals with the voltage-resistance method; and the cryogenic current comparator is described in section 2.3.

2.1 Transresistance amplifier

A *transresistance amplifier* is a current-to-voltage converter (I-V converter), that measures an input current I_{IN} generating an output voltage $V_{\mathrm{OUT}} = RI_{\mathrm{IN}}$, where R is the transresistance gain of the amplifier.

A possible implementation of a transresistance amplifier is shown in figure 2.1: it consists of an operational amplifier (op amp), that is, a differential voltage amplifier with very high gain, inserted in a negative feedback loop containing the resistor R, which is the amplifier transresistance.

In the ideal case, through the feedback, the op amp steers the output voltage to keep the input voltages V_{p} and V_{n} equal, $V_{\mathrm{p}} = V_{\mathrm{n}} = 0$. Then, since $V_{\mathrm{n}} = 0$, I_{IN} flows all across R, and thus

$$V_{\mathrm{OUT}} = RI_{\mathrm{IN}}. \tag{2.1}$$

In the schematic of figure 2.1, R can be replaced with a generic impedance Z, thus obtaining the so-called *transimpedance amplifier*: in this case (2.1) becomes $V_{\mathrm{OUT}} = ZI_{\mathrm{IN}}$.

While in an ideal op amp the input current is null, in the real case two small non-zero currents I_{B^-} and I_{B^+} flow, see figure 2.2. These non-idealities can be modelled by introducing the input bias current I_{B} and the input offset current, I_{OS}, so that

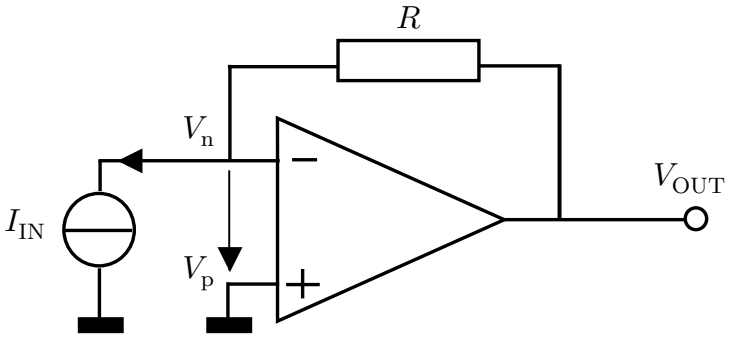

Figure 2.1: Schematic of a transresistance amplifier: − and + respectively label the inverting and noninverting inputs of the op amp, while V_{n} and V_{p} represent the input voltages.

$$I_{\mathrm{B^+}} = I_{\mathrm{B}} - I_{\mathrm{OS}}, \tag{2.2}$$

$$I_{\mathrm{B^-}} = I_{\mathrm{B}} + I_{\mathrm{OS}}. \tag{2.3}$$

Moreover, in a real op amp, owing to imperfectly balanced inputs, the output voltage is nonzero when the input voltage is zero. This can be modelled by adding an input offset voltage V_{OS} as shown in figure 2.2.

Taking into account these additional terms, a real transresistance amplifier can be represented as in figure 2.3. Now $V_{\mathrm{n}} = V_{\mathrm{OS}}$ and the current I_{R} crossing the resistor R is

$$I_{\mathrm{R}} = I_{\mathrm{IN}} + I_{\mathrm{B}} + I_{\mathrm{OS}}, \tag{2.4}$$

from which

$$V_{\mathrm{OUT}} = V_{\mathrm{OS}} + RI_{\mathrm{R}}. \tag{2.5}$$

This, combined with (2.4), gives

$$V_{\mathrm{OUT}} = +RI_{IN} + V_{\mathrm{OS}} + R(I_{\mathrm{B}} + I_{\mathrm{OS}}) \tag{2.6}$$

$$= +R\left[I_{\mathrm{IN}} + \frac{V_{\mathrm{OS}}}{R} + I_{\mathrm{B}} + I_{\mathrm{OS}}\right]. \tag{2.7}$$

Equation (2.7) demonstrates how the presence of I_{B}, I_{OS} and V_{OS} affects the measurement of I_{IN} by generating an error $\Delta I_{\mathrm{IN}} = V_{\mathrm{OS}}/R + I_{\mathrm{B}} + I_{\mathrm{OS}}$.

When R has a high value, (2.7) can be approximated as $V_{\mathrm{OUT}} \approx R[I_{\mathrm{IN}} + I_{\mathrm{B}} + I_{\mathrm{OS}}]$, showing that, in this case, the error from the offset and bias currents dominate over that from the offset voltage.

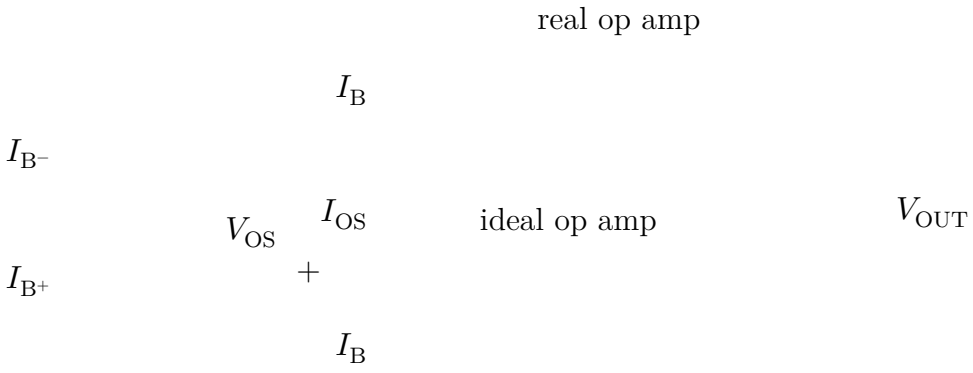

Figure 2.2: Schematic of a real op amp. The non-idealities are represented by the three current generators producing I_B and I_{OS} and by the voltage generator producing V_{OS}.

A method to eliminate the above errors is to perform a differential measurement of the output voltage by reversing the direction of I_{IN}. Therefore, being $I_{IN}^{+} = I_{IN}$ and $I_{IN}^{-} = -I_{IN}$, the amplifier produces accordingly two different output voltages

$$V_{OUT}^{+} = R\left[I_{IN} + \frac{V_{OS}}{R} + I_B + I_{OS}\right] \tag{2.8}$$

and

$$V_{OUT}^{-} = R\left[-I_{IN} + \frac{V_{OS}}{R} + I_B + I_{OS}\right]. \tag{2.9}$$

By taking the difference between V_{OUT}^{+} and V_{OUT}^{-}, it follows that

$$\Delta V_{OUT} = V_{OUT}^{+} - V_{OUT}^{-} = 2RI_{IN}. \tag{2.10}$$

As shown by (2.10), the differential measurement cancels the error due to the offsets.

However, the complete cancellation of the error happens only if the terms V_{OS}, I_{OS}, and I_B are constant over the two measurements. The possible drift of these components prevents the complete cancellation.

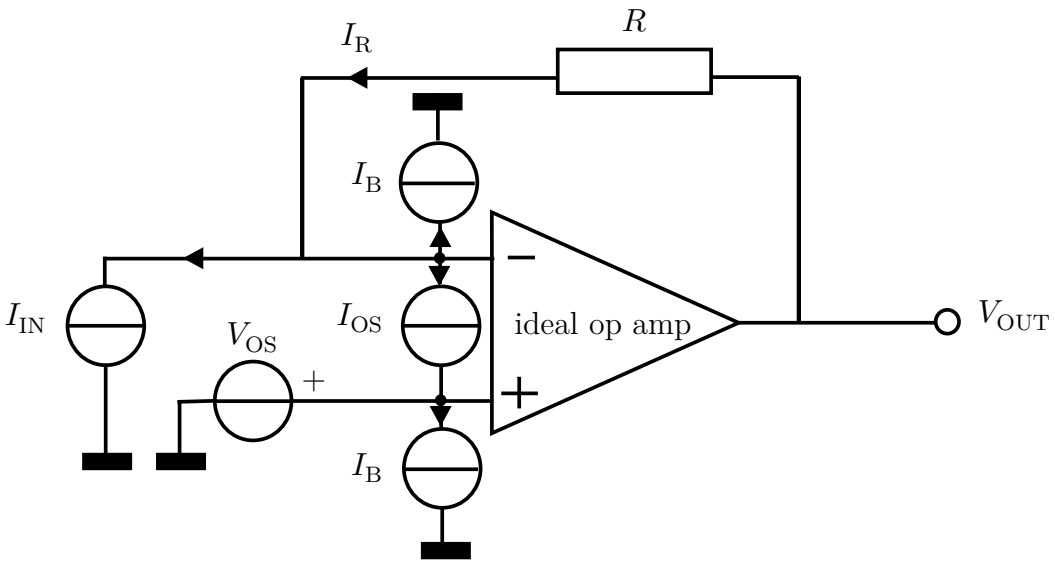

Figure 2.3: Schematic of a real transresistance amplifier which takes into accounts the non-idealities I_B, I_{OS} and V_{OS}.

2.2 Voltage-resistance method

Among the methods that can be employed to measure DC low currents there is the so-called *voltage-resistance method*, often used to measure the current produced by single-electron devices with high accuracy [128, 49, 48, 36, 11, 12, 47, 13]. The schematic representation of the method is reported in figure 2.4, which shows that this is actually a bridge measurement method. The purpose of this method is to

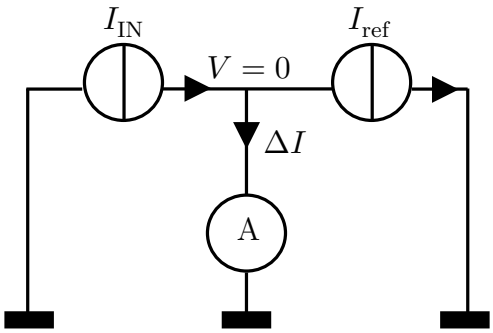

Figure 2.4: Principle schematic of the voltage-resistance method: I_{IN} is the measurand current, I_{ref} is the reference current produced to compensate I_p and ΔI is the difference between the two currents.

compare the measurand current I_{IN} against a reference current I_{ref} with about the

same magnitude of I_{IN}, $|I_{\mathrm{ref}}| \approx |I_{\mathrm{IN}}|$. The discrepancy ΔI between I_{IN} and I_{ref} is measured by the ammeter A. Therefore,

$$I_{\mathrm{IN}} = I_{\mathrm{ref}} + \Delta I \tag{2.11}$$

and since $|I_{\mathrm{ref}}| \approx |I_{\mathrm{IN}}|$, $|\Delta I| \ll |I_{\mathrm{p}}|$.

The current I_{ref} can be generated by a voltage source V_{ref} driving a resistor R, as shown in figure 2.5. The voltage V_{ref} is measured by the voltmeter V_1 and R is

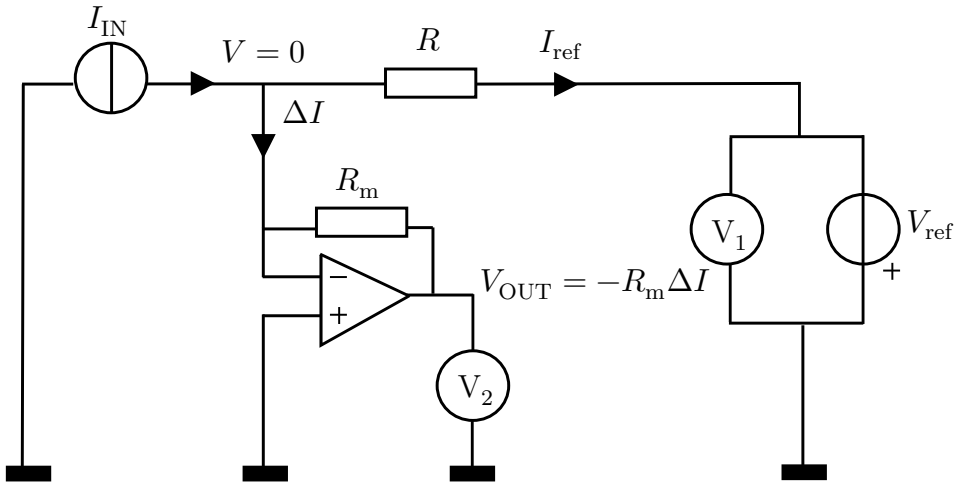

Figure 2.5: Schematic of the voltage-resistance method: the resistor R and a voltage generator supplying V_{ref} produce the current I_{ref}, while the transresistance amplifier measures ΔI.

a temperature-controlled resistor that allows obtaining a stable value of I_{ref}.

A transresistance amplifier with a transresistance gain R_{m} can then be used to measure ΔI, in place of the ammeter A of figure 2.4. The output signal of the amplifier V_{OUT} is measured by the voltmeter V_2.

By calibrating the two voltmeters V_1 and V_2 against a Josephson voltage standard and the resistances R and R_{m} against a quantum Hall resistance standard, the voltage-resistance method allows the direct traceability of the current I_{IN} to the quantum standards of voltage and resistance.

The main advantage of this method is that the relative uncertainty in the measurement of I_{IN}, is lower than the one achievable by directly measuring it with the transresistance amplifier. In fact,

$$\frac{u(I_{\mathrm{IN}})}{I_{\mathrm{IN}}} = \sqrt{\left[\frac{u(I_{\mathrm{ref}})}{I_{\mathrm{IN}}}\right]^2 + \left[\frac{u(\Delta I)}{I_{\mathrm{IN}}}\right]^2} \tag{2.12}$$

$$= \sqrt{\left[\frac{u(I_{\mathrm{ref}})}{I_{\mathrm{IN}}}\right]^2 + \left[\frac{\Delta I}{I_{\mathrm{IN}}}\right]^2 \left[\frac{u(\Delta I)}{\Delta I}\right]^2}, \tag{2.13}$$

where $u(\Delta I)/\Delta I$ mainly depends on the uncertainty of the transresistance amplifier gain and $|\Delta I/I_{\mathrm{IN}}| \ll 1$.

For example, typically $|\Delta I/I_{\mathrm{IN}}| \approx 10^{-4}$ and $u(\Delta I)/\Delta I \approx 10^{-4} \div 10^{-3}$, thus the contribution of the transresistance amplifier to the overall uncertainty of I_{IN} is of $10^{-8} \div 10^{-7}$. In this way, the drift of the transresistance gain between calibrations is typically negligible.

Therefore, the dominant contribution is given by $u(I_{\mathrm{ref}})$ and, since $I_{\mathrm{ref}} = V_{\mathrm{ref}}/R$, the main uncertainty contributions are those associated with the voltmeter measuring V_{ref} and R.

A major source of uncertainty is the stability of the high-value resistor R [100]: for this reason, frequent calibrations of R during the running experiment are often performed.

2.3 Cryogenic current comparator (CCC)

The *cryogenic current comparator* (CCC) is a device used to compare the ratio of two electrical currents with the highest precision [83, 82].

There are two types of CCCs available: type I and II [110]. The type I CCC is based on a toroidal-shaped superconductor (figure 2.6) in which two windings with N_1 and N_2 turns are wound around the toroidal direction. Through these windings two currents flow in opposite directions: I_1 and I_2 which are generated by two isolated current sources in the so-called *primary* and *secondary* circuit.

According to the Meissner effect, the currents I_1 and I_2 generate a supercurrent I that flows on the inner and outer surface of the torus, keeping the overall amount of magnetic flux inside the superconductor equal to zero. Due to the Ampère's law, the value of the supercurrent is

$$I = N_1 I_1 - N_2 I_2. \tag{2.14}$$

The key feature of the CCC is a DC superconducting quantum interference device (SQUID), which monitors the magnetic flux generated by I thanks to a pick-up coil inserted in the inner part of the torus. The SQUID then acts as a null detector by controlling one of the two current sources. When the flux is balanced,

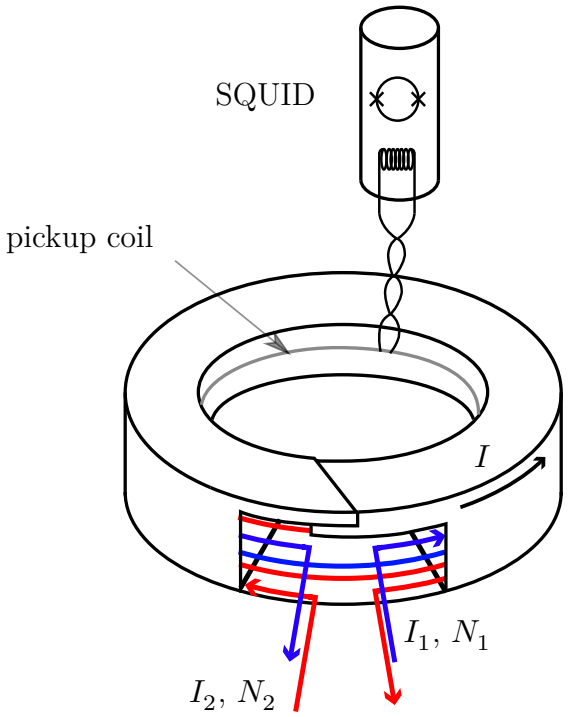

Figure 2.6: Schematic of a type I CCC. The secondary and primary circuits are depicted in red and blue respectively. The primary has N_1 turns and a current I_1 flowing trough it, while the secondary has N_2 turns and it is crossed by the current I_2. On the surface of the torus the supercurrent I flows. The ends of the superconducting torus are overlapping to avoid flux leakages. A coil picks up the flux generated by I, which is sensed by a SQUID detector through a coupling transformer.

the current ratio is exactly the reciprocal ratio between the corresponding number of turns,

$$\frac{I_1}{I_2} = \frac{N_2}{N_1}. \tag{2.15}$$

The superconducting torus should have the screen ends overlapping in order to minimize the magnetic flux leakage and reduce the ratio error [111].

In the type II CCC the two windings are instead wound along the poloidal direction and the pick-up coil is wound in the inner part of the torus [107].

While the type I CCC can be employed to measure small currents by amplifying them with a high and accurate gain [68], the type II can be used for high accuracy measurements of high currents, up to 100 A [108]. In fact, with the type II configuration, the windings can be placed away from the superconducting torus, thus avoiding that a high local magnetic flux density around the windings could destroy the superconducting state.

The CCC I worked on in PTB belongs to the type I thus, in the following chapters, I will always refer to this specific configuration.

In the last two decades, several type I CCCs with a large winding ratio (up to 1:30000) have been constructed to amplify the current produced in electron-counting experiments involving both metal-oxide and semiconductor-based pumps [69, 57, 109, 117, 56, 67], but the sensitivity is typically limited to parts in 10^6 at 100 pA. This result, which is well above the target of 10^7 at 100 pA required to realize the new quantum current standard, is mainly affected by the noise induced by the electromechanical coupling with the environment, low-frequency LC resonances, and noise rectifications due to SQUID nonlinearities [111].

Due to the above limitations the CCC is no longer employed for the measurement of low currents in single-electron experiments.

Despite that, the CCC has a central role in metrology: it is an important tool for the calibration of resistors, providing the direct traceability to the quantized Hall resistance. The ultimate accuracy in resistance ratio measurements achieved with the CCC is of a few parts in 10^9 [82].

Chapter 3

Noise characterization of transresistance amplifiers

The purpose of this chapter is to present the Allan deviation as a tool to analyze and characterize the noise and the offset stability of transresistance amplifiers. In particular, the attention is focused on the commercial transresistance amplifier FEMTO DDPCA-300 and on the advanced Ultrastable Low-noise Current Amplifier (ULCA), developed at PTB, both described in section 3.2.1 and 3.2.2.

Section 3.3.1 presents a simple and inexpensive temperature control system (thermostat) designed to improve the thermal stability of the FEMTO amplifier. The enhanced offset stability of the amplifier, obtained by employing the thermostat, is compared to the one of the bare amplifier in terms of Allan deviation.

For what concerns the ULCA, section 3.3.2 reports the Allan deviations of the amplifier noise evaluated by shielding it in different configurations. Among them, the one contributing to the minimum noise level was chosen to be employed during the single-electron experiment described in chapter 6.

3.1 Characterization of amplifier stability

The Allan variance

A powerful statistical tool to characterize the noise and the offset stability of an amplifier is the *Allan variance* (or *two-sample variance*) [1]. This tool overcomes the limitations of the standard variance for correlated noise processes (e.g. flicker noise and random walk) [2]. In fact, the Allan variance is well defined and has estimators with good statistical properties also for those noises for which the standard variance

does not converge[1].

The Allan variance is a measure of the stability of the quantity average between two adjacent time intervals. Let $y(t)$ be a variable quantity modelled as a random process (figure 3.1); the Allan variance without dead time is defined as

$$\sigma_y^2(\tau) = \frac{1}{2}\langle(\bar{y}_{j+1}^{\tau} - \bar{y}_j^{\tau})^2\rangle, \tag{3.1}$$

where

$$\bar{y}_j^{\tau} = \frac{1}{\tau}\int_{t_j}^{t_j+\tau} y(t)\ dt \tag{3.2}$$

is the average over the time τ starting at times $t_j = t_0 + j\tau$, j integer, and $\langle\rangle$ denotes the ensemble average.

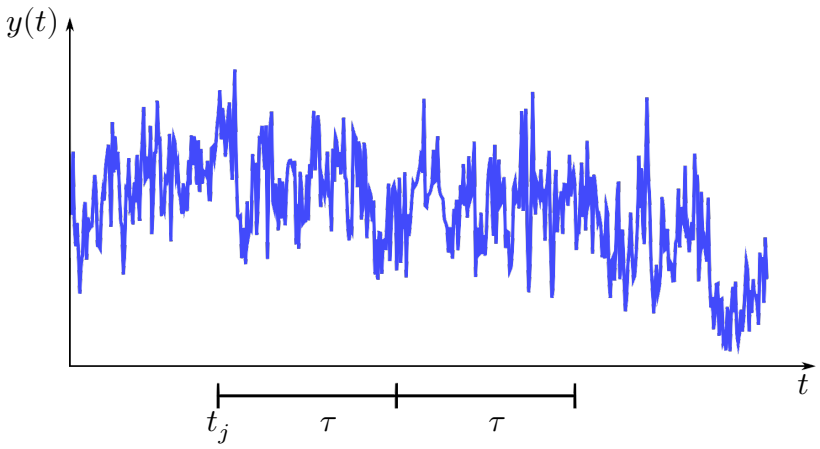

Figure 3.1: Representation of the variable quantity $y(t)$ as a random process.

The *Allan deviation* is then

$$\sigma_y(\tau) = \sqrt{\sigma_y^2(\tau)}. \tag{3.3}$$

Since, from (3.3), the Allan deviation depends on the averaging time τ, it is common to represent $\sigma_y(\tau)$ on a graph.

[1]It is fundamental to distinguish between a *variance*, which is parameter associated to a random process, that is, a mathematical model representing a physical phenomenon, and an *estimator* of the variance, which is an algorithm operating on measured quantities. A variance may be infinite for certain processes whereas an estimator always yields a finite number. For noise processes like flicker noise and random walk the standard variance is infinite; in this case the most common estimator of the standard variance, the *sample variance*, is no longer an unbiased and consistent estimator of the standard variance (see [3, Ch. 8] and [4]).

Table 3.1: Correspondence between the exponent α and μ and the common power-law noises.

Noise type	α	μ
Random walk	-2	1
Flicker	-1	0
White	0	-1

In practice, for a finite data set of size m, the Allan variance can be efficiently estimated by means of the *maximal-overlap estimator* [5]

$$\hat{\sigma}_y^2(n\tau_0) = \frac{1}{2(m-2n+1)} \sum_{j=1}^{m-2n+1} [\bar{y}_{j+n}^{\tau} - \bar{y}_j^{\tau}]^2, \tag{3.4}$$

where

$$\bar{y}_j^{\tau} = \frac{1}{n} \sum_{i=j}^{j+n-1} \bar{y}_j^{\tau_0} \tag{3.5}$$

and τ_0 is the averaging time for one measurement.

If there is dead time between the measurements, the estimates obtained from (3.4) should be corrected for a bias dependent on the noise type [6]. Furthermore, in the case of white noise, the Allan deviation corresponds to the standard deviation of the mean, independently from the data spacing (i.e. with or without dead time between the measurements).

The Allan variance can be also calculated from the spectral density function $S_y(f)$ of the random process $y(t)$ [7],

$$\sigma_y^2(\tau) = 2 \int_0^{\infty} S_y(f) \frac{\sin^4(\pi f \tau)}{(\pi f \tau)^2} \mathrm{d}f. \tag{3.6}$$

For many physical processes, the spectral density function is approximately a combination of a few power-law processes, that is, for the cases of interest for this work,

$$S_y(f) \approx \sum_{\alpha=-2}^{0} h_\alpha f^\alpha, \tag{3.7}$$

where each exponent α is associated to a different process and h_α are coefficients related to the process intensities. Table 3.1 reports the names of the common power-law processes with exponents $\alpha = -2, -1, 0$.

From (3.6), it can be shown that for power-law processes the Allan variance has the asymptotic behaviour[2] [7]

[2]In contrast, the relationship between the standard variance and the spectral density function

$$\sigma_y^2(\tau) \propto \tau^{\mu}, \tag{3.8}$$

with $\mu = -\alpha - 1$. This allows classifying the Allan variance on the basis of the exponent μ as reported in Table 3.1.

When the Allan variance is reproduced in a log-log plot as a function of τ, the power-law noise processes are represented as straight lines with slope μ. In the case of Allan deviation, the slope is $\mu/2$, as shown in figure 3.2. Therefore, from the evaluation of the asymptotic behaviour of the Allan deviation, it is possible to determine the underlying noise processes.

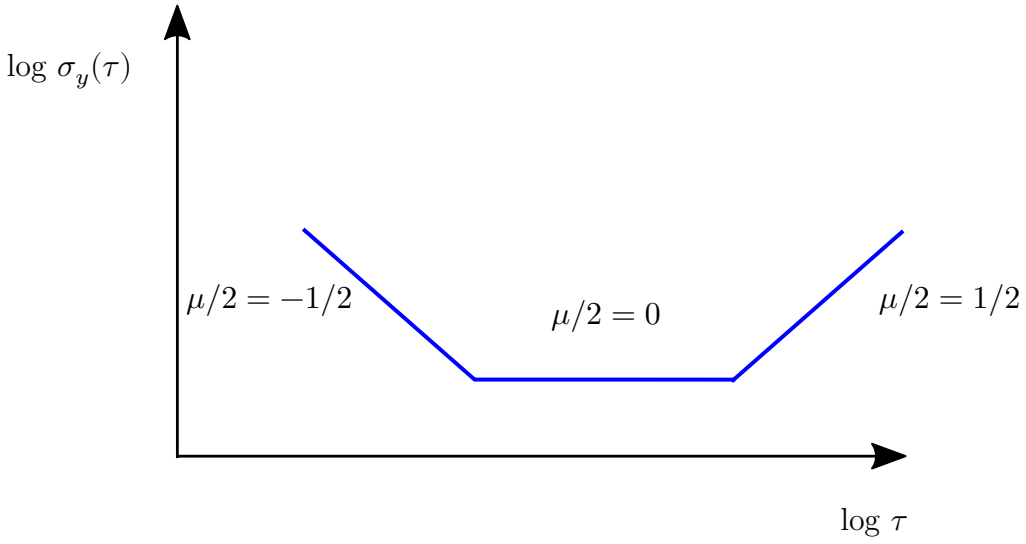

Figure 3.2: Example of Allan deviation $\sigma_y(\tau)$ represented in a log-log plot for the power-law noise processes of table 3.1.

---

of a random process is

$$\sigma_y^2 = \int_0^{\infty} S_y(f)\mathrm{d}f.$$

The above integral does not converge for power-law processes with $\alpha \leq -1$, like flicker and random walk. This shows that for this kind of processes the standard variance is no longer a good measure of the variability of the process and should be substituted with other variances (however, even for processes with $-1 < \alpha < 0$ and for which the standard variance converges, it can be shown that the sample variance is no longer an unbiased and consistent estimator of σ_y^2 [8]). Instead, (3.6) shows that, due to the kernel $\sin^4(\pi f\tau)/(\pi f\tau)^2 \sim f^2$ for $f \to 0$, the Allan variance converges for noises with $\alpha > -3$.

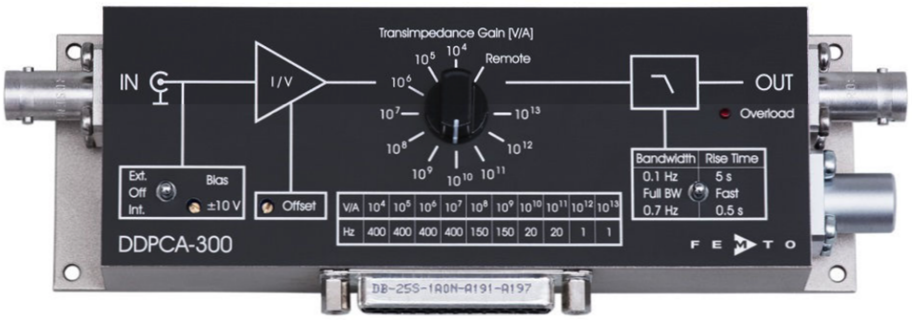

Figure 3.3: Picture of the FEMTO DDPCA-300 transresistance amplifier. Reproduced from [16], with permission of FEMTO Messtechnik GmbH.

3.2 Amplifiers investigated

3.2.1 FEMTO DDPCA-300

Thanks to the combination of good performances, the simplicity of use and affordable price, the FEMTO mod. DDPCA-300 transresistance amplifier is largely employed in electron-counting [9, 10, 11, 12, 13] and nanophysics experiments [15, 14].

The amplifier, represented in figure 3.3, has a nominal transresistance gain R_{nom} manually switchable from 10 kΩ to 10 TΩ in decadic steps. The specified accuracy of R_{nom} is 1 %. Depending on the range chosen, the gain temperature coefficient varies from 1×10^{-4}/K to 3×10^{-4}/K [16].

The maximum output voltage is ±10 V and the instrument is declared to be stable for input capacitances lass than 10 nF. The current noise depends on R_{nom} and reaches $0.2\,\mathrm{fA}/\sqrt{\mathrm{Hz}}$ for the highest values ($R_{\mathrm{nom}} = 1\,\mathrm{T\Omega}$ and $R_{\mathrm{nom}} = 10\,\mathrm{T\Omega}$).

The amplifier has a configurable output low-pass filter with a selectable bandwidth among 0.1 Hz, 0.7 Hz and the so-called *full bandwidth*. All measurements reported in the following section 3.3.1 and section 4.1.1 are performed in the full bandwidth mode, whose cutoff frequency is from 1 Hz to 20 Hz depending on the gain selection.

3.2.2 Ultrastable Low-noise Current Amplifier

The Ultrastable Low-noise Current Amplifier (ULCA) is an advanced instrument designed and developed at PTB to measure low currents of the order of 100 pA, with a relative uncertainty of about 10^{-7} [17].

The ULCA can be used for the validation of single-electron devices as a primary quantum standard in QMT experiments [18, 19]. The main features of this

instrument are expressed by its name: the very high stability of its gain and a very low-noise contribution to the measurements.

The ULCA layout is composed of two cascaded stages presented in figure 3.4: a current amplifier followed by a transresistance amplifier. The overall transresistance is then $A_{\mathrm{TR}} = G_I R_{IV}$, where G_I is the current gain of the first stage and R_{IV} is the transresistance of the second stage.

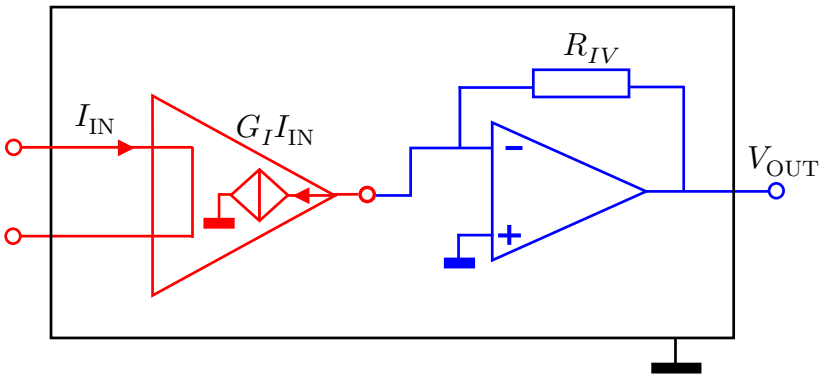

Figure 3.4: Simplified schematic of the ULCA: the red block is a current amplifier with gain G_I; the blue one, a transresistance amplifier with gain R_{IV}.

The ULCA can be operated either in a current measurement mode or in a current source mode to generate small currents.

Since the aim of this work is to measure the current produced by single-electron pumps, the interest is focussed on the current measurement instead of the current source mode: for further details about the latter see [18].

One of the advantages of the ULCA is that it is a compact and portable device operating at room temperature with a copper-made case that ensures high thermal stability. The amplifier is powered by a battery box (BatBox) composed of two separate batteries to ensure long, uninterrupted measurements: when one is powering the ULCA, the other is charging. Thanks to the low power consumption (11 mA of total supply current drawn from the battery), the temperature inside the instrument remains close to the ambient temperature. However, the internal temperature can be recorded from an on-board temperature sensor.

Different versions of ULCA have been developed over the years to fulfil a variety of experimental needs. During my experience at PTB, I worked with three different versions of the ULCA: the *standard* ULCA whose calibration is reported in section 4.2, the *low-bias* ULCA employed in the cable noise measurements described in section 3.3.2 and section 6.3.2 and the *low noise* ULCA used in the single-electron experiment reported in chapter 6. These versions are briefly described below.

- **Standard ULCA** (first generation): the standard ULCA, also called the 3 GΩ ULCA has an overall transresistance $A_{\mathrm{TR}} = 1\,\mathrm{G\Omega}$, with $G_I = 10^3$

Figure 3.5: A two-channel standard ULCA. Reproduced from [18], with the permission of AIP Publishing.

and $R_{IV} = 1\,\mathrm{M\Omega}$. The name comes from the $3\,\mathrm{G\Omega}/3\,\mathrm{M\Omega}$ resistor network at the input stage composed of 3000 $2\,\mathrm{M\Omega}$ NiCr thin-film resistors. For the standard ULCA, the white noise level is $2.4\,\mathrm{fA}/\sqrt{\mathrm{Hz}}$ with a dynamic range of $\pm 5\,\mathrm{nA}$. The relative uncertainty contribution from fluctuations and drift of the transresistance within one week after the calibration with the CCC is 10^{-7}, while the long-term drift is $5 \times 10^{-6}/\mathrm{yr}$ [18]. With a one day average, a relative uncertainty of 10^{-7} over 100 pA can be reached [18]. The input bias current is around $\pm 30\,\mathrm{fA}$ with a temperature dependence of $\pm 1\,\mathrm{fA/K}$. This ULCA is particolarly suited for measurements with repetition frequencies down to around 1 mHz, when then the $1/f$ noise corner starts being evident. This allows, for example, to push down to 1 mHz the on-off switching of the current measurements, in order to suppress the noise and the drift effect. A picture of the standard ULCA is reported in figure 3.5.

- **Low-bias ULCA** (2nd generation): among the second generation variants of the ULCA [20], PTB recently developed this version called $175\,\mathrm{G\Omega}$ low-bias ULCA: with a bias current below $\pm 100\,\mathrm{aA}$ this version is particularly suitable to measure sub-picoampere currents. Its transresistance value is $A_{\mathrm{TR}} = 1\,\mathrm{T\Omega}$, with $G_I = 10^5$ and $R_{IV} = 10\,\mathrm{M\Omega}$. In this version the input resistance network is made by $1\,\mathrm{G\Omega}$ thick-film resistors combined in series and in parallel. The input bias current is very stable in time and with a temperature dependence of $\pm 10\,\mathrm{aA/K}$, thus experiments without thermal stabilization are possible. The estimated noise level is $0.4\,\mathrm{fA}/\sqrt{\mathrm{Hz}}$ with $1/f$ corner at around $30\,\mu\mathrm{Hz}$. Thanks to the improved stability of this ULCA version, measurements with an accuracy of 10 aA can be obtained with a short averaging time (around 30 min) both with the ON-OFF switching of the current or not [21].

- **Low noise ULCA** (2nd generation): this version is also called the 10 GΩ low noise ULCA. It has an overall transresistance gain of $A_{\mathrm{TR}} = 1\,\mathrm{G\Omega}$, with $G_I = 10^3$ and $R_{IV} = 1\,\mathrm{M\Omega}$. The resistance network can be implemented using series and parallel of 10 MΩ thin-film resistors made by NiCr or CrSi ($10\,\mathrm{M\Omega} \times 1000 = 10\,\mathrm{G\Omega}$). The estimated noise is $1.4\,\mathrm{fA}/\sqrt{\mathrm{Hz}}$, lower than the 3 GΩ ULCA. Thanks to the reduced noise level, the measurement time is reduced by a factor of two compared to the standard ULCA [22]. The low noise ULCA presents has $1/f$ corner at 600 µHz. The bias input current is greater than that of the 175 GΩ low-bias ULCA, being ±3 fA with a temperature coefficient of ±0.2 fA/K [20]. A comparison between the low noise ULCA and the standard ULCA in terms of noise and gain stability over the years is reported in [22].

3.3 Results

3.3.1 FEMTO DDPCA-300

In this section it is described a temperature control system (thermostat) employed to improve the thermal stability of a FEMTO DDPCA-300 transresistance amplifier.

Description of the thermostat

In figure 3.6 is presented the assembly diagram of the thermostat, whose operating principle is based on an actuator: the thermoelectric cooler TEC. The TEC element is placed between the liquid heat exchanger, HE, and the copper plate, CP, on which the amplifier A is mounted. The purpose of CP is to obtain an homogeneous temperature across the surface of A and to minimize temperature gradients. For what concerns thermal resistances, A, CP and HE, have the surfaces covered with a layer of thermal grease to minimize them. These elements are fixed together and placed in a box filled with expanded polystyrene, TI, to provide a thermally insulated environment.

A small circulation pump, P, together with a passive heat radiator, HR and HE forms a hydraulic circuit where a solution of ethylene glycol flows as exchange fluid.[3] A temperature controller, TC, measures the temperature of CP through the thermistor NTC and drives TEC to keep the temperature T^{set} . To measure the effective temperature reached by the amplifier, T^{A}, a platinum resistance thermometers Pt100 is glued on its case. Another Pt100 is used to measure the environmental

[3]The components of the hydraulic circuit belong to a kit for the refrigeration of computer microprocessors.

temperature T^{E}. Both the Pt100 are acquired by a resistance meter M.

In table 3.2 are listed the components employed for the thermostat assembly, while a picture of the thermostat is shown in figure 3.7.

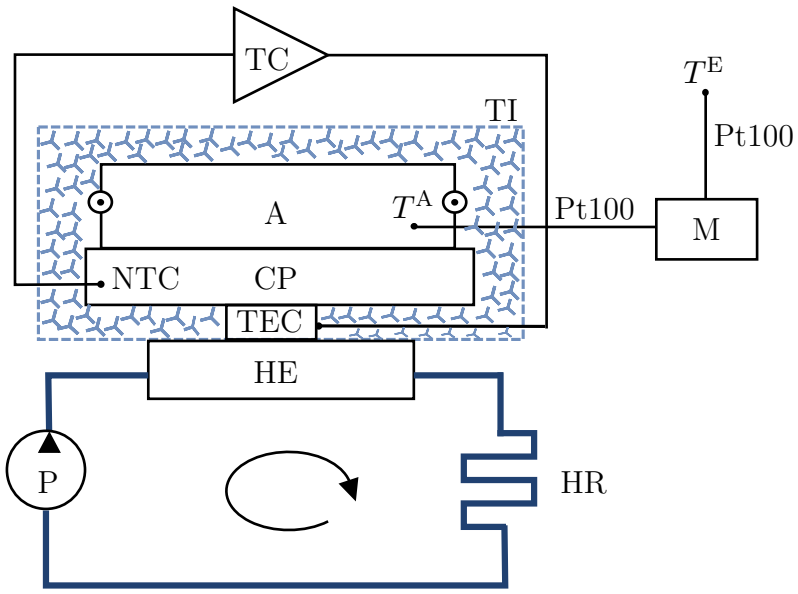

Figure 3.6: Schematic representation of the thermostat: the amplifier A is placed on the copper plate CP in which is embedded the thermistor NTC. The element NTC forms, together with the temperature controller, TC, and the thermoelectric element, TEC, a feedback circuit keeping A at the temperature T^{set}. All the feedback circuit elements, except TC, are placed inside the insulating box TI.

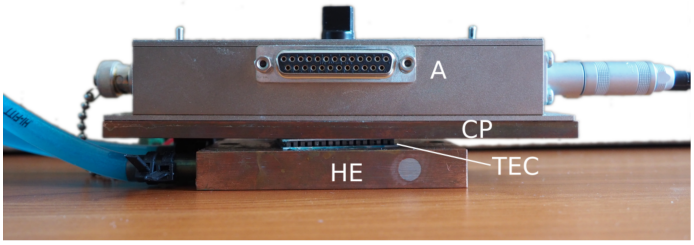

Figure 3.7: Side view of the thermostat active part taken out from the insulating box. It shows the amplifier, the copper plate CP, the thermoelectric element TEC and the heat exchanger HE. Reproduced with permission from [23] © IOP Publishing. All rights reserved.

Table 3.2: Components of the thermostat.

Name	Description
A	FEMTO mod. DDPCA-300
TEC	Laird Technologies mod. CP14-127-045L
HE	Thermo electric devices mod. Ll301
NTC	Mini betacurve thermistor probe mod. 10K3MBD1
P	Thermaltake pump: fow rate 44 l/h
HR	Thermaltake radiator mod. Rocket—CL-W0011: surface area 1300 cm^2, thermal resistance 0.5 °C/W, total coolant volume 0.8 l.
TC	Thorlabs mod. TED 350 bench-top temperature controller
Pt100	Termics 100 Ω platinum resistance thermometer
M	Agilent data mod. 34970A data acquisition/logger switch unit

Offset stability

The offset stability of the temperature-controlled amplifier was compared with the bare one. First of all, the bare A, set at its highest nominal gain $R_{\mathrm{nom}} = 10\,\mathrm{T\Omega}$ and left open-circuited[4], was placed in a non-thermostated laboratory. The values of T^{E}, T^{A} and the offset voltage V_{O} were recorded for several days with a sampling time of about 7.4 s. For such a high value of R_{nom}, the offset voltage is approximately given by

$$V_{\mathrm{O}} \approx R_{\mathrm{nom}} I_{\mathrm{b}}, \tag{3.9}$$

where I_{b} is the bias input current of A.

Figure 3.8 reports the acquired data for the bare case, showing how I_{b} is directly affected by the fluctuations of T^{E}. The variations of I_{b} are coherent with the specifications of A indicating that $I_{\mathrm{b}} < 10\,\mathrm{fA}$ and that it doubles every 10 °C of temperature increase [16]. This behaviour can be interpreted as the temperature dependence of I_{b} for JFET transistors, that is,

$$I_{\mathrm{b}} \approx I_{\mathrm{b}}(T_0) 2^{\dfrac{T - T_0}{10\,^{\circ}\mathrm{C}}}, \tag{3.10}$$

where T_0 is a reference temperature. From (3.10), the temperature coefficient of I_{b} can be obtained as

$$\alpha(I_{\mathrm{b}}) \approx \frac{1}{I_{\mathrm{b}}} \frac{\mathrm{d}I_{\mathrm{b}}(T)}{\mathrm{d}T} \approx \frac{\ln 2}{10\,^{\circ}\mathrm{C}} \approx 7\%/^{\circ}\mathrm{C}, \tag{3.11}$$

which roughly corresponds to the variations observed in figure 3.8.

[4] the input was closed with a dust cap

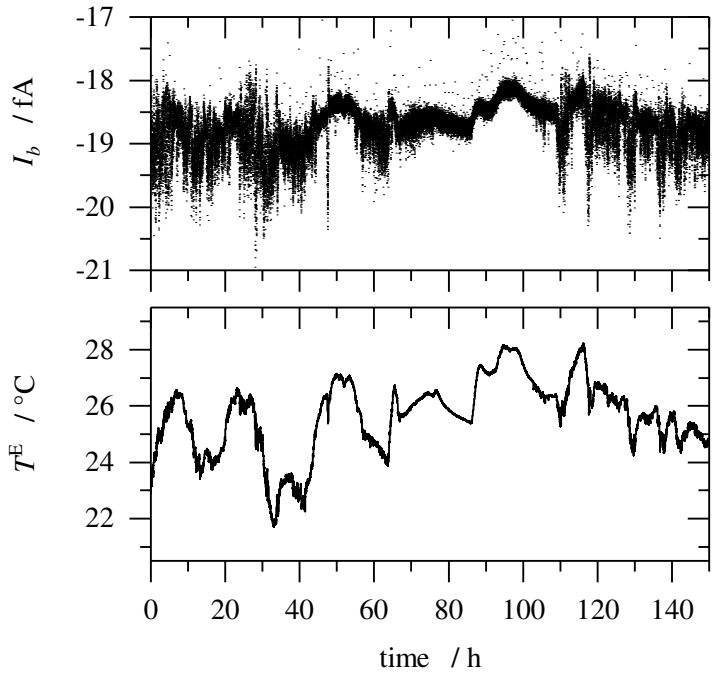

Figure 3.8: Time series representing the instability of the bare amplifier. The top curve represents the calculated input bias current I_b; the bottom curve represents the environment temperature T^E. Reproduced with permission from [23] © IOP Publishing. All rights reserved.

The measurements were repeated after mounting A on the operating thermostat with a $T^{set} = 25\,°C$[5], and the results are shown in figure 3.9. While T^E varied between 22 °C and 28 °C, the variation of T^A was limited to 0.05 °C over the entire acquisition period. In this case, I_b showed reduced fluctuations no longer correlated with the behaviour of T^E.

Finally, in figure 3.10, are represented the Allan deviations of I_b evaluated with and without the operating thermostat. With the working thermostat the white noise region was extended to 8200 s, achieving a resolution of 6 aA with an improvement of a factor of around 15 compared to the bare case.

It was also demonstrated how, by employing the proposed thermostat, the thermal contribution to gain instabilities of A can be suppressed to a level below 7×10^{-7} (more details in [23]).

[5]Since the system proposed here is intended to be used in a non-thermostated environment, this temperature allows to operate without the risk of moisture formation inside the amplifier.

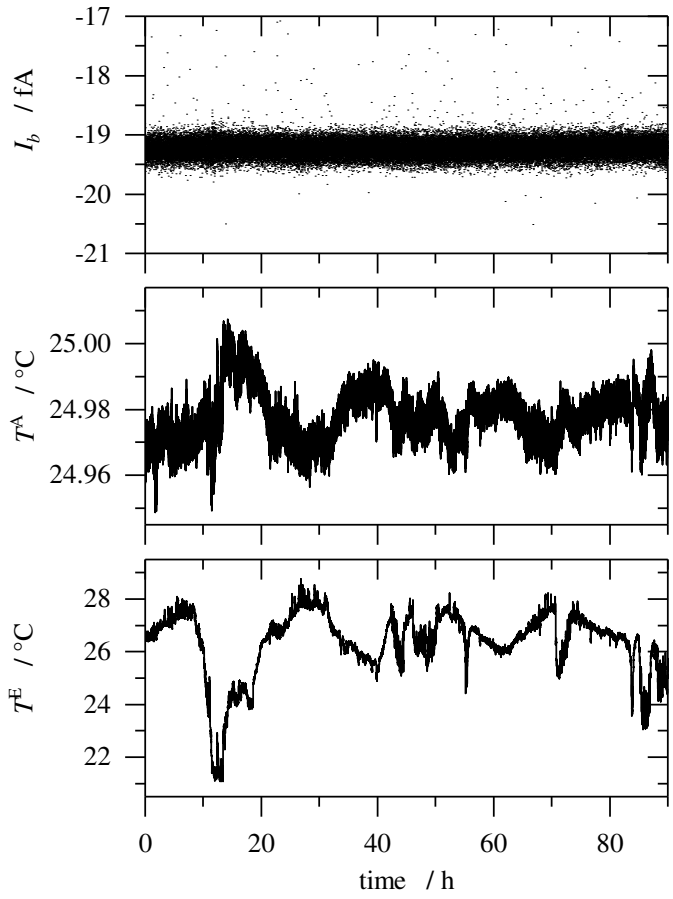

Figure 3.9: Time series measured from the amplifier A mounted on the thermostat with a setted temperature of $T^{\mathrm{set}} = 25\,^{\circ}\mathrm{C}$. From the bottom to the top: the environment temperature T^{E}, the amplifier temperature T^{A} and the input bias current I_{b}. Reproduced with permission from [23] © IOP Publishing. All rights reserved.

3.3.2 PTB Ultrastable Low-noise Current Amplifier

In order to measure the current produced by single-electron devices, the ULCA must be connected to a cryogenic probe through a coaxial cable. This section reports the results of shielding tests performed to minimize the noise and the interferences contributions coming from the external environment on the current measurements.

The tests were performed with a low-bias ULCA connected to a coaxial cable Bedea, whose specifications are reported in section B.5, table B.6. The other end of the cable was left open-circuited (closed with a dust cap). The current noise was measured by connecting the amplifier output to an Agilent 34410-A multimeter having a sampling interval of approximately 1 ms and with the autozero off.

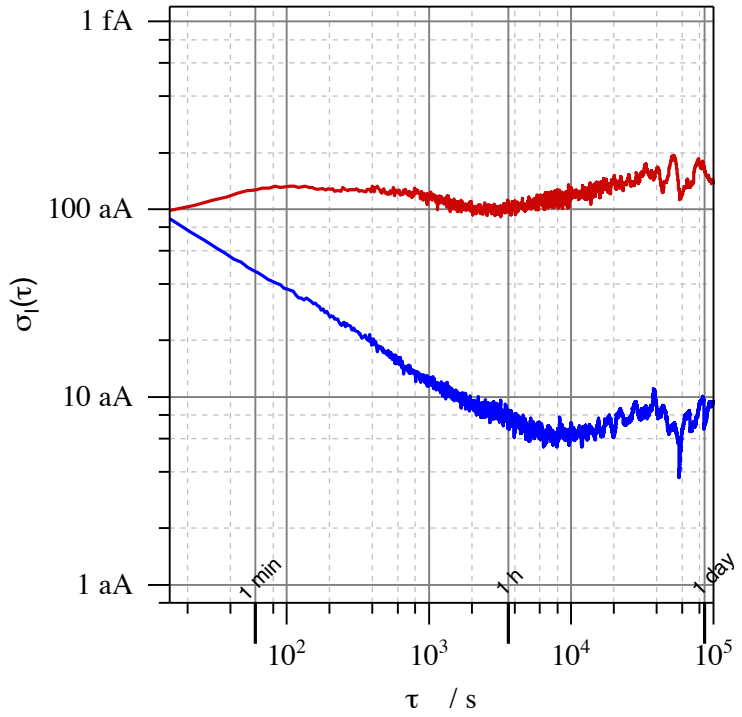

Figure 3.10: Allan deviation of I_b: (—) represents the case of the bare A, while (—) is estimated for A thermostated. Reproduced with permission from [23] © IOP Publishing. All rights reserved.

Three different shielding conditions were investigated:

- leaving the ULCA and the coaxial cable not shielded.
- placing the ULCA inside a Mu-metal[6] box, while the coaxial cable was left outside.
- placing both the ULCA and the coaxial cable inside the Mu-metal box.

Figure 3.11 reports the Allan deviations of the current noise estimated in the three different shielding conditions together with the one measured from the low-bias ULCA having the input closed with a dust cap.

The first consideration that can be done is that placing in the Mu-metal box both the ULCA and the coaxial cable helps to extend the white noise region to longer τ. Thus, this shielding condition allows to increase the measurement resolution of a factor of about 4 compared to the others investigated. For this reason

[6]Mu-metal is ferromagnetic alloy with a very high permeability usually employed in shielding electronic devices from static or low-frequency magnetic fields.

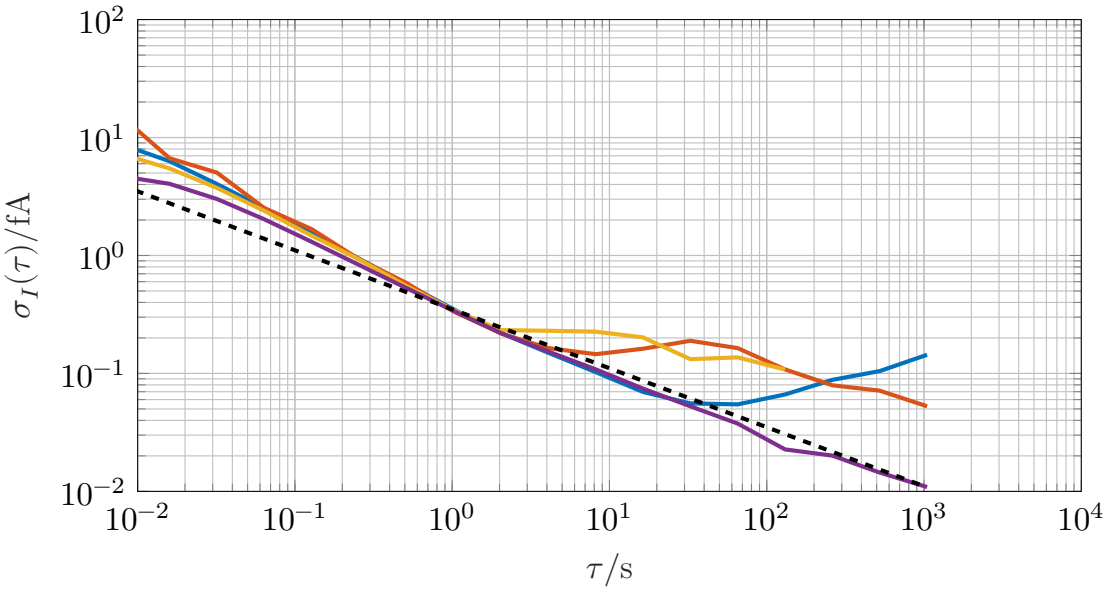

Figure 3.11: Plot of the Allan deviations of the current noise for the ULCA in three different experimental conditions: (—) represents the ULCA with only dust cap at the input, (—) was acquired with both the ULCA and the cable not shielded, (—) with only the ULCA shielded in Mu-metal and (—) with both the ULCA and the cable shielded in Mu-metal. Dashed line represents a reference for the white noise slope.

this configuration was adopted for the setting of the single-electron experiment illustrated in chapter 6.

On the other hand, in the case of both the ULCA and the coaxial cable unshielded and of only the cable unshielded, it can be noticed, after few seconds of measurement, the presence of a bump and a subsequent drift. The origin of this bump is not clear yet: the major hypothesis lead to a magnetic or thermal source present in the laboratory. However, after the air conditioning system has been improved in the laboratory, these features in the Allan deviation were no longer found as shown in the further measurements reported in figure 6.6.

3.3.3 Final remarks about the amplifiers employed in this work

From the comparison between the corresponding Allan deviations, it can be observed that the temperature-controlled FEMTO (figure 3.9), the low-bias and the low noise ULCA (figure 3.11 and figure 3.12) reach a noise level which is comparable. For instance, for acquisition time of 100 s, the noise level of the temperature-controlled FEMTO is around 40 aA, the one of the low-bias ULCA is around 30 aA

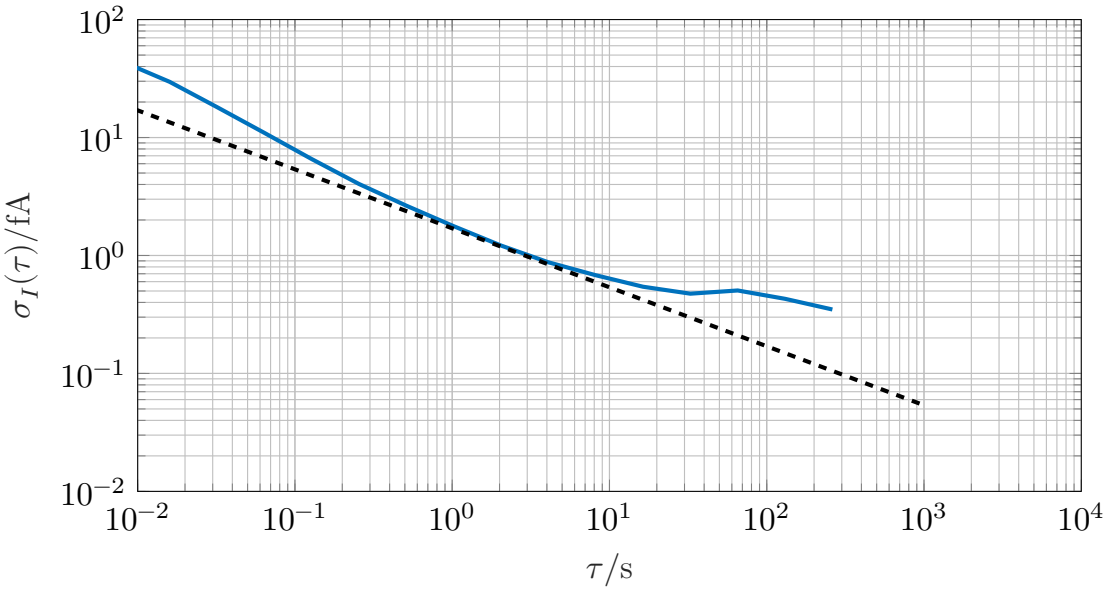

Figure 3.12: Plot of the Allan deviation of the current noise for the low noise ULCA. Dashed line represents a reference for the white noise slope.The output of the ULCA was measured with an Agilent 34410-A multimeter having a sampling interval of approximately 1 ms and with the autozero off.

and the low noise ULCA is around 40 aA.

However, due to its architecture, the ULCA can be calibrated with higher accuracy with respect to the FEMTO, see section 4.1.1 and section 4.2. Furthermore, the FEMTO emplyes resistors with high resistance values which, for long measurement time, have a lower stability than that of the resistor network of the ULCA. Thus, the ULCA should be preferred for high accuracy applications.

Nonetheless, due to the high stability of the current offset (figure 3.9), the temperature-controlled FEMTO can be successfully employed in low current measurements when it is used as a null detector as, for instance, in [11, 12, 13], (section 2.2).

For what concerns the noise measurements in the cables described in section 3.3.2 and section 6.3.2, the low-bias ULCA was employed. Due to its low noise contribution to the measurements, this version of the ULCA is particularly suitable to detect the noise induced by the external environment. In fact, the measured lines are long and thus have appreciable capacitances that can generate noise once subjected to the voltage noise of the amplifier.

For the single-electron experiment described in chapter 6, two low noise ULCAs were used: their transresistance gain value $A_{\mathrm{TR}} = 1\,\mathrm{G\Omega}$ is suitable to measure the nominal current produced by the pump $I^{\mathrm{nom}} = 100\,\mathrm{pA}$. The Allan deviation of the current noise of one of the two low noise ULCAs employed in the experiment can

be observed in figure 3.12.

Chapter 4

Calibration of transresistance amplifiers

This chapter describes the calibration of the gain of transresistance amplifiers with traceability to the unit of electrical resistance, the ohm (Ω), through its realization with the quantum Hall effect. Two different calibration methods are applied to the two transresistance amplifiers FEMTO DDPCA-300 (section 3.2.1) and ULCA (section 3.2.2).

The first method, described in section 4.1.1, was developed at INRiM and exploits the capacitance-charging method to generate currents in the range from 100 fA to 100 pA. This calibration method requires the traceability to the units of capacitance and time. The set-up proposed for this experiment is simple, easy to use and demands a low budget. It was employed for the calibration of the FEMTO DDPCA-300 [141].

The second calibration method, presented in section 4.2, was developed at PTB for the calibration of the ULCA and involves a 14 bit CCC. This is a standard method and further details are reported in [111, 18, 100].

4.1 Capacitance-charging method

The capacitance-charging method allows the accurate generation of DC currents by applying a linear voltage ramp on a capacitor. When a voltage $v_{\mathrm{in}}(t)$ is applied to a differentiating capacitor C, the test current

$$i(t) = C\frac{\mathrm{d}v_{\mathrm{in}}(t)}{\mathrm{d}t} \tag{4.1}$$

is generated.

The produced current $i(t)$ can be employed for the calibration of the gain of a transresistance amplifier. As shown in figure 4.1, the amplifier A, whose transresistance gain R has to be calibrated, produces an output voltage $v_{\mathrm{out}}(t) = Ri(t)$.

Therefore, the relation

$$R^{-1} = C\frac{1}{v_{\text{out}}(t)}\frac{\mathrm{d}v_{\text{in}}(t)}{\mathrm{d}t} \tag{4.2}$$

holds. The above equation shows how the measurement of R requires only the traceability to the units of capacitance and time, since only a voltage ratio is involved.

The capacitance-charging method is completely insensitive to the constant voltage burden across A, that could be caused by a non-zero input impedance or by offsets: it has no effect on the ramp slope and, consequently, on the current generated.

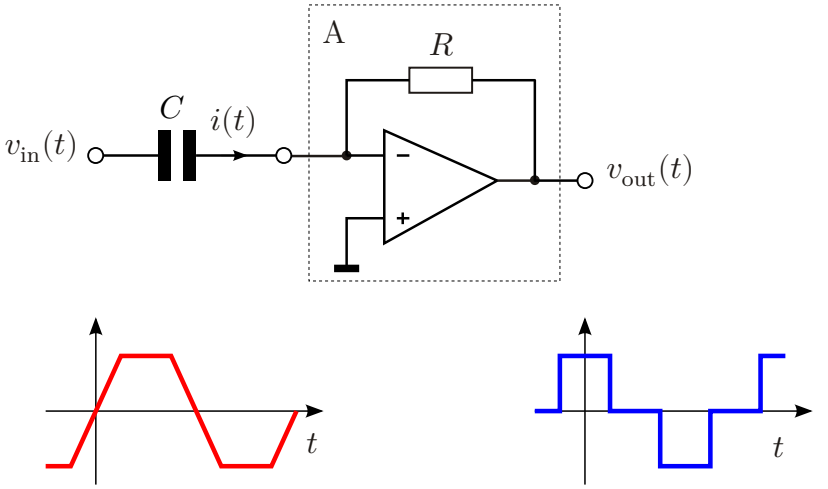

Figure 4.1: Principle schematic of the capacitance-charging method employed for the calibration of a transresistance amplifier A. The waveforms pictured as $v_{\text{in}}(t)$ (–) and $v_{\text{out}}(t)$ (–) are associated to the calibration mode proposed.

4.1.1 Calibration of the FEMTO amplifier using the capacitance-charging method

This section presents a set-up for the calibration of the transresistance gain of the FEMTO DDCPA-300, implementing the capacitance-charging method. This set-up is a derivation of a previous one employed for the calibration of low-current meters [131, 129].

4.1.2 Set-up and calibration procedure

As shown in figure 4.2, the source G generates the voltage $v_{\text{in}}(t)$, which is applied to the capacitor C. In agreement with (4.1), C produces the current $i(t)$ which is

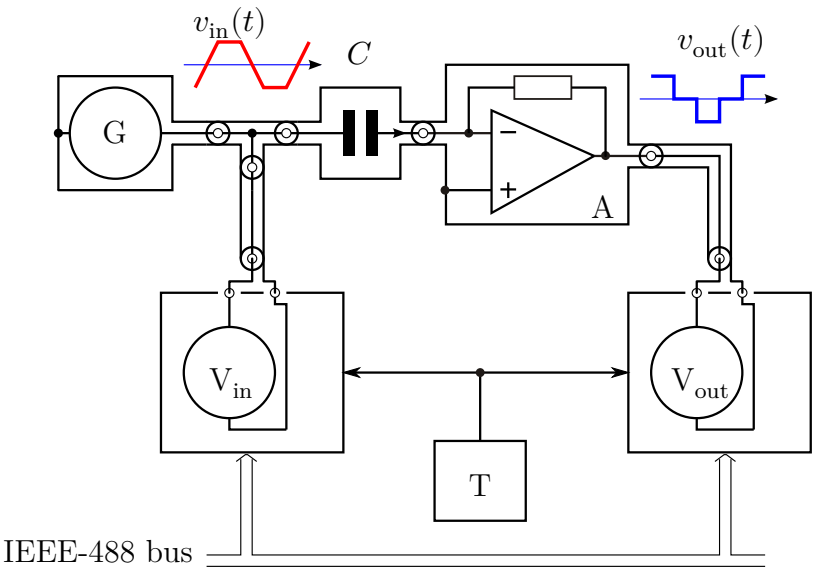

Figure 4.2: Schematic of the calibration set-up. Note that the whole circuit is wired using coaxial cables. Reprinted by permission from [141] © 2018 IEEE.

injected into the transresistance amplifier A to be calibrated. The waveform $v_{\text{in}}(t)$ has trapezoidal shape, as shown in figure 4.4. This piecewise linear waveform has three different voltage slopes, positive, negative and zero, to which correspond three different values of the nominal current: $+I_{\text{nom}}$, $-I_{\text{nom}}$ and 0. The value $I = 0$ allows to determine the offset of A while the measurement is running.[1].

Both the input voltage $v_{\text{in}}(t)$ and the output voltage $v_{\text{out}}(t)$ are sampled by two voltmeters V_{in} and V_{out} that share the same trigger signal from the generator T. The recorded voltage samples $v_{\text{in},h}$ and $v_{\text{out},h}$, acquired at times t_h, are transferred through an interface bus IEEE-488 and stored in the computer for off-line processing.

The transresistance gain of A is estimated from a finite-difference version of (4.2) implemented in a Matlab script, see (2) in [131] as

$$R_h^{-1} = C \frac{1}{v_{\text{out},h}} \frac{v_{\text{in},h+1} - v_{\text{in},h}}{\Delta t}, \tag{4.3}$$

with $\Delta t = t_{h+1} - t_h$.

[1] A sligthly different variation of the set-up can be employed by substituting the linear voltage ramp $v_{\text{in}}(t)$ with a sinusoidal waveform with a very low frequency: this allows to achieve a relative calibration uncertainty of the order of 10^{-4} [141].

Figure 4.3: Picture of the calibration set-up corresponding to the schematic of figure 4.2. Bottom left: source G with its power supply. Centre: C, A and trigger. Top left: V_{in}. Right: V_{out}. Note that the amplifier A and the capacitor C are directly connected to reduce possible effects of dielectric absorption in the insulating materials of the connection. Reprinted by permission from [141] © 2018 IEEE.

4.1.3 Instruments employed

Voltage source G This is a purpose-built voltage source. The generated voltage signal $v_{in}(t)$ has an amplitude of $\pm 10\,V$, and the ramp slopes are about $\pm 0.1\,V/s$. Each piece of the ramp has a duration of about 200 s: thus, the period of $v_{in}(t)$ is about 800 s. The source is based on analogue electronics; it is battery-operated, free-running and galvanically isolated to reduce the interferences to the calibration circuit. Details about the source can be found in [131].

Injection capacitor C This is a standard gas or vacuum capacitor to avoid the phenomenon of dielectric absorption typical of all solid-dielectric capacitors, which would give deviations from (4.1). In that case an equivalent model of the capacitor must be considered, as the one represented in [132], figure 4. The possible deviation of the capacitance value from the ideal case is taken into account in the final uncertainty budget, see table table 4.3. Different

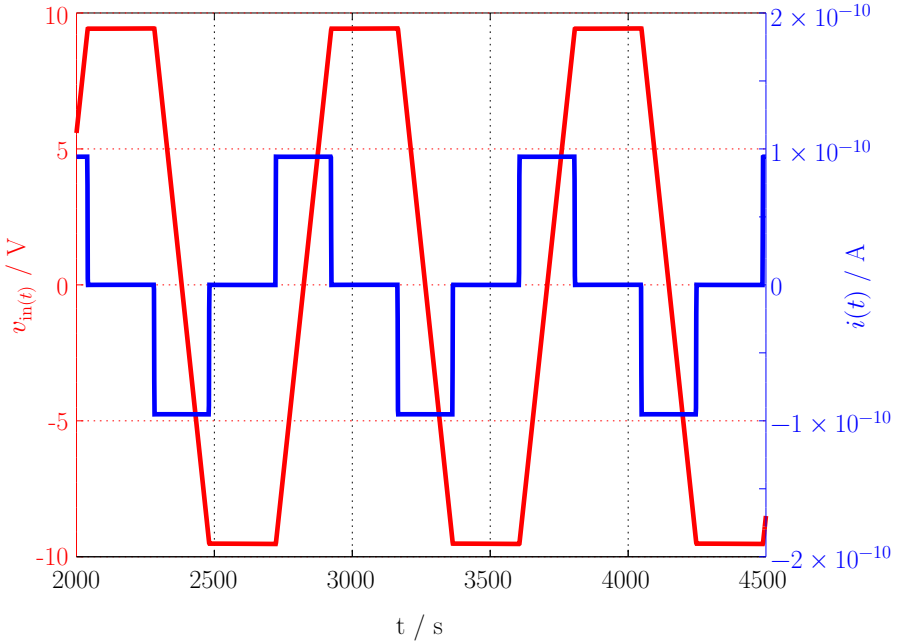

Figure 4.4: The outcome of a typical measurement ($R_{\mathrm{nom}} = 10\,\mathrm{G\Omega}$, $C_{\mathrm{nom}} = 1\,\mathrm{nF}$, $I_{\mathrm{nom}} = \pm 95\,\mathrm{pA}$). Red line (—) is the trapezoidal ramp signal $v_{\mathrm{in}}(t)$; blue line (—) is the test current $i(t)$. The sign of $i(t)$ is determined by the sign of the slope of $v_{\mathrm{in}}(t)$: when $v_{\mathrm{in}}(t)$ is constant $i(t) = 0$. Reprinted by permission from [141] © 2018 IEEE.

Table 4.1: Standard capacitor models with their nominal capacitance value C_{nom} employed in the experiments.

C_{nom}	Model
1 pF	General Radio mod. 1403-K
10 pF	Sullivan mod. C80001
100 pF	Sullivan mod. C80002
1 nF	General Radio mod. 1404-A [143]

nominal capacitance values from 1 pF to 1000 pF are employed to cover the investigated current range, from $\approx 100\,\mathrm{fA}$ to $\approx 100\,\mathrm{pA}$. Table 4.1 reports the models employed during the experiments. The standard capacitors were measured with a commercial capacitance bridge (Andeen–Hagerling mod. 2500A) working at a frequency of 1 kHz as a two terminal-pair standard [133, chapter 2]. The calibration is traceable to the Italian national standard of electrical

capacitance. Residual frequency dependences in gas-dielectric capacitors have been observed, and ascribed to surface effects [139, 138, 140].

It has been shown that, for one of the investigated capacitors (1404-A), the deviation of the capacitance between the very low frequency employed in the experiment and the measurement frequency can be extrapolated with measurements in the audio frequency range (50 Hz − 2 kHz) [139]. For the specific items employed, a relative ac-dc deviation below 1×10^{-5} can be considered.

Voltmeters V_{in} and V_{out} The voltmeter sampling $v_{in}(t)$ is an Agilent 3458A with the autozero and autorange functions disabled; the one sampling $v_{out}(t)$ is an Agilent 34401A, also with autozero and autorange disabled. Both V_{in} and V_{out} are simultaneously triggered. The voltmeters are routinely calibrated, with traceability to the Italian national standard of DC voltage.

Trigger T The trigger is a purpose-built quartz digital synthesizer, with a frequency of about 950 mHz, calibrated against Italian national frequency standard.

4.1.4 Results

All the measurements were carried out in a shielded and temperature controlled laboratory at 23 °C. In order to avoid noise clipping that could cause a systematic error in the calibration, the currents $\pm I_{nom}$ were not chosen at decadic values, but with slightly lower nominal value (e.g. 95 pA instead of 100 pA). The amplifier A was calibrated for the transresistance nominal gains $R_{nom} = 10\,G\Omega$, $100\,G\Omega$, $1\,T\Omega$ and $10\,T\Omega$. Each gain was calibrated by running the system for about 50 cycles of $v_{in}(t)$, corresponding to around 10 h of measuring time.

Figures 4.4, 4.5 and 4.6 report, as example, the outcome of a calibration at $R_{nom} = 10\,G\Omega$, with $C_{nom} = 1\,nF$ and $I_{nom} = \pm 95\,pA$.

Figure 4.4 shows the time evolution of $v_{in}(t)$, measured by V_{in}, and $i(t)$ versus the measurement time.

In figure 4.5 is reported the error at the amplifier input $\Delta i(t)$, expressed as $\Delta i(t) = R_{nom}^{-1} v_{out}(t) - i(t)$, which is the discrepancy between the current reading $R_{nom}^{-1} v_{out}(t)$ and the calibration current $i(t)$.

Finally, figure 4.6 shows the relative deviation $\delta R = (R - R_{nom})/R_{nom}$ for the positive and negative half-cycles of $v_{in}(t)$. As calibration value, the average of δR over all measurement cycles is considered.

Table 4.2 reports the calibration outcome for different nominal transresistance gains and nominal currents. An increase of around 2.5×10^{-3} can be observed in the values of δR between an odd exponential of the gain and the following even. This fact can be explained as the contribution of a second stage of the FEMTO amplifier

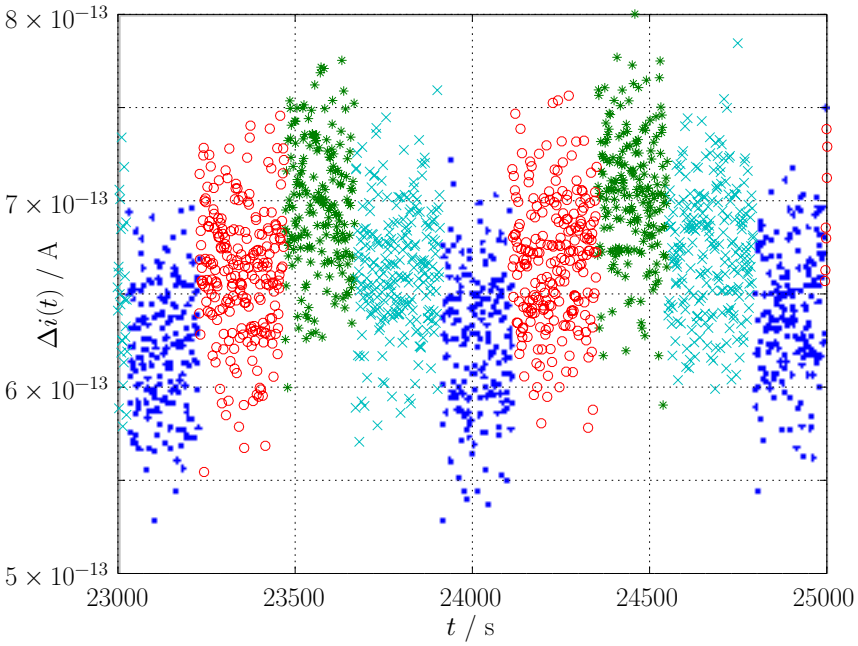

Figure 4.5: Time evolution of the error at the amplifier input $\Delta i(t)$. Different symbols represent the four different phases of $v_{\text{in}}(t)$: • corresponds to the positive ramp slope of $v_{\text{in}}(t)$ and to $i(t) = +I_{\text{nom}}$, ∗ to negative ramp slope and to $i(t) = -I_{\text{nom}}$, ◦ to $v_{\text{in}}(t)$ constant positive and to $i(t) = +0$, × to $v_{\text{in}}(t)$ constant negative and to $i(t) = -0$. The average of the phases $i(t) = +0$ and $i(t) = -0$ allows to estimate the offset of A. Reprinted by permission from [141] © 2018 IEEE.

that, when the exponential is even, has the gain equal to the unity, while when the exponential is odd it adds an extra 10-times amplification. The contribution of this second stage can correspond to this increase in the gain error.

The uncertainties reported in table 4.2 and table 4.3 are standard uncertainties (coverage factor $k = 1$). The accuracy levels obtained, which are of the order of 10^{-5}, are comparable, for the same nominal currents, to those reported in the literature [130, 148, 147, 146], with the main difference that for the cited methods it is also necessary the traceability to the voltage. Moreover, the achieved uncertainty level is two or three orders of magnitude better than the manufacturer specifications [16].

The strategy of calibration, the data evaluation process and the analysis of the uncertainty are reported in [131, 142].

A study about the temperature stability of the transresistance gain, performed with the capacitance-charging method, is reported in [23].

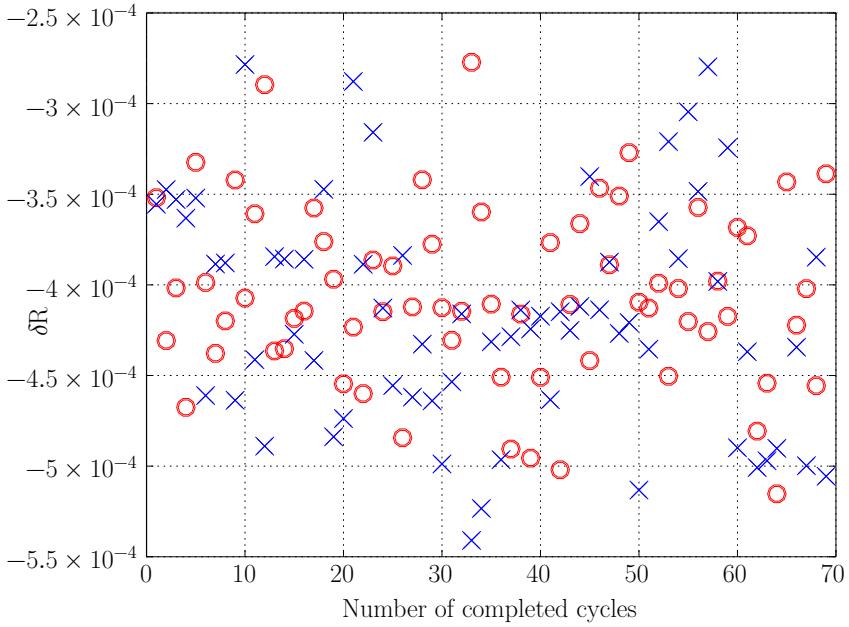

Figure 4.6: The deviation of the amplifier transresistance gain from its nominal value as function of measurement time. The deviation is evaluated for each positive (∘) and negative (×) semicycle of $v_{\text{in}}(t)$. Reprinted by permission from [141] © 2018 IEEE.

4.2 Calibration of a ULCA by means of a CCC

The calibration of the transresistance gain A_{TR} of a standard ULCA (section 3.2.2) is performed separately for the input and output stages.

The calibration set-up here described was based on a Magnicon 14 bit CCC. During the calibration the ULCA was kept in a temperature-controlled chamber at 23.0 °C. All data were collected and transferred to a computer via the interface bus IEEE-488. The CCC system is controlled by the Magnicon application *CCC viewer*.

4.2.1 Calibration of the ULCA input stage

The calibration of the input current gain G_I is performed in the *pure feedback configuration*, shown in figure 4.7, by using the CCC as current ratio standard.

The amplifier input current I_1 crosses the CCC primary winding with N_1 turns. The amplifier output current $I_4 = G_I I_1$ crosses the CCC secondary winding with N_4 turns. The auxiliary winding with N_2 turns is driven by the current source I_2, controlled by the SQUID in a feedback loop, to null the magnetic flux across the SQUID. The current I_2 is measured through the calibrated shunt resistor R_2

Table 4.2: Results of the transresistance amplifier calibrations

R_{nom}	I_{nom}	C_{nom}	δR
10 GΩ	95 pA	1 nF	$-4.35(35) \times 10^{-4}$
	−95 pA		$-4.62(40) \times 10^{-4}$
10 GΩ	9.5 pA	100 pF	$-4.64(34) \times 10^{-4}$
	−9.5 pA		$-4.54(59) \times 10^{-4}$
100 GΩ	9.5 pA	100 pF	$-3.05(3) \times 10^{-3}$
	−9.5 pA		$-3.09(4) \times 10^{-3}$
1 TΩ	9.5 pA	100 pF	$-2.90(3) \times 10^{-3}$
	−9.5 pA		$-4.32(3) \times 10^{-3}$
1 TΩ	0.95 pA	10 pF	$-3.29(9) \times 10^{-3}$
	−0.95 pA		$-3.14(7) \times 10^{-3}$
10 TΩ	0.95 pA	10 pF	$-5.77(8) \times 10^{-3}$
	−0.95 pA		$-5.76(6) \times 10^{-3}$
10 TΩ	0.095 pA	1 pF	$-5.83(18) \times 10^{-3}$
	−0.095 pA		$-6.03(16) \times 10^{-3}$

by the bridge-voltage detector V, measuring ΔV_2 with gain G. The current I_1 is periodically reversed to cancel possible offsets. The value of G_I can be expressed as

$$G_I = \frac{N_1}{N_4}\left(1 - \frac{\Delta V_2}{G}\,\frac{1}{R_2\,\Delta I_1}\,\frac{N_2}{N_1} + k\,\frac{N_A}{N_1}\right), \tag{4.4}$$

where ΔI_1 is the peak-to-peak amplitude of I_1. The last term within parentheses comes from an additional compensation circuit, not shown in figure 4.7, comprising a winding with N_A turns and a compensation factor k.

The ratio N_1/N_4 should be chosen close to the nominal transresistance gain G_I^{nom}. For the calibration of the standard ULCA, with $G_I^{\text{nom}} = 1000$, the following parameters were chosen to minimize the calibration uncertainty: $N_1 = 16000$, $N_2 = -4$, $N_4 = 16$ and $N_A = 1$; the chosen input current was $I_1 = \pm\ 12.97\,\text{nA}$, which resulted in a current $I_2 = \pm\ 12.97\,\mu\text{A}$.

4.2.2 Calibration of the ULCA output stage

The calibration procedure of the ULCA output transresistance R_{IV} exploits the *bridge configuration*, shown in figure 4.8, commonly employed for a standard resistor. The transresistance R_{IV} is compared with a calibrated standard resistor R_1.

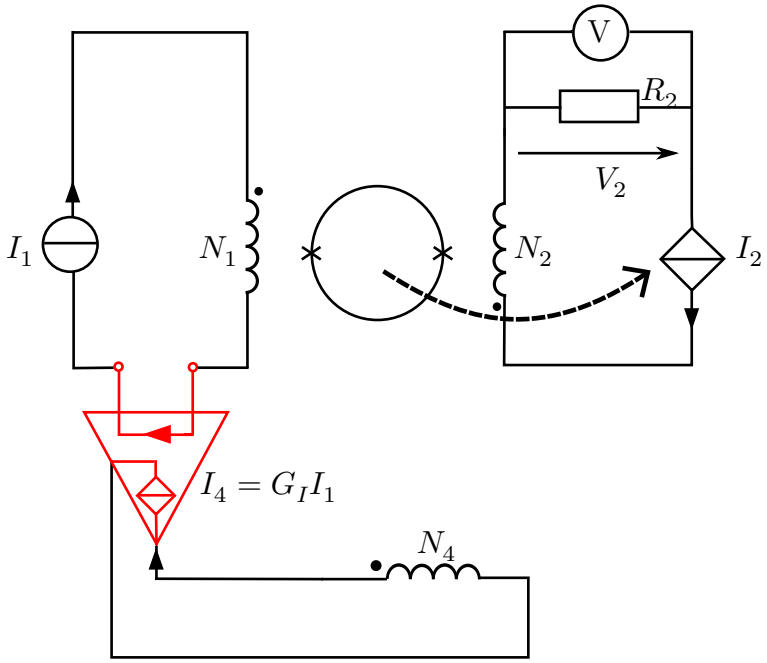

Figure 4.7: Principle schematic of the system employed for the calibration of the standard ULCA input stage, the binary compensation unit is omitted for simplicity. In red is depicted the input stage to be calibrated.

The amplifier input current I_2 crosses the CCC secondary winding with N_2 turns. The CCC primary winding with N_1 turns and the resistor R_1 are driven by the current source I_1, adjusted by the SQUID feedback loop to null the magnetic flux. The bridge unbalance voltage V is measured by the bridge-voltage detector having gain G. The current I_2 is periodically reversed to cancel possible offsets. The resistance ratio is given by

$$\frac{R_1}{R_{IV}} = \frac{N_1}{N_2}\left(1 + k\,\frac{N_A}{N_1}\right)\left(1 + \frac{\Delta V}{G\Delta(I_2 R_{IV})}\right), \tag{4.5}$$

where $\Delta(I_2 R_{IV})$ is the variation of the ULCA output voltage. Therefore, the transresistance gain of the ULCA is given by

$$R_{IV} = R_1 \frac{N_2}{N_1}\left[\left(1 + k\,\frac{N_A}{N_2}\right)\left(1 + \frac{\Delta V}{\Delta(I_2 R_{IV})}\right)\right]^{-1}. \tag{4.6}$$

The ratio N_1/N_2 should be chosen close to the nominal value of the ratio R_1/R_{IV}. For the calibration of the standard ULCA, with nominal values $R_{IV} = 1\,\mathrm{M\Omega}$ and $R_1 = 12.9\,\mathrm{k\Omega}$, the following parameters were chosen to minimize the calibration uncertainty: $N_1 = 52$, $N_2 = 4029$ and $N_A = 1$; the chosen input current was $I_2 = \pm 0.5\,\mu\mathrm{A}$, which resulted in a current $I_1 = \pm 38.74\,\mu\mathrm{A}$.

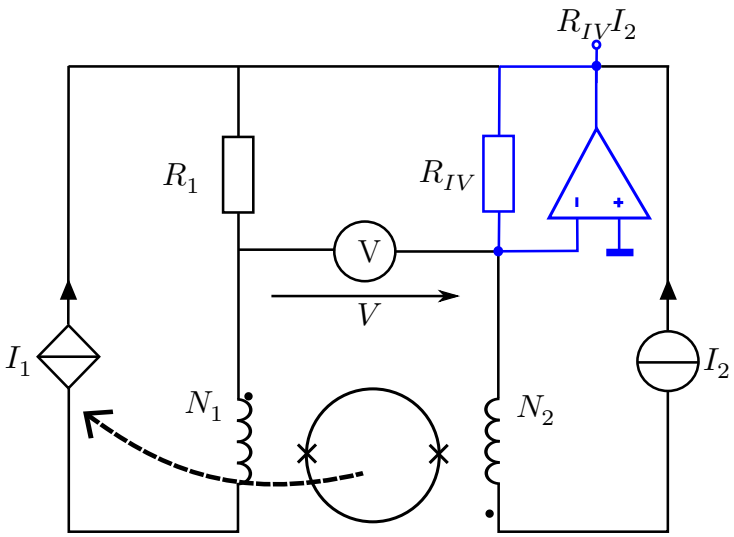

Figure 4.8: Bridge configuration schematic involved for the calibration of the standard ULCA output stage, the binary compensation unit is omitted for simplicity. In blue is represented the output stage of the ULCA with its resistance to be calibrated.

4.2.3 Instruments employed

14 bit CCC As reported in section 2.3, this type I CCC was developed by PTB in collaboration with Magnicon and it is the improved version of the previous 12 bit CCC [118]. This CCC (figure 4.9) represents the cutting edge of this technology.

In this CCC the wires forming the windings are made by a single-filament of NbTi in Cu matrix with a overall diameter (including the insulator) of 35 µm. The torus is made by a lead shield that overlaps 2.9 times and the inner and outer diameter are respectively 18.0 mm and 32.5 mm.

The SQUID chip has a size of 3×3 mm^2 and is mounted coplanar to the torus, together with the pick-up coil which is made by one Nb turn [101] (figure 4.9).

These elements are placed at the lower end of a cryogenic probe allowing to perform the measurements in a liquid helium dewar. On top of the probe there is a matrix box for the selection of 18 windings with a number of turns from 2^0 to 2^{13} and, in addition, 1, 17, 78 and 773.

The CCC is also equipped with an auxiliary circuit with a winding with N_A turns, called *binary compensation unit*. This unit performs a preliminary reduction of the unbalance of the bridge by introducing a current $I_A = kI_1$ which is a well-known fraction of the current I_1 [105, 106]. The value of k,

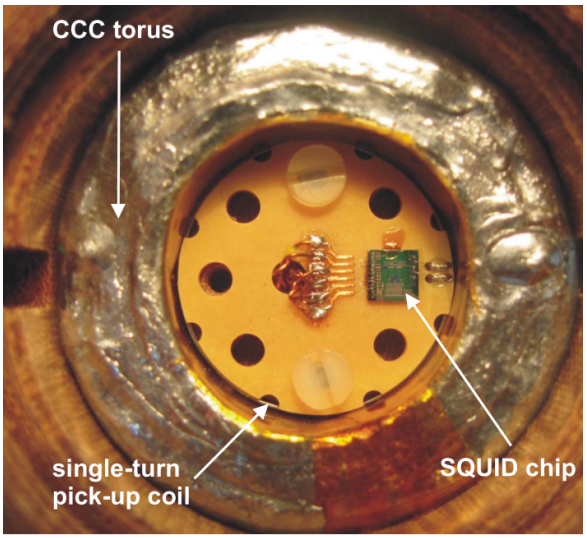

Figure 4.9: Picture of the bottom part of the 14 bit CCC probe available in PTB. It is clearly visibile the superconducting torus, the SQUID chip and the pick-up coil. Reprinted by permission from [101] © 2014 IEEE.

called *compensation factor*, is determined through a periodic calibration of the binary compensation network [106].

Standard resistors The resistors R_1 of figure 4.8 and R_2 of figure 4.7 are the same standard resistor with a nominal value of 12.9 kΩ, calibrated against a quantized Hall resistance by means of the 14 bit CCC with a relative accuracy of 10^{-8}. The resistor is temperature controlled at 23 °C.

Voltmeter For the acquisition of the output voltage V_{TEMP} of the on-board ULCA thermometer a Keysight 3458A is employed.

Thermostatic chamber During the calibration, the ULCA is kept in a Measurements International 930 air bath system.

Thermometer The temperature inside the air bath system is monitored by a high accuracy thermometer Isotech TTI-22 coupled with a platinum thermoresistance Pt100 Klasmeier 935-14-112.

4.2.4 Temperature dependence

To estimate the temperature coefficients of G_I and R_{IV}, these quantities were measured by changing the temperature of the air bath from 19 °C to 27 °C with 1 K steps. The amplifier temperature is acquired by the on-board thermometer which produces an output voltage V_{TEMP} recorded at each temperature.

Typically, for the standard ULCA ,the temperature coefficients of G_I and R_{IV} are of the order of parts in 10^8 [18].

4.2.5 Results

An example of the outcome of a standard ULCA calibration is reported in table 4.4. The relative deviation δA_{TR} from the nominal value is estimated as

$$\delta A_{TR} = (1 + \delta G_I)(1 + \delta R_{IV}) - 1, \tag{4.7}$$

where δG_I and δR_{IV} are the relative deviations of G_I and R_{IV} from their nominal values, that is, $G_I = G_I^{\mathrm{nom}}(1 + \delta G_I)$ and $R_{IV} = R_{IV}^{\mathrm{nom}}(1 + \delta R_{IV})$.

As shown in table 4.4, the relative standard uncertainty (including the type B uncertainty) of the calibration of G_I and R_{IV} is of 10^{-8} [111, 18, 102].

The value of δA_{TR} and its uncertainty are estimated by combining the results of the calibrated values of G_I and R_{IV}, obtaining a relative uncertainty of the order of 10^{-8} [18, 100].

Calibration of the second generation ULCAs

As mentioned in 3.2.2, several second generation ULCAs have been developed during the years, each of them with different features.

The calibration procedures for these new variants are exactly the same as the ones employed for the standard ULCAs. The main difference is in the different value of G_I and R_{IV} of the new versions; this implies that a different intensity of the currents I_1 and I_2 in the CCC is involved. Further details about the calibration of second generation ULCAs are reported in [103].

Table 4.3: Uncertainty budget for the calibration conditions: $R_{\text{nom}} = 10\,\text{G}\Omega$, $C_{\text{nom}} = 1\,\text{nF}$, $I_{\text{nom}} = \pm 95\,\text{pA}$.

	Source	Contribution to $u(\delta R)$	Type
	C calibration, frequency and temperature dependence	3.0×10^{-5}	B
	V_{in} sampling	5.0×10^{-6}	B
	Timebase T accuracy	1.0×10^{-6}	B
	C current leakages	1.0×10^{-5}	B
$I_{\text{nom}} = 95\,\text{pA}$	Reading noise	9.5×10^{-6}	A
$I_{\text{nom}} = -95\,\text{pA}$	Reading noise	1.6×10^{-5}	A
$I_{\text{nom}} = 95\,\text{pA}$	$u(\delta R) =$	3.4×10^{-5}	RSS
$I_{\text{nom}} = -95\,\text{pA}$	$u(\delta R) =$	3.6×10^{-5}	RSS

Table 4.4: Typical outcome for the calibration of a standard ULCA. The data reported are referred to measurements at 23 °C.

i	Name	$x_i \times 10^6$	$u(x_i) \times 10^6$
1	δG_I	-4.122	0.010
2	δR_{IV}	64.832	0.010
	δA_{TR}	60.710	0.014

Chapter 5

Single-parameter pumping of a GaAs-based pump

Semiconductor-based pumps are mainly fabricated using GaAs heterostructures or Si [24]: the pump involved in this work belongs to the first type and was fabricated at PTB. A detailed description of the fabrication and characterization of a similar pump can be found in [25].

The pump is based on a *quantum dot* (QD) [27, 26, 28]: a region with a size of 10 nm to 100 nm in which a small number of electrons, between one and few hundreds, can be spatially confined in all the three dimensions. The energy of electrons confined in such a small structure is quantized, that is, their excitation spectrum is discrete.

One way to achieve the three-dimensional confinement, firstly described in [29], comes after a previous reduction of the electron motion in two dimensions, creating a *two-dimensional electron gas* (2DEG).

A 2DEG can be obtained in a heterostructure by placing a n-doped AlGaAs layer sandwiched between an undoped layer of AlGaAs and a cap layer of GaAs (figure 5.1). This generates a quantum well formed by the undoped AlGaAs and the buffer layer of GaAs, obtaining the 2DEG [24, section 5.2.4]. The main advantage of these modulation-doped heterostructures compared to the homogeneously doped semiconductors, is the enhanced mobility of the electrons which is maintained also at low temperatures.

A quasi-one-dimensional region, called *transport channel*, is obtained in the 2DEG by shallow-etching the n-doped AlGaAs while the undoped layer is kept intact [30].

Three Schottky gates, called *entrance*, *exit* and *plunger gate*, are deposited on the transport channel. When negative voltages are applied to the gates the transport channel below the gates is depleted of electrons. This creates tunnel barriers with locally tunable height, thus forming the QD.

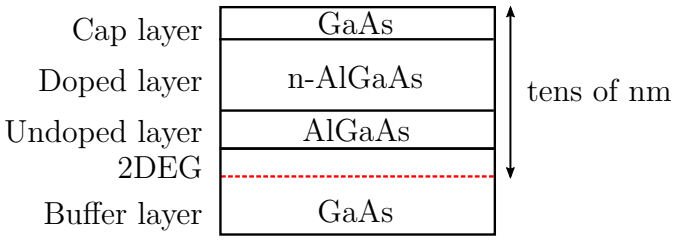

Figure 5.1: Cross-section diagram of the investigated modulation-doped heterostructure made of GaAs/AlGaAs. The 2DEG, which is located around 80 nm in depth from the sample surface, is shown with red line at the interface between the undoped AlGaAs and the GaAs substrate. The carrier density is $2.02 \times 10^{11}/\mathrm{m}^2$ and the mobility is $858\,\mathrm{m}^2/(\mathrm{V\,s})$.

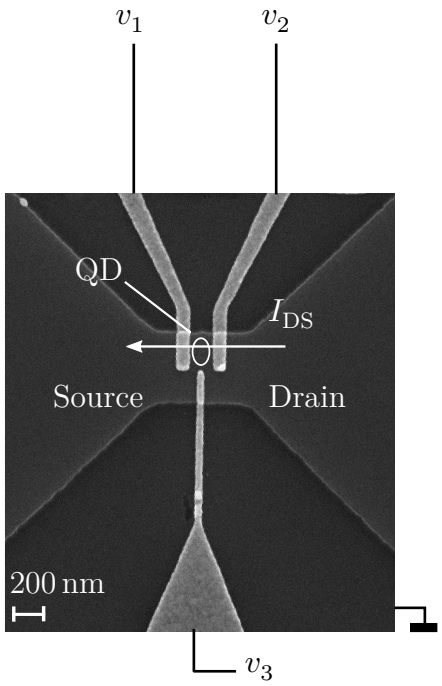

Figure 5.2: SEM micrograph of the single-electron pump measured: the darker zones are where the n-doped AlGaAs has been etched. The effective width of the transport channel, which is obtained by a shallow etch of about 40 nm, is slightly less than the geometrical one of 460 nm [30]. Overlapping the channel there are: the entrance gate (1), the exit gate (2) and the plunger gate (3). The gates are made of CrAu with a thickness 30 nm, and are deposited on top of the transport channel.

The remaining regions of 2DEG act as the source and drain reservoirs of electrons, filled up to the electrochemical potential μ_{S} and μ_{D}. In the pump operation

no bias voltage is applied, so that $\mu_S = \mu_D = 0$.

A micrography of the device can be observed in figure 5.2, showing the three gates to which voltages v_1, v_2, and v_3 are applied. The function of the plunger gate is to tune the transport channel effective width and to confine the electrons in the QD: typically a constant voltage V_3^{DC} is applied.

Figure 5.3 reports the energy diagram of the pump. The QD has discrete energy levels with heights $\mu_{QD}(1), \mu_{QD}(2), \mu_{QD}(3), ...$

By changing the height of one or both the entrance and exit barriers (i.e. changing the voltage applied to the gate), it is possible to change the populations of the QD levels. A proper cycling of the barrier height allows to transfer electrons between the source and the drain.

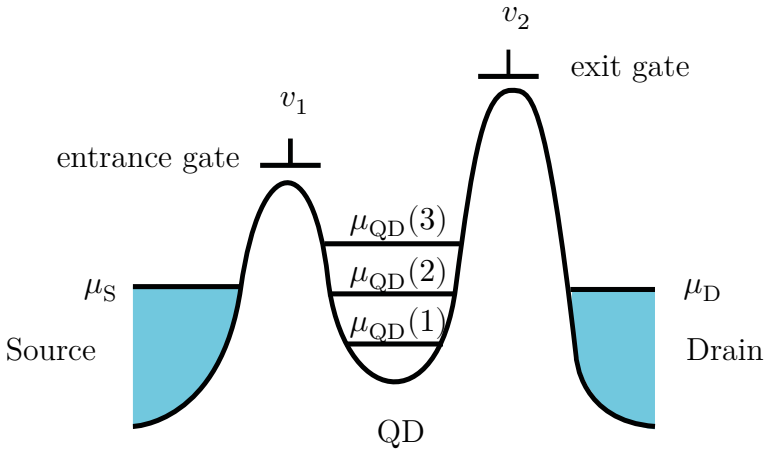

Figure 5.3: Representation of QD surrounded by two fixed tunable barriers. The plunger gate is not shown.

The *single-parameter pumping* employed in the experiment consists in the generation of a DC current by tuning the height of only one tunnel barrier by applying an RF-signal to the corresponding gate. In the simplest case a sinusoidal excitation $v_1^{AC}(t)$ with a DC bias V_1^{DC} is applied to the entrance gate, $v_1 = V_1^{DC} + v_1^{AC}(t)$, while the height of the exit barrier is kept fixed by $v_2 = V_2^{DC}$.

The pumping cycle is presented in figure 5.4: it consists in four different phases.

Loading phase (figure 5.4a) If the oscillation amplitude of $v_1^{AC}(t)$ is sufficiently high, μ_{QD} drops below μ_S and multiple electrons can fill the QD.

Decoupling phase (figure 5.4b) While the height of the barrier increases μ_{QD} are shifted above μ_S.

Isolation phase (figure 5.4c) The electrons in excess tunnel back to the source reservoir, while the remaining are trapped in the QD.

Discharging phase (figure 5.4d) The height of the entrance barrier overcomes the exit barrier height and allows the trapped electrons to escape into the drain reservoir.

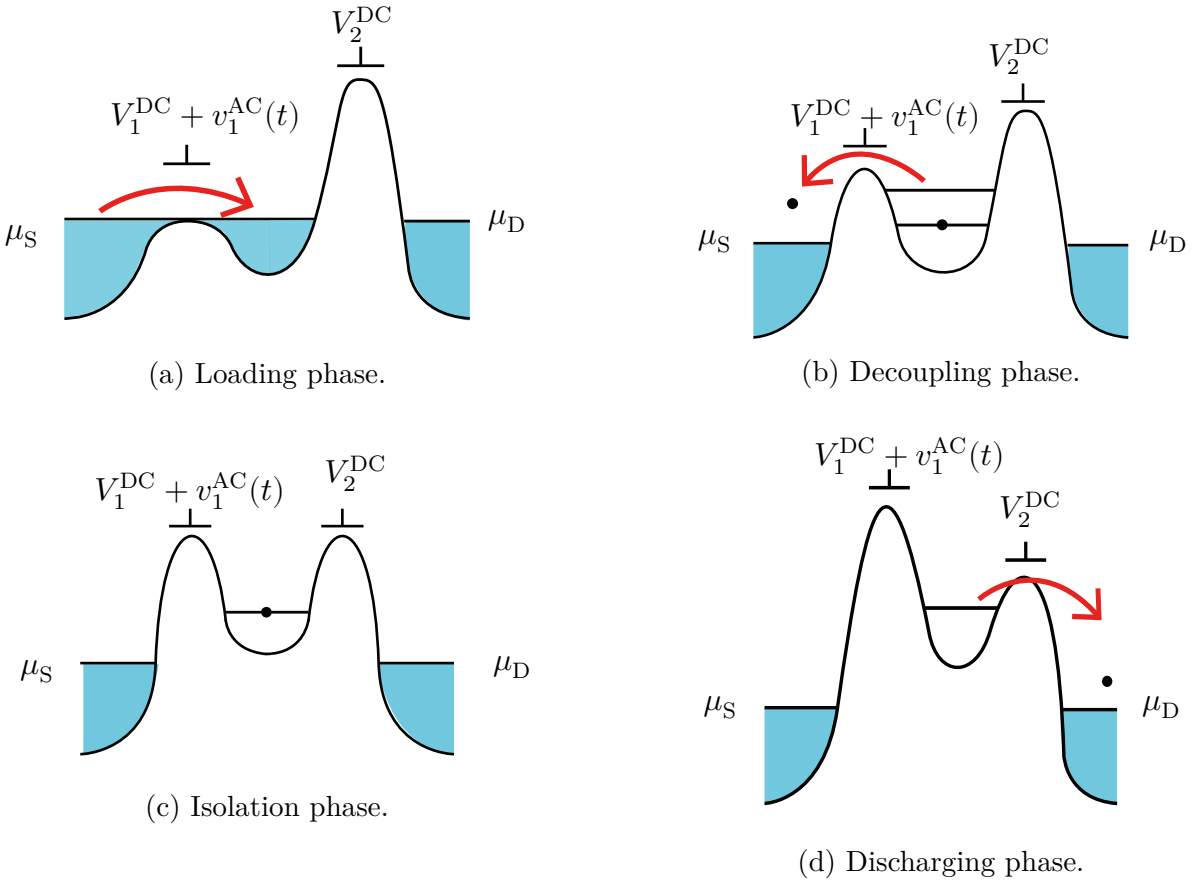

(a) Loading phase.

(b) Decoupling phase.

(c) Isolation phase.

(d) Discharging phase.

Figure 5.4: Schematic representations of the potential along the transport channel during the pumping cycle for the case $n = 1$. The plunger gate is not represented.

The current produced between the two reservoirs is quantized[1] as

$$I_{DS} = nef, \tag{5.1}$$

where f is the $v_1^{AC}(t)$ frequency and n is the integer number of electrons pumped per cycle. Since no bias voltage is applied, the direction of the current is only determined by which gate is driven by the RF-signal.

[1]The described pumping process is nonadiabatic, i.e. when the operating frequency is in the megahertz to gigahertz range, the parameters of the QD are not perfectly synchronized with it. This behaviour allows to obtain quantized and directional current by applying only a single periodic signal. More details in [32, 31]

Even if the mechanism is not fully understood yet, GaAs/AlGaAs pumps demonstrated an improvement of their quantization accuracy when a perpendicular magnetic field is applied [35, 36, 34, 33].

The theoretical treatment of the pumping error rates is a very complex subject, more details on this topic can be found in [32]. However, the errors that can occur during the pumping cycle are not taken into account as subject of this work.

Chapter 6

Single-electron current measurements

The aim of this chapter is to present the result of a 16 h current measurement of a GaAs-based pump within a single-electron experiment.

The set-up employed was specifically designed to perform high accuracy measurements: it is an improvement over [121].

One of the new set-up features is the *cross-switch chip*, an additional heterostructure embedded in the pump, which allows to perform non-stop measurements and remove current offsets. For this reason, the cabling system of the cryogenic probe was designed to accommodate all the interconnections needed to drive and measure the pump with the cross switch. The new cabling system was characterized with particular attention to the noise level introduced by the environment in the current cables. Two ULCAs, calibrated against a quantized Hall resistance, were employed to measure and amplify the current generated by the pump providing two output voltages. Two *Programmable Josephson Voltage Standards* (PJVs) were included in the set-up to perform potentiometric measurements of the ULCA outputs.

The outcome of the measurement is the deviation between the current produced by the pump and the nominal current.

Section 6.1 presents the overview of whole experiment, while sections 6.2, 6.3 and 6.4 report the details about the cross-switch chip, the new cabling system and the electronics employed in the experiment. The procedure used to measure the pump and the data anaysis performed are described in section 6.5. Finally, in section 6.6, the results achieved are presented.

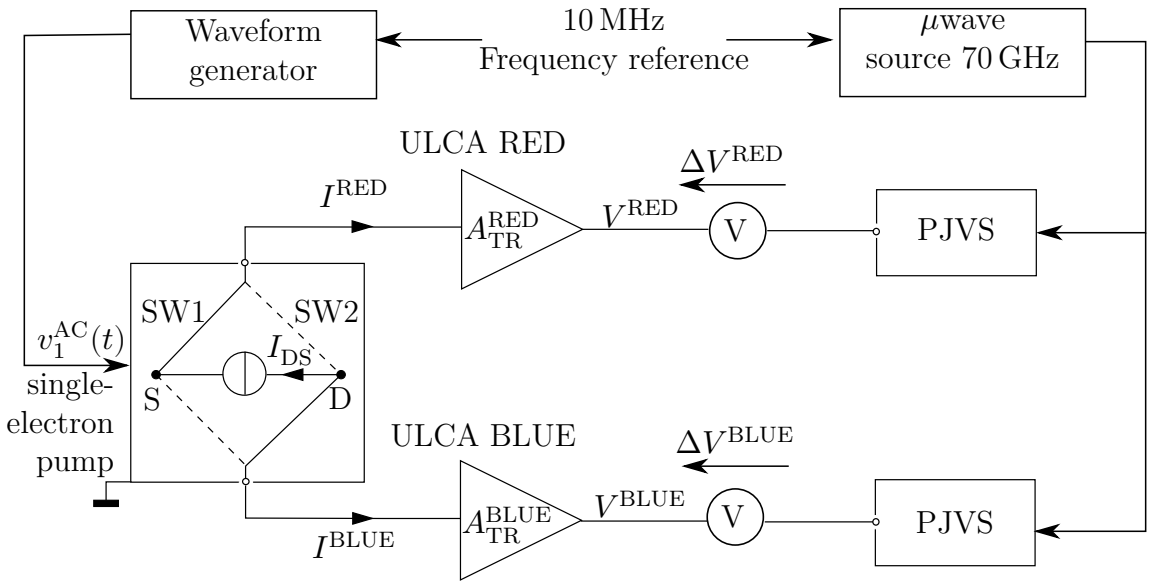

Figure 6.1: Simplified block diagram of the set-up for the potentiometric measurement involving the two ULCAs and the two PJVSs. The ULCAs convert the current in a voltage output compensated by the two different JPVSs: the difference is measured by two commercial voltmeters and transferred via IEEE-488 buses to a computer. All the electrical connections among the instruments are done by employing coaxial cables. The sample, the refrigerator, the case of the ULCAs and the two PJVSs are sharing the same ground. Furthermore, both the sample and the JPVSs share the same frequency reference.

6.1 Experiment

The block diagram of the experimental set-up for the measurement of the pump-generated current is reported in figure 6.1.

The pump is driven by a sinusoidal excitation $v_1^{\mathrm{AC}}(t)$ having a frequency of 625 MHz. The pump operates with a magnetic field of 12 T. According to (5.1) it produces a current $I_{\mathrm{DS}} \approx 100\,\mathrm{pA}$ when the pump is operating with n=1. Two ULCAs, labelled ULCA RED and ULCA BLUE, measure I_{DS} through the switches SW1 and SW2 and produce the output voltages

$$V^{\mathrm{X}} = A_{\mathrm{TR}}^{\mathrm{X}}\, I^{\mathrm{X}}, \tag{6.1}$$

where X = RED, BLUE, I^{X} are the ULCAs input currents and $A_{\mathrm{TR}}^{\mathrm{X}}$ are the transresistance gains with nominal values of 1 GΩ. With these values $|V^{\mathrm{X}}| \approx 100\,\mathrm{mV}$, with a sign depending on the positions of SW1 and SW2.

The voltages V^{X} are measured by comparison with the reference voltages $V_{\mathrm{J}}^{\mathrm{X}}$, $|V_{\mathrm{J}}^{\mathrm{X}}| < |V^{\mathrm{X}}| \approx 100\,\mathrm{mV}$, generated by two PJVSs. The two voltages are chosen so that $V_{\mathrm{J}}^{\mathrm{RED}} = -V_{\mathrm{J}}^{\mathrm{BLUE}}$ with a sign that depends on the positions of SW1 and SW2.

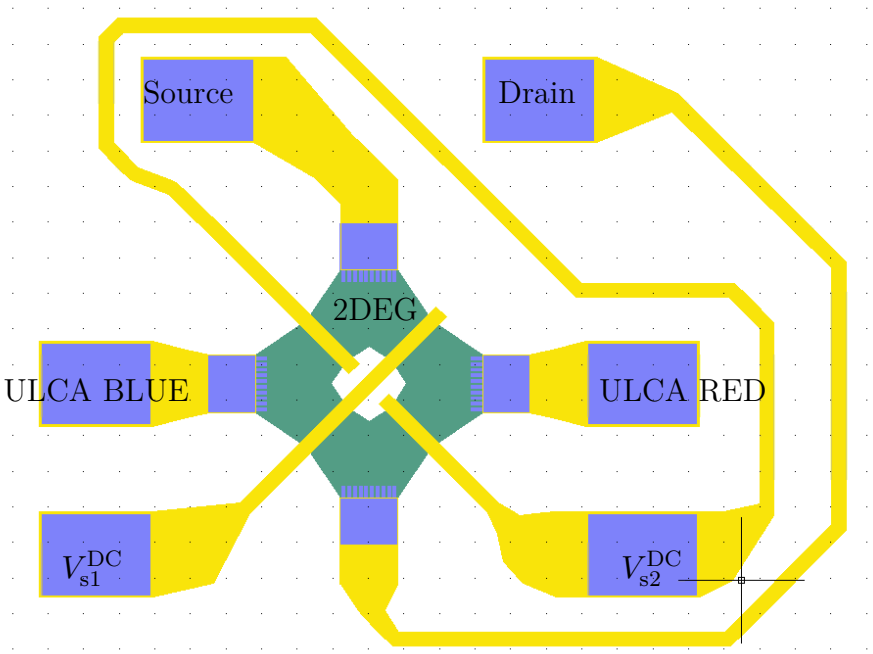

Figure 6.2: CAD design of the cross switch: there is the 2DEG ring (green), the CrAu leads (yellow), the Ni/Ge/Au ohmic contacts and the corresponding pads (blue).

The deviations of V^{X} from V_{J}^{X},

$$\Delta V^{X} = V^{X} - V_{J}^{X}, \tag{6.2}$$

have a magnitude of tens of µV. Thanks to the potentiometric measurement between the PJVS and the ULCA output voltages, the contribution of the gain uncertainty of both multimeters is minimized.

The switches SW1 and SW2 are employed to periodically reverse the current direction at the ULCAs inputs and to cancel the offsets through differential measurements.

6.2 Cross-switch chip

The switches SW1 and SW2 of figure 6.1 are implemented with a cross-switch chip, which is a device fabricated on a separate substrate with respect to the pump.

The structure of the cross-switch chip is shown in figure 6.2. The device is made of a GaAs/AlGaAs heterostructure with a 2DEG carrier density of $2.26 \times 10^{11}/\mathrm{m}^2$ and a mobility of $736\,\mathrm{m}^2/(\mathrm{V\,s})$. Its main characteristic is the presence of a 2DEG ring in the middle of a shallow-etched region. The 2DEG ring is connected to four

pads by means of Ni/Ge/Au ohmic contacts and CrAu leads. Two of the pads are then connected to the source and drain terminals of the pump and two to the inputs of the ULCAs.

On top of the 2DEG there are two CrAu leads biased at voltages V_{s1}^{DC} and V_{s2}^{DC} for the control of the switches. These voltages allow to deplete the 2DEG region below the control leads, thus forcing the current to flow through two different paths: when $V_{s1}^{DC} = 0$ and $V_{s2}^{DC} = -400\,\mathrm{mV}$ the switches are connected as in figure 6.3a; when $V_{s1}^{DC} = -400\,\mathrm{mV}$ and $V_{s2}^{DC} = 0$ the switches are connected as in figure 6.3b. In this way the two ULCAs measure the same current I_{DS} but in the opposite direction.

By periodically operating the switches to reverse the ULCAs input currents, it is possible to perform a continuous measurement. This is called a *PLUS-MINUS* measurement process. Compared to the *ON-OFF* offset removal technique, in which the pump is periodically turned on and off [48, 36, 11, 121, 119, 12, 13], the PLUS-MINUS technique doubles the signal-to-noise ratio, allowing to reduce the type A uncertainty.

Figure 6.4 shows a schematic diagram of the connections of the cross switch to the pump and the control voltages.

6.3 Cryogenic probe

The cryogenic probe involved in the design of the new cabling system is a KELTLM34 Melcher probe 4 which belongs to a KelvinoxTLM dilution refrigerator of Oxford Instruments. More details regarding the refrigerator and the probe are given in section B.1 and section B.3.

The probe structure can be divided in four main parts: the *stainless steel part*, the *1K-pot region*, the *dilution unit* and the *sample holder region* (figure B.1).

To drive the pump and to measure the generated current, the new cabling system required the fabrication of

- two independent RF lines[1]
- two signal lines to measure I_{DS} by means of the ULCAs
- 24 DC lines for driving $V_{1,2,3}^{DC}$, $V_{s1,s2}^{DC}$ and for the sample diagnostic lines[2]

[1] As discussed in chapter 5, to perform the single-parameter pumping process only $v_1^{AC}(t)$ is necessary, nevertheless two RF-lines were fabricated to create a system also usable for driving pumps with the periodic modulation of both the entrance and exit gates.

[2] Of those 24, only five lines were necessary to perform the experiment described in this work. The choice to have 24 was done to allow future measurements of more complex devices.

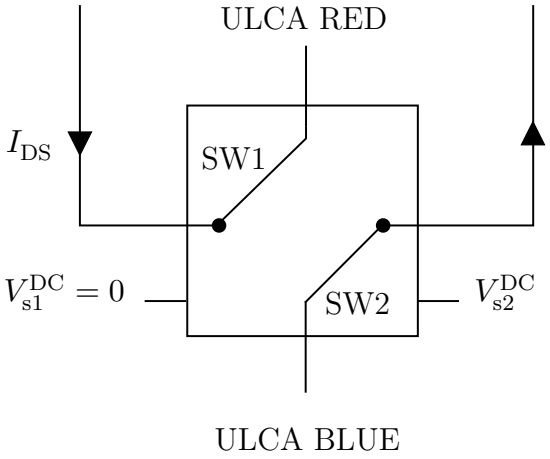

(a) Path followed by I_{DS} when SW1 is connected to the ULCA RED and SW2 is connected to ULCA BLUE.

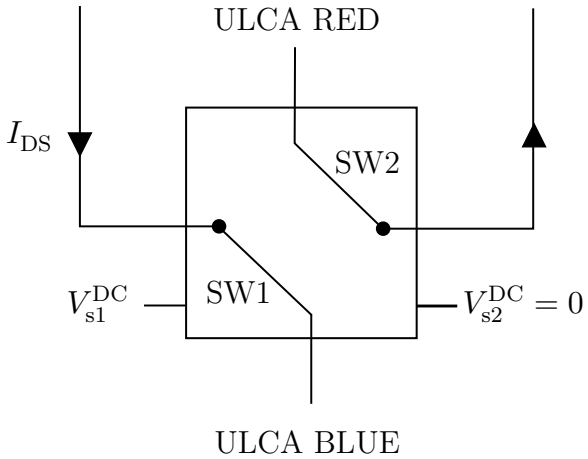

(b) Path followed by I_{DS} when SW1 is connected to the ULCA BLUE and SW2 is connected to ULCA RED.

Figure 6.3: Schematic representations of the cross-switch chip behaviour driven by $V_{s1,s2}^{\mathrm{DC}}$.

A description of the employed cables and of their testing process is reported below.

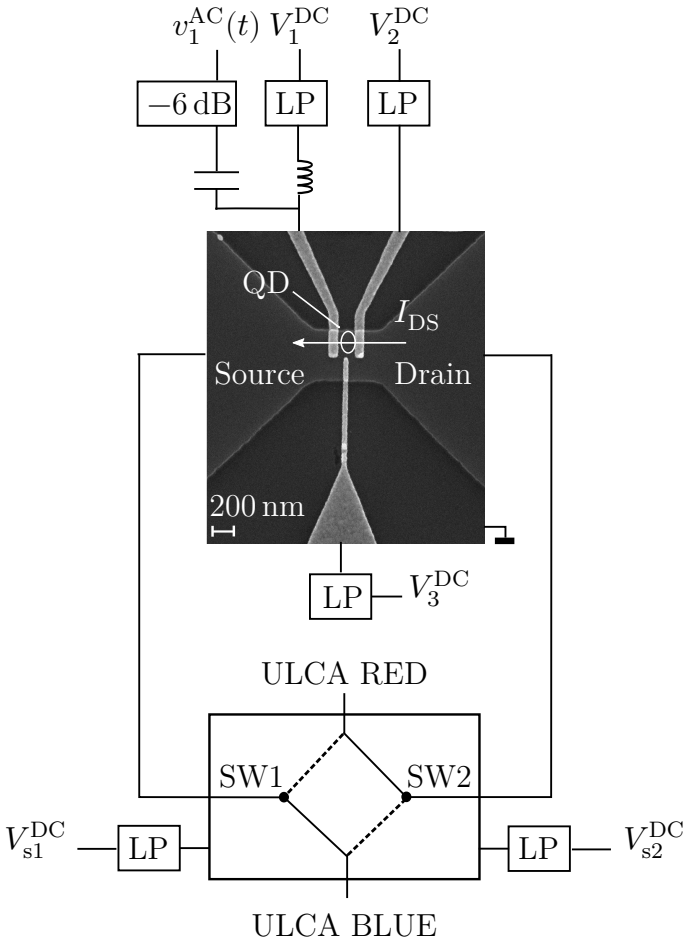

Figure 6.4: Schematic representation of the connections necessary to drive the pump and the cross switch. The current generated is acquired by the ULCA RED and ULCA BLUE. LP represents the low-pass filters applied to the gate voltages $V_{1,2}^{DC}$ and to the voltages driving the cross-switch chip $V_{s1,s2}^{DC}$.

6.3.1 RF lines

Two RF lines, named *line A* and *line B*, were fabricated. They pass through all the length of the probe: from the top flange of the stainless steel part at room temperature to the sample holder at few mK (figure B.4).

Two different semi-rigid coaxial cables were employed

- the Elspecs stainless steel cables mod. AN50085
- the Coax Co., LTD NbTi cables mod. SC-219/50[3]

[3]The NbTi cables are often used in cryogenic systems as thermal decouplers: when the NbTi

Details and specifications of the coaxial cables are reported in section B.4.1.

Cable testing

To check the quality of the RF lines fabricated, a time-domain reflectometer (TDR) was employed. This instrument is used to locate and characterize discontinuities in metallic cables, connector or other electrical paths. Its working principle is based on sending an incident signal through the conductor and acquire its reflections. If the impedance of the conductor is uniform, no reflections will be received by the source. Therefore, by observing the magnitude of the reflected signal, it is possible to estimate the variation in the conductor impedance and thus, the magnitude of the discontinuity.

In this specific case, a Tektronix DSA8300 Spectrum Analyzer was employed to inspect the impedance of each RF line to observe possible damages in the structure of the cables.

The result of this analysis can be observed in figure 6.5 as a function of the cable length. In both of the lines the cable assemblies showed minimal impedance deviations from 50 Ω, which is the typical impedance value for the standard coaxial cables employed in the radio frequency field. The deviations appear exactly in correspondence of the positions of the connectors. This suggests that no damages or discontinuity are present in the newly fabricated RF lines of the probe. The initial part and the terminal part of the RF lines are made evident by the extreme increase of the impedances showed in the figures.

6.3.2 Signal lines

Two signal lines, named as *RED* and *BLUE line*, were fabricated by using the same assembly of three coaxial cables, whose choice was made based on the noise analysis performed in [21]. As for the RF lines, also the signal lines cross all the length of the probe (figure B.6 and figure B.7).

Three types of coaxial cables were employed

- Lemo mod. 280630
- Thermocoax® mod. 1 Nc. Ac. 0.5[4]

becomes superconducting (T_c = 10 K and B_c = 15 T) its thermal conductivity is extremely low [122]. Therefore it is recommendable to use NbTi cables to minimize the heat transport across the 1K-pot. Furthermore, the NbTi cables are used only in 1K-pot region since the magnetic field generated from the coils across the dilution unit and in correspondence of the sample would break their superconductivity.

[4] A detailed description on the microwave filtering properties of Thermocoax® coaxial cables, often employed in single-electron experiments, can be found in [43].

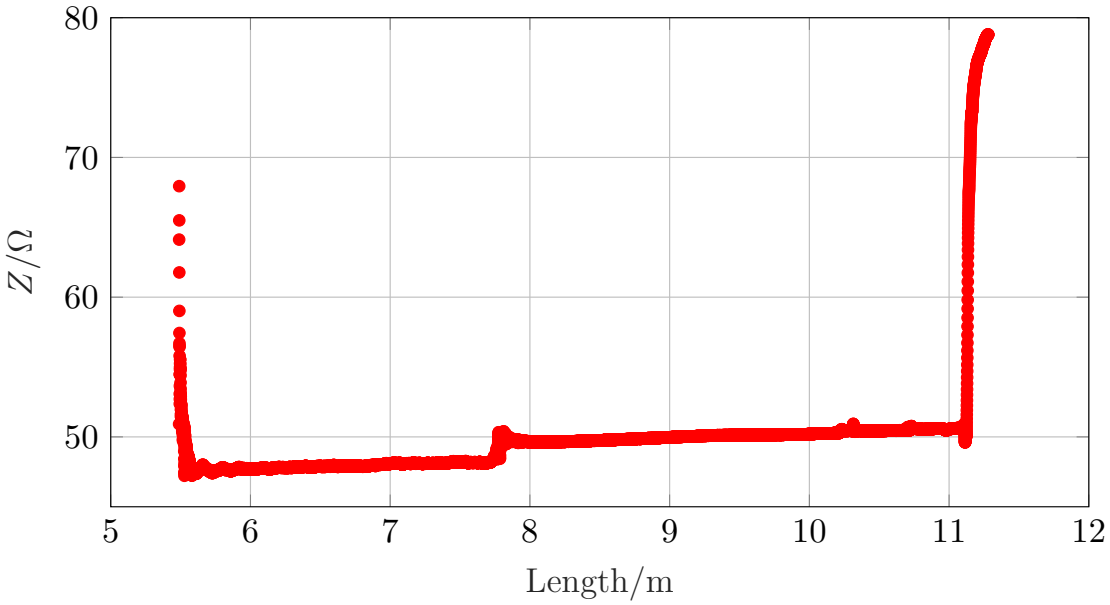

(a) Line A

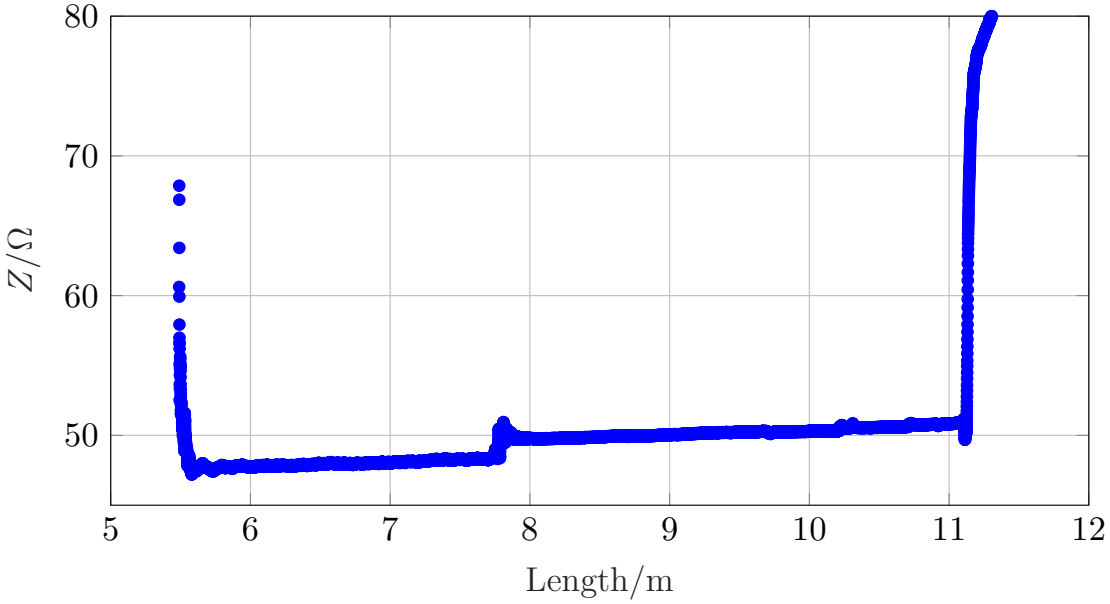

(b) Line B

Figure 6.5: Time Domain Reflectometry of the new RF lines. both the signals were acquired with an attenuator of −6 dB.

- Single filament NbTi wire in copper matrix (insulated).

Details and specifications of the coaxial cables are reported in section B.4.2.

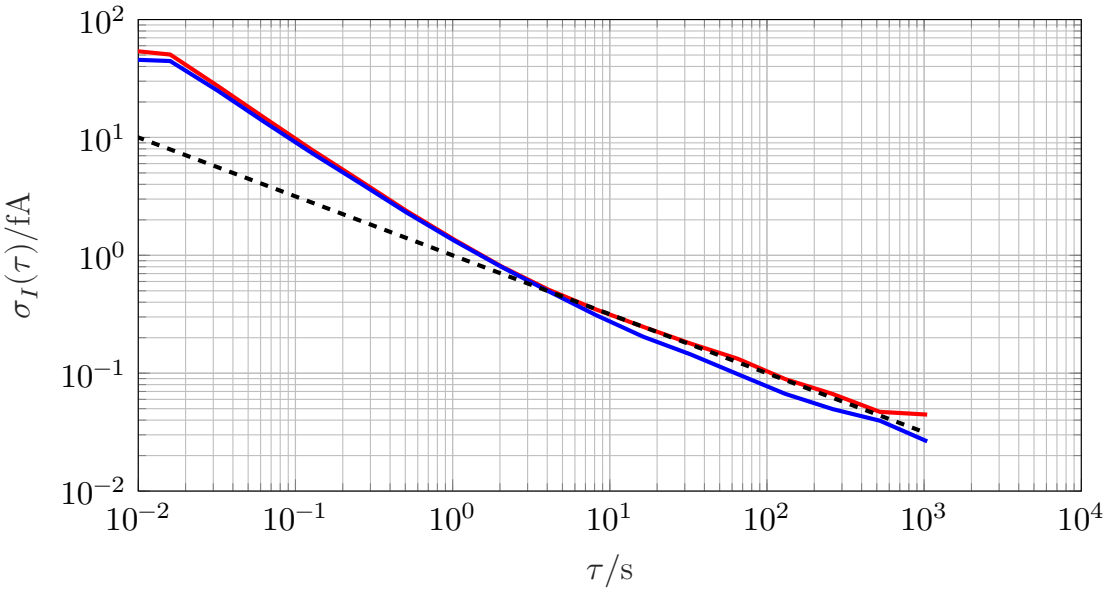

Figure 6.6: Plot of the Allan deviation of the current noise of the RED (—) and BLUE line (—). Dashed line indicates. Dashed line represents a reference for the white noise slope.

Cable testing

The characterization of the noise level in the signal lines helps to have an estimation on how much the experimental set-up can affect the lines dedicated to carry I_{DS}.

As discussed in section 3.3.3, a low-bias ULCA (section 3.2.2) was employed for measuring the noise level in both of the signal lines. The ULCA was shielded in a Mu-metal box and connected to the each line by means of a Bedea coaxial cable (specifications in B.5) also shielded in Mu-metal, to replicate the best experimental conditions found in section 3.3.2. The output of the ULCA was collected by a Keysight 34410-A multimeter with a sampling time of around 1 ms.

The probe was cooled down at around 70 mK on the mixing chamber and with 12 T magnetic field active. On the sample holder was mounted a GaAs/AlGaAs pump with $V^{\mathrm{DC}}_{1,2,3} = v^{\mathrm{AC}}_1(t) = 0$ and without cross-switch chip: these conditions led the device to behave like an open circuit.

The Allan deviation, estimated on the data acquired, is shown in figure 6.6. Since the reversing time of the current for the single-electron experiment was chosen to be 40 s (section 6.5.2), to this time interval the current noise level in the cables reaches around

- 0.18 fA for the RED line
- 0.16 fA for the BLUE line.

Comparing figure 3.12 and figure 6.6 it can be noticed that, at 40 s, the noise level coming from measuring set-up is not a limiting factor on the accuracy of the single-electron current measurement: it is lower than that of the low noise ULCA employed in the experiment.

6.3.3 24 DC lines

The 12-pair of constantan woven loom wires[5] were employed to cover all the probe length.

In single-electron experiments, radiations with a frequency of 1 GHz and above belong to the energy scale comparable with the one driving the electronic transport: they would provide enough energy to the electrons in the QD to trigger spurious events. To avoid the heating up of the electrons in the pump, that would generates unwanted events, all the lines were provided with two filtering stages

- at room temperature with 1 MHz low-pass filters
- at cryogenic temperature by means of the so-called *low-pass filter PCB* also provided with around 1 MHz low-pass filters, shown in figure B.8 and figure B.9.

6.4 Electronics

This section contains a list of the instruments necessary at the operation of the experiment, which are shown in figures 6.7 and 6.8. In figure 6.1 not all the instruments are shown.

Waveform generator A The waveform generator Tektronix AWG 7102 with an attenuation of −6 dB is employed for applying the periodic excitation $v_1^{\mathrm{AC}}(t)$. As frequency reference of the generator is used the 10 MHz coming from the primary caesium frequency standard. The merging of the signals V_1^{DC} and $v_1^{\mathrm{AC}}(t)$ is done employing a bias T integrated directly in the sample holder.

DC voltage source B To generate the DC voltage signals $V_{1,2,3}^{\mathrm{DC}}$ and $V_{\mathrm{s1,s2}}^{\mathrm{DC}}$ a purpose-built DAC system is employed. It is made by nine DAC cards plus one that allows the remote control by the PC using a USB port. The set-up is design to support up to 24 DC signals when the appropriate number of DAC cards are added (see 6.3.3).

Switch board C It is a purpose-built board used to apply and control $V_{1,2,3}^{\mathrm{DC}}$ and $V_{\mathrm{s1,s2}}^{\mathrm{DC}}$.

[5] The wires were provided by Oxford Instrument.

Transresistance amplifiers G The ULCA RED and ULCA BLUE are two low noise ULCAs. Both the ULCAs and the cables connecting them to the probe are shielded in Mu-metal (see 3.3.2). They are periodically calibrated with the 14 bit CCC available in PTB as discussed in 4.2.

Programmable Josephson Voltage Standards Two PJVSs (figure A.2) are embedded in the set-up, both of them have 1 mV voltage output. More details about the PJVSs can be found in A.1.1. The output voltage generated by the two PJVSs can be considered with an uncertainty of 1 part in 10^8 [98]. The operation of the two PJVs is verified periodically.

Voltmeters D, E Four voltmeters are involved in the experiment.

- Two Keysight 3458A are used to measure ΔV^{X} the difference between the voltage produced by the ULCAs and the voltage produced by the PJVSs. This is possible thanks to a couple of self-made boxes carrying the signals V^{X} and $V_{\mathrm{J}}^{\mathrm{X}}$ at each input of the multimeters (figure 6.7 F). To keep the voltage measurements more stable and not exposed to temperature fluctuations, two Teflon cases are employed to shield the boxes at the input electrodes of the multimeters. The gain of the two multimeters is periodically calibrated by using the two PJVSs: the only remaining effect is the drift of the characteristics of the multimeters.
- Two Keysight 34410-A are employed for recording the voltage signal $V_{\mathrm{TEMP}}^{\mathrm{X}}$ coming from the on-board thermometers of the two ULCAs.

6.5 Measurement procedure and data analysis

6.5.1 Operating parameters

The operating parameters of the experiment are established as follows. In order to set the operating point of the pump at $n = 1$, a sweep of the exit gate voltage V_2^{DC} was performed keeping $V_1^{\mathrm{DC}} = -160\,\mathrm{mV}$, $V_3^{\mathrm{DC}} = -120\,\mathrm{mV}$ and measuring the generated current with the two ULCAs. Figure 6.9 shows the resulting characteristic $I^{\mathrm{X}}(V_2^{\mathrm{DC}})$: two current plateaus corresponding to $n = 1$ and $n = 2$ are visible.

As described in [41], the data presented in figure 6.9 can be modelled in the range $0.9 < \langle n \rangle < 1.1$, being $\langle n \rangle$ the average number of transferred electrons per cycle, as the sum of two exponential functions

$$\frac{I_{\mathrm{mod}}(V_2^{\mathrm{DC}})}{ef} = 1 - e^{-\alpha_1(V_2^{\mathrm{DC}} - x_1)} + e^{\alpha_2(V_2^{\mathrm{DC}} - x_2)}, \tag{6.3}$$

where α_1, α_2, x_1, x_2 are the parameters of the model.

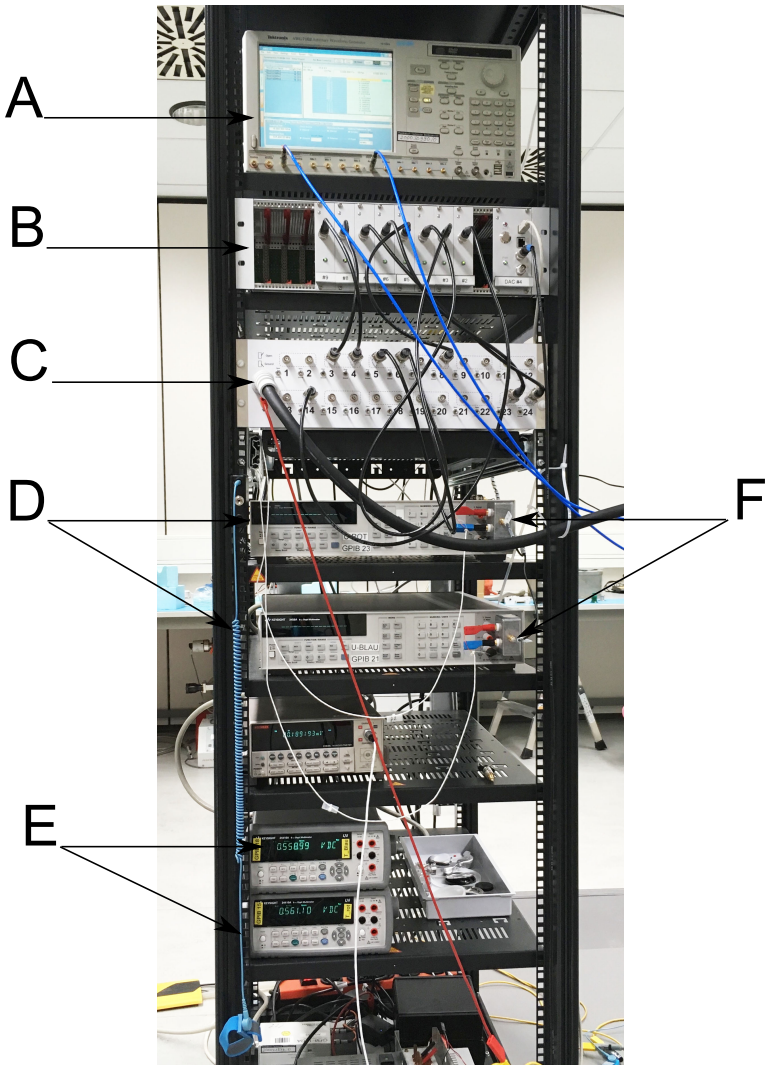

Figure 6.7: Picture of the instruments employed in the set-up. It shows the waveform generator (A), the DAC system (B), the switch board (C), the two voltmeters (D) measuring the deviation of the ULCAs from the PJVs voltages through the boxes (F), the two voltmeters for measuring the internal temperature of the ULCAs (E).

In the works presented in [121, 119], the inflection point of the fit (6.3) on the data is considered as the optimum working point of the pump, i.e. the most stable point of operation in terms of variation of V_2^{DC}.

However, the exact location of the optimum working point cannot be determined uniquely: it may vary depending on the chosen model to fit the data, as shown in [45], figure 5. Therefore, for the pump measurement presented in this thesis, the optimum value was chosen to approximate the inflection point of figure 6.9 from the transformed data of figure 6.10.

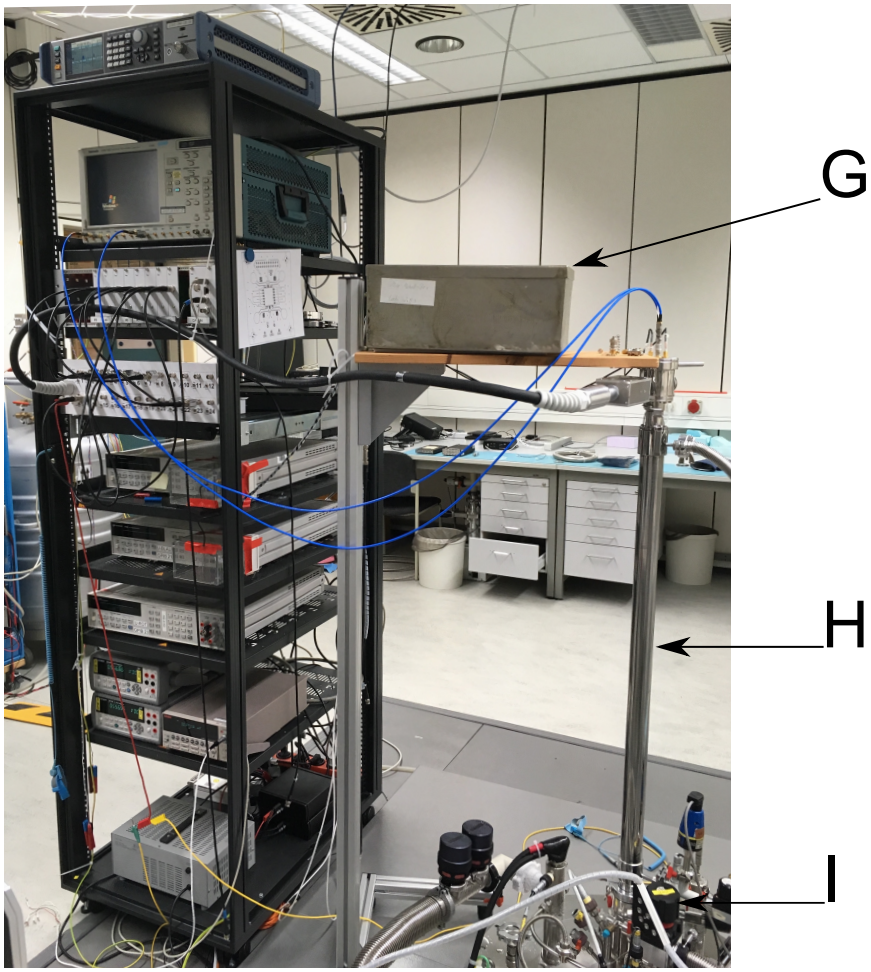

Figure 6.8: Picture of the set-up from another prospective. It shows the Mu-metal box containing the two ULCAs (G), the cryogenic probe (H) inserted in the KelvinoxTLM dilution refrigerator (I).

6.5.2 Measurement sequence

The measurement sequence starts with the switch SW1 connected to the ULCA RED and the switch SW2 connected to the ULCA BLUE (figure 6.3), so that $\Delta V^{\mathrm{RED}} > 0$ and $\Delta V^{\mathrm{BLUE}} < 0$.

The switches are periodically reversed, and during each phase 200 samples of the voltages ΔV^{X} are acquired by the two voltmeters (figure 6.11a). The sampling time is 0.2 s and the autozero function is activated every 10 samples to remove any internal offset error. This gives an overall measurement time for each phase of about 40 s. To guarantee that the ULCAs are settled during the data acquisition,

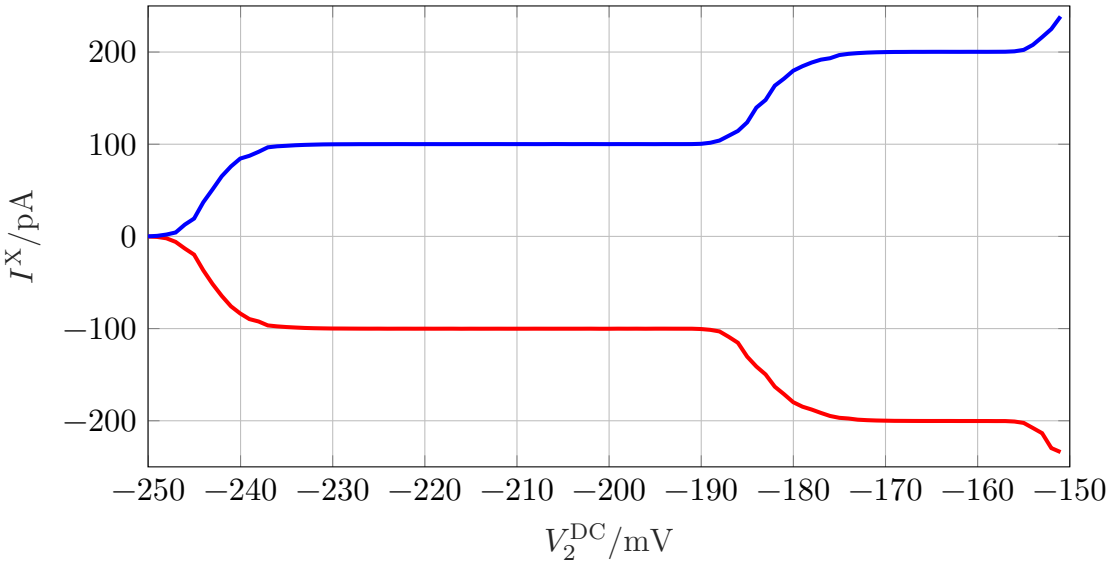

Figure 6.9: Current measured by the ULCA RED (—) and ULCA BLUE (—) as a function of the exit gate voltage V_2^{DC}. The plateaus correspond to the transfer of an integer number of charges ($n = 1$ and $n = 2$) through the pump.

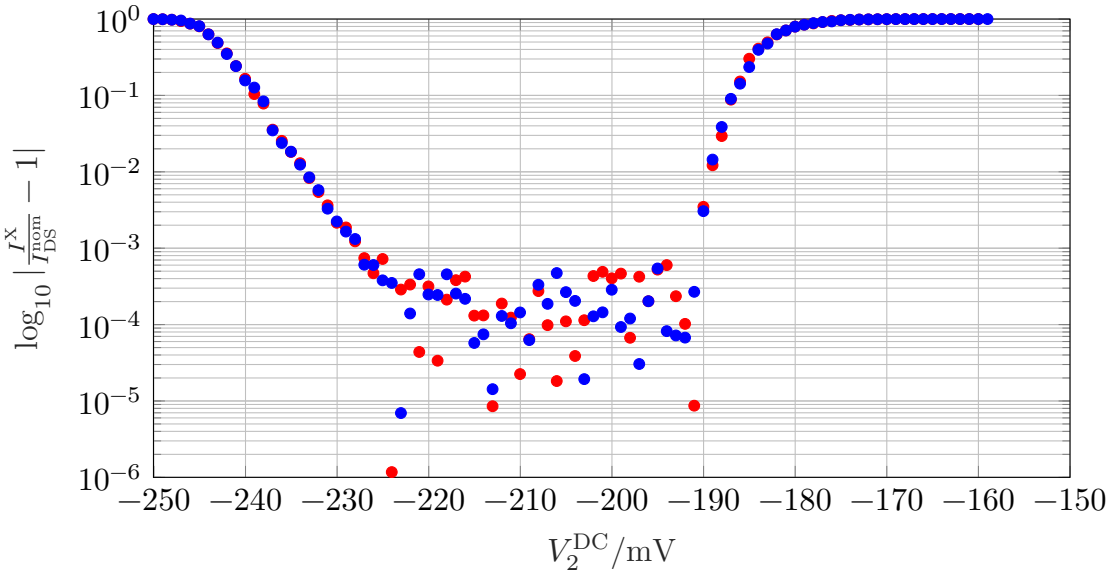

Figure 6.10: Semilogarithmic plot of the absolute value of the deviation between the measured current I^{X} and the nominal nominal values $I_{\mathrm{DS}}^{\mathrm{BLUE,nom}} = ef$ and $I_{\mathrm{DS}}^{\mathrm{RED,nom}} = -ef$.

as suggested in [18], the first 20 points of each phase are discarded from the data analysis (figure 6.11b). The remaining samples are labelled $\Delta V_{\kappa,l}^{\mathrm{X}}$ with $\kappa = 1, \ldots, K$

being an index indicating the phase and $l = 1, \dots, L$ indexing the effective samples in each phase.

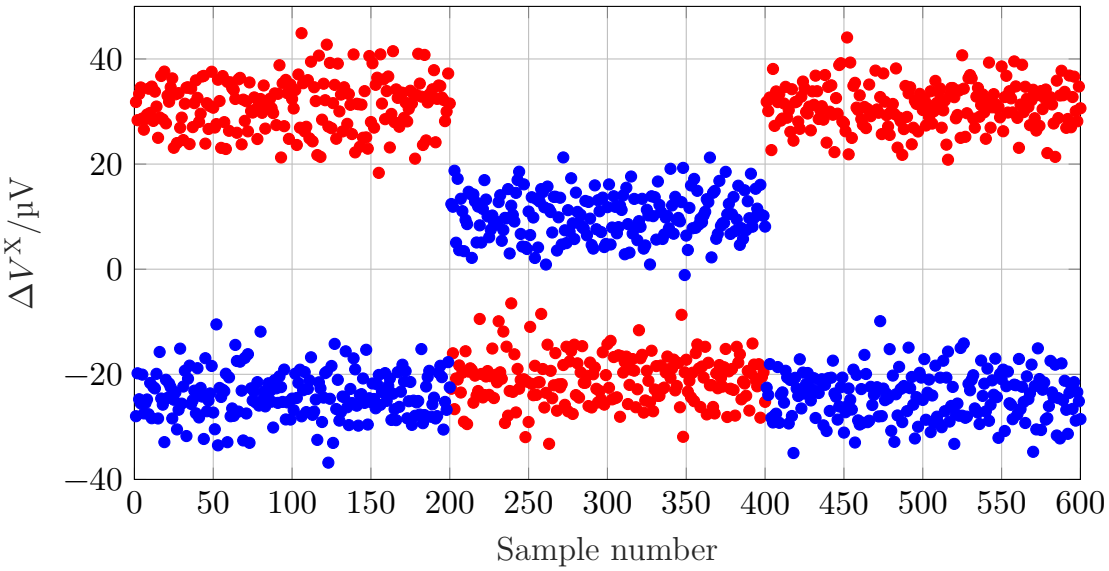

(a) All the data points are reported.

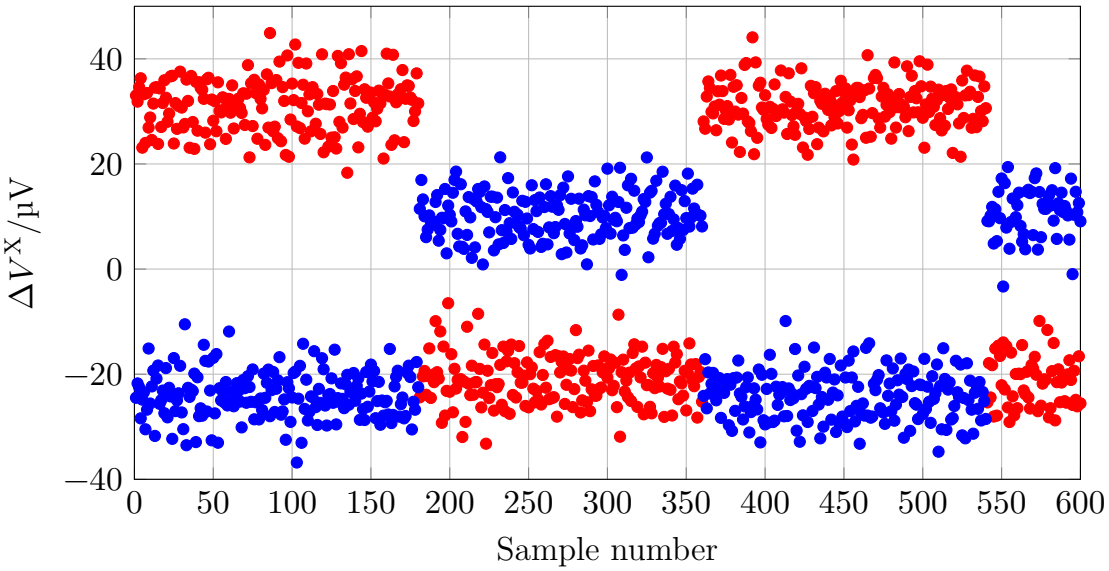

(b) The first 20 data points of each dataset are discarded.

Figure 6.11: Example of a data acquisition of ΔV^X: the symbol (•) corresponds to ΔV^{RED}, while (•) represents ΔV^{BLUE}. The red and blue plateaus are not exactly symmetrical due to the difference in the gain calibrations of the amplifiers.

From (6.1), the samples $V^{\mathrm{X}}_{\kappa,l}$ of the ULCAs output voltages are given by

$$V^{\mathrm{RED}}_{\kappa,l} = \Delta V^{\mathrm{RED}}_{\kappa,l} + (-1)^{\kappa} V_{\mathrm{J}}, \tag{6.4}$$

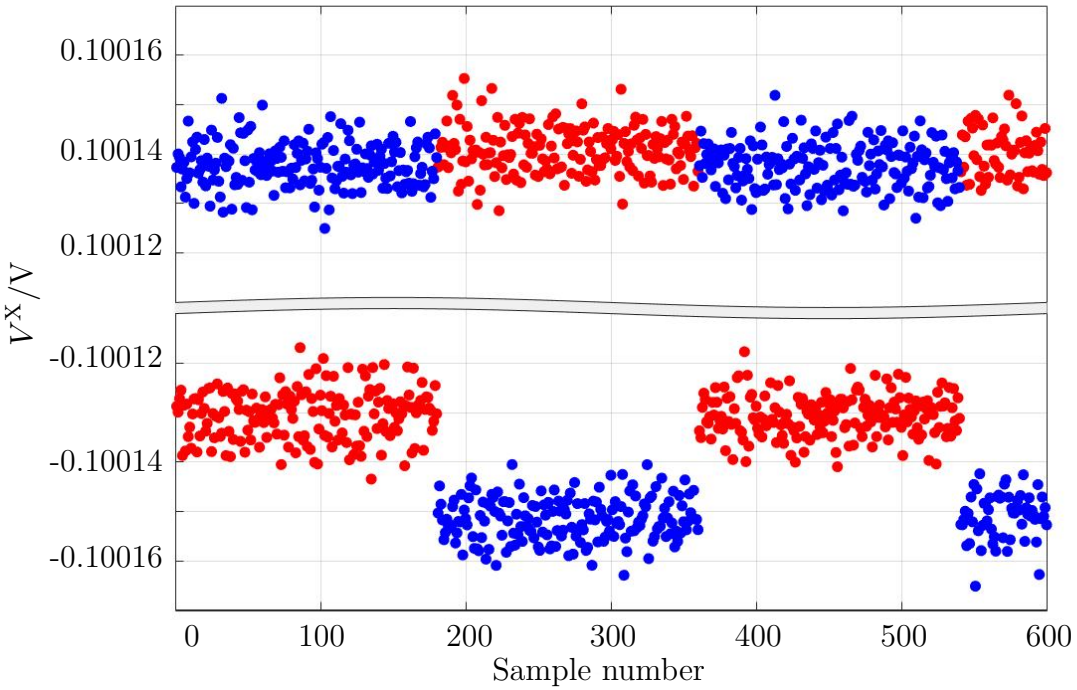

Figure 6.12: Plot of the reconstructed voltage V^{X} produced by the ULCAs: (•) corresponds to V^{RED}, while (•) represents V^{BLUE}.

$$V_{\kappa,l}^{\mathrm{BLUE}} = \Delta V_{\kappa,l}^{\mathrm{BLUE}} - (-1)^{\kappa} V_{\mathrm{J}}, \tag{6.5}$$

where $V_{\mathrm{J}} = |V_{\mathrm{J}}^{\mathrm{X}}|$, constant. An example of $V_{\kappa,l}^{\mathrm{X}}$ is shown in figure 6.12.

The current readings of the ULCAs can be defined as

$$I_{\kappa,l}^{\mathrm{X}} = \frac{V_{\kappa,l}^{\mathrm{X}}}{A_{\mathrm{TR}}^{\mathrm{X}}(T_{\kappa,l}^{\mathrm{X}})}, \tag{6.6}$$

where $A_{\mathrm{TR}}^{\mathrm{X}}(T_{\kappa,l}^{\mathrm{X}})$ is the gain of ULCAs corrected by the amplifier temperature $T_{\kappa,l}^{\mathrm{X}}$, recorded synchronously from the ULCA temperature sensors. Figure 6.13 presents the samples $I_{\kappa,l}^{\mathrm{X}}$: the offset affecting the data compared to the nominal value $|I_{\mathrm{DS}}^{\mathrm{nom}}| = |ef| = 100.136\,031\,\mathrm{pA}$[6] is visible.

From $I_{\kappa,l}^{\mathrm{X}}$, the following average sequences, with $q = 1, \ldots, Q = K/2 - 1$ are

[6]Here and in the following, the conventional value $e_{90} = \frac{2}{R_{\mathrm{K-90}} K_{\mathrm{J-90}}}$ of the elementary charge is considered. The usage of e_{90} is necessary to provide consistency to the measurement since for the calibration of the output voltage of the PJVSs and of the transresistance gain A_{TR} of both the ULCAs, the conventional values $R_{\mathrm{K-90}}$, and $K_{\mathrm{J-90}}$ are employed.

computed:

$$\bar{I}_q^{\mathrm{X}} = \frac{1}{2L}\Big[\sum_{l=\frac{L}{2}+1}^{L} I^{\mathrm{X}}_{(2q-1),l} + \sum_{l=1}^{\frac{L}{2}} I^{\mathrm{X}}_{(2q+1),l} - \sum_{l=1}^{L} I^{\mathrm{X}}_{(2q),l}\Big]. \tag{6.7}$$

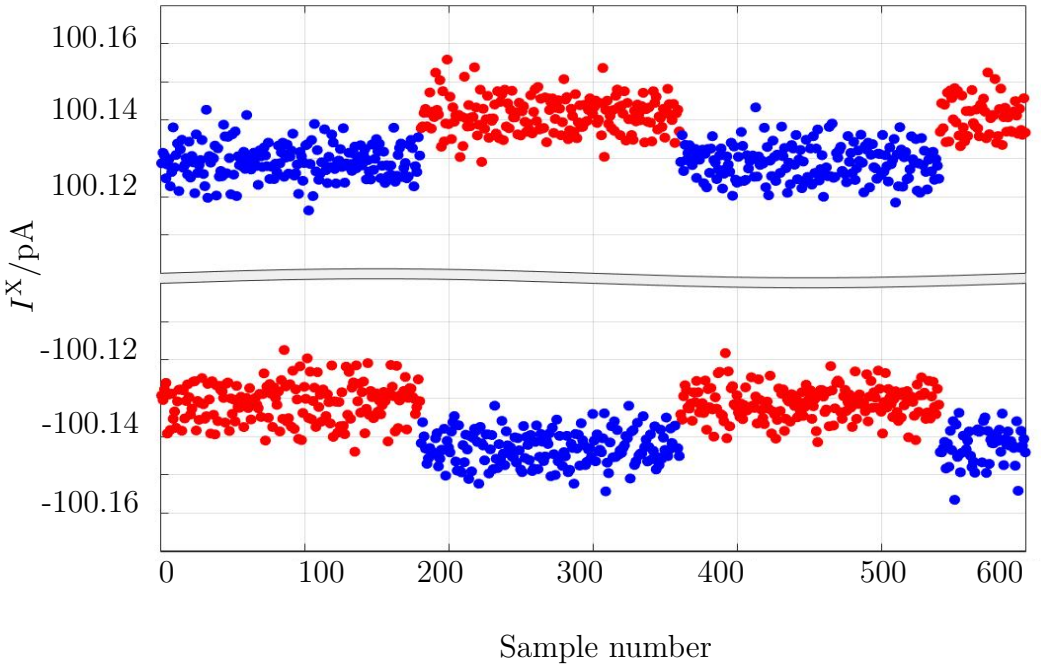

Figure 6.13: Plot of the current I^{X} measured by the ULCAs: (●) corresponds to I^{RED} while (●) represents I^{BLUE}.

These sequences are further averaged as

$$\bar{I}_q = \frac{1}{2}(\bar{I}_q^{\mathrm{BLUE}} - \bar{I}_q^{\mathrm{RED}}), \tag{6.8}$$

obtaining the final reading

$$\bar{I}_{\mathrm{DS}}^{\mathrm{read}} = \frac{1}{Q}\sum_{q=1}^{Q} \bar{I}_q. \tag{6.9}$$

The relative deviation $\delta\bar{I}_{\mathrm{DS}}$ from the nominal value is

$$\delta\bar{I}_{\mathrm{DS}} = \frac{\bar{I}_{\mathrm{DS}}^{\mathrm{read}}}{I_{\mathrm{DS}}^{\mathrm{nom}}} - 1. \tag{6.10}$$

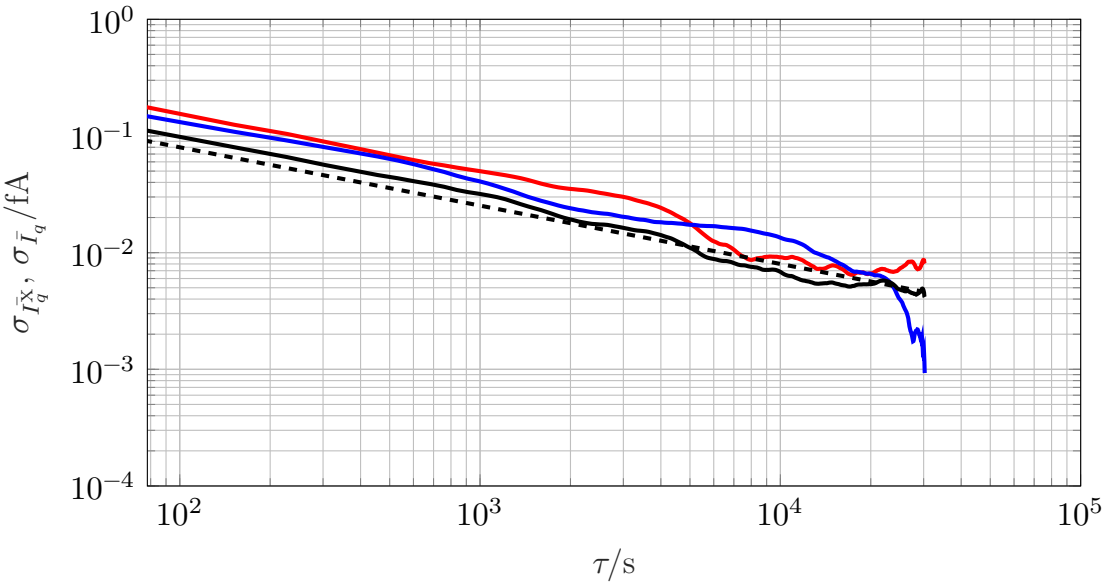

Figure 6.14: Allan deviation of $\bar{I}_q^{\mathrm{X}}$ and $\bar{I}_q$ estimated on a 16 h measurement. (—) represents the Allan deviation derived from $\bar{I}_q^{\mathrm{RED}}$, (—) is the Allan deviation evaluated from $\bar{I}_q^{\mathrm{BLUE}}$ and (—) is the Allan deviation estimated on $\bar{I}_q$. For all of the three curves the region in which the fit was performed is highlighted.

6.6 Final results

A 16 h measurement yielded $\delta\bar{I}_{\mathrm{DS}} = 7(9) \times 10^{-8}$ with a type A uncertainty of 3.8×10^{-8} and a preliminary type B uncertainty of 8×10^{-8}.

The Allan deviations of $\bar{I}_q^{\mathrm{X}}$ and of $\bar{I}_q$ are shown in figure 6.14. The effectiveness of the differential measurement is demonstrated by the fact that the flicker region observable in figure 6.6 is no longer present in figure 6.14.

A fitting procedure on the data of figure 6.14 gives white noise levels

$$\sigma_{\bar{I}^{\mathrm{RED}}}(\tau) \approx 1.6\ \mathrm{fA}/\sqrt{\tau/\mathrm{s}} \tag{6.11}$$

$$\sigma_{\bar{I}^{\mathrm{BLUE}}}(\tau) \approx 1.3\ \mathrm{fA}/\sqrt{\tau/\mathrm{s}} \tag{6.12}$$

$$\sigma_{\bar{I}}(\tau) \approx 0.9\ \mathrm{fA}/\sqrt{\tau/\mathrm{s}} \tag{6.13}$$

Since the value $\sigma_{\bar{I}}(\tau)$ is approximately $1/\sqrt{2}$ of $\sigma_{\bar{I}^{\mathrm{X}}}(\tau)$, it can be concluded that the two ULCA readings are uncorrelated.

Extrapolating $\sigma_{\bar{I}}(\tau)$ at 16 h, one obtains the type A uncertainty

$$u_{\mathrm{A}}(\bar{I}_{\mathrm{DS}}) = \sigma_{\bar{I}}(16\,\mathrm{h}) \approx 3.8\,\mathrm{aA}. \tag{6.14}$$

The type B uncertainty is still in phase of evaluation. A major contribution is that associated to the instability of A_{TR} [121].

The final result obtained in this work is the outcome of a measurement set-up that allowed a significant improvement compared to the one presented in [121] where, after one day of measurement time, the total relative uncertainty on the nominal current of 96 pA was 0.16 µA/A.

Compared to [121], the major contributions to this greater accuracy result are:

- The cross-switch chip, which allows the measurement of the pump by two different ULCAs without interruptions. Its presence allows to remove the current offset affecting the measurement and to double the signal-to-noise ratio with respect to an ON-OFF measurement, thus reducing the type A uncertainty.
- The two low noise ULCAs with a lower noise level.
- The two PJVs which are employed as accurate references to the potentiometric measurement of the ULCA outputs improving the accuracy of the voltage measurements.
- The new low noise cabling system of the cryogenic probe that was specifically designed to perform high accuracy current measurements of single-electron devices.

With the achievement of an uncertainty below 10^{-7}, this result represents a step forward in the adoption of the single-electron pumps as a quantum current standard.

Chapter 7

Conclusions

This PhD work is about the measurement of low currents. In particular, I worked on the characterization, calibration and improvement of the performances of two transresistance amplifiers: the FEMTO DDPCA-300 and the ULCA. The noise and the stability of the amplifiers were characterized by means of the Allan deviation, a powerful statistical tool suitable for the analysis of non-stationary noise.

For the FEMTO DDPCA-300, it was developed and implemented a specialized temperature controller to improve its offset stability. The resolution achieved was around 15 times better compared to that of the uncontrolled amplifier, reaching a value of 6 aA at 8200 s.

For what concerns the ULCA, an investigation showed how the amplifier achieves its best operating condition when shielded together with the coaxial cable into a Mu-metal box. In fact, the corresponding Allan deviation shows a resolution which is four times better than the one obtained under the other experimental conditions examined in chapter 3. For this reason, the same shielding configuration was employed in the single-electron experiment set-up described in chapter 6.

The gain of the two amplifiers was also calibrated employing different methods: the FEMTO DDPCA-300 was calibrated with the capacitance-charging method, the ULCA by means of a 14 bit CCC.

The set-up used for the calibration of the FEMTO DDPCA-300 was designed and built to generate currents in the range from 100 fA to 100 pA. Its usage can be extended also to other transresistance amplifiers suitable for low DC current measurements. Since the set-up exploits the capacitance-charging method, only the traceability to the units of capacitance and time is required and not, as the majority of the methods usually employed, also to the unit of voltage. The accuracy obtained with this calibration set-up is of the order of 10^{-5}. The calibration set-up and the experimental results were published in [141].

Regarding the ULCA calibration, the procedure described in chapter 4 employs a 14 bit CCC for the separate calibration of both its input and output stages. The two calibrations are then combined to obtained the overall transresistance gain

A_{TR}: the relative calibration uncertainty is of the order of 10^{-8}.

As final application, I measured the low current produced by a single-electron pump. The peculiarity of this kind of devices is the ability to transfer an integer number of elementary charges in a controlled way. For this reason, they are a possible realisations of the ampere in the revised SI, which will be finally implemented on 20 May 2019.

To realize a quantum current standard, the current produced by single-electron pumps should fulfil two requirements: having at least a magnitude of 100 pA and a relative error of 10^{-7} or lower.

The device I measured was a GaAs/AlGaAs pump performing the single parameter pumping process. The operating frequency was 625 MHz which generated a nominal current of 100 pA in case the pump is transferring one electron per period.

In order to fulfil the requirement of measuring the current with high accuracy, the experimental set-up was upgraded with respect to that of [121].

First of all, an additional heterostructure to be integrated with the pump, the cross-switch chip, was designed and fabricated to perform non-stop measurements and remove the current offsets. Then, the cabling system of the cryogenic probe was totally redesigned to allow the potentiometric measurement of the pump current by a couple of ULCAs and PJVSs.

As reported in chapter 6, after a 16 h measurement, the relative deviation between $I_{\mathrm{DS}}^{\mathrm{nom}}$ and the current produced by the pump was $\delta\bar{I}_{\mathrm{DS}} = 7(9) \times 10^{-8}$. Even if the type B uncertainty is still in phase of evaluation, a preliminary value mainly related to the instability of ULCA transresistance gains was considered as in [121]. The ability to measure the current with an uncertainty lower than 1.6×10^{-7} [121] demonstrates that the adopted measuring method led to an improvement over the state of the art.

Even if a further reduction of the type A uncertainty can be expected by performing longer measurements (which can be extended up to 24 hours due to the maintenance of the dilution refrigerator), the uncertainty budget of these measurements is limited by the gain stability of the ULCAs. Anyway, this work is a confirmation of the experimental progress made to meet the requirements for having a primary metrological quantum current standard.

Appendix A

A.1 DC and AC Josephson effect

The DC and AC Josephson effects were predicted in 1962 by Brian Josephson and describe the phenomenon of the tunneling of electron pairs called *Cooper pairs* from one superconductor to another which is weakly coupled with the first through a thin barrier of insulator [134]. This charge movement generates a supercurrent across the so-called *Josephson junction*. The Josephson junctions are mainly realized using Superconductor-Insulator-Superconductor (SIS) junctions or Superconductor-Normal metal-Superconductor (SNS) junctions.

The DC Josephson effect consists in the flowing of a DC supercurrent through a Josephson junction even if zero voltage is applied across it. This supercurrent can be described as

$$I(t) = I_{\mathrm{C}} \sin \varphi(t), \tag{A.1}$$

where I_{C} is the critical current, i. e. the maximum value of supercurrent that can flow across the junction, while $\varphi(t)$ is the phase difference between the two quantum mechanical waveforms of the superconducting states in the left and right superconductor respectively.

The AC Josephson effect predicts how, having a finite voltage V applied across the junction, the usual DC current appears but there is also an additional AC supercurrent with a frequency

$$f_{\mathrm{J}} = \frac{2e}{h} V, \tag{A.2}$$

where e is the electronic charge and h is the Planck constant.

The frequency f_J can be modulated with an external signal at frequency f_{e}, usually in the microwave spectrum. The result is a non-linear voltage-current behaviour of the junction that shows constants steps of voltage

$$V_n = n \frac{h}{2e} f_{\mathrm{e}} = n \Phi_0 f_{\mathrm{e}}, \tag{A.3}$$

with n=1, 2, 3.. is the integer number of steps and Φ_0 is the magnetic flux quantum.

These steps were observed by S. Shapiro in 1963 therefore they are also called *Shapiro steps* [86].

Equation (A.3) can be written using the Josephson constant

$$K_{\mathrm{J}} = (h/2e)^{-1} = (\Phi_0)^{-1}. \tag{A.4}$$

Therefore

$$V_n = n\frac{f_{\mathrm{e}}}{K_{\mathrm{J}}}, \tag{A.5}$$

where K_{J} is defined since 1990 as $K_{\mathrm{J-90}}$=483 597.9 GHz/V.

Thanks to the AC Josephson effect it is possible to link two units of measure as the frequency and the volt. Considering that the frequency is already defined by using the caesium standard [85] with an accuracy of one part in 10^{12}, since the 1970s the AC Josephson effect was exploited to define a metrological standard for the volt, so-called Josephson Voltage Standard (JVS), by using the Shapiro steps as a reference [137].

At the beginning of the Josephson effect discovery, small DC output voltages of tens of millivolts were produced; in order to increase the level of the voltage produced, arrays of Josephson junctions connected in series were produced and uniformly irradiated with external microwaves [96]. With 1484 Josephson junctions it is possible to produce a stable and quantized voltage at 1 V level by exposing the junctions to 72 GHz and generating a number of around 8000 voltage steps [88]. Moreover, by irradiating 14184 Josephson junctions with microwaves at the same frequency, it is possible to increase the voltage produced to 10 V achievable in 150000 quantized voltage levels [89].

Resistively-capacitively-shunted-junction model The characteristic behaviour of a Josephson junction can be described with the *resistively-capacitively-shunted-junction* model (RCSJ model) [91, 90]. In this model, the real Josephson junction can be represented as a circuit with a conducting resistance R_{N}, a capacitor C and an ideal Josephson junction in parallel. Thanks to the Stewart-McCumber parameter β_C, which depends on R_{N}, C and I_{C}, a classification of the junction can be done.

If $\beta_C > 1$ the junction is underdamped and in case of strongly underdamped condition ($\beta_C \gg 1$) the junction has a hysteretic behaviour in the I-V plot without the exposure to microwave irradiation. Under irradiation, the junction presents multiple Shapiro steps corresponding to the same bias current.

If $\beta_C \leq 1$ the junction is overdamped, i. e. the junction shows just a single plateau in the I-V characteristic. When the junction is irradiated multiple steps with constant voltage are induced. In particular, it was found that suitable overdamped junctions are made of Superconductor-Normal metal-Superconductor (SNS) [93] and Superconductor-Insulator-Normal metal-Insulator-Superconductor

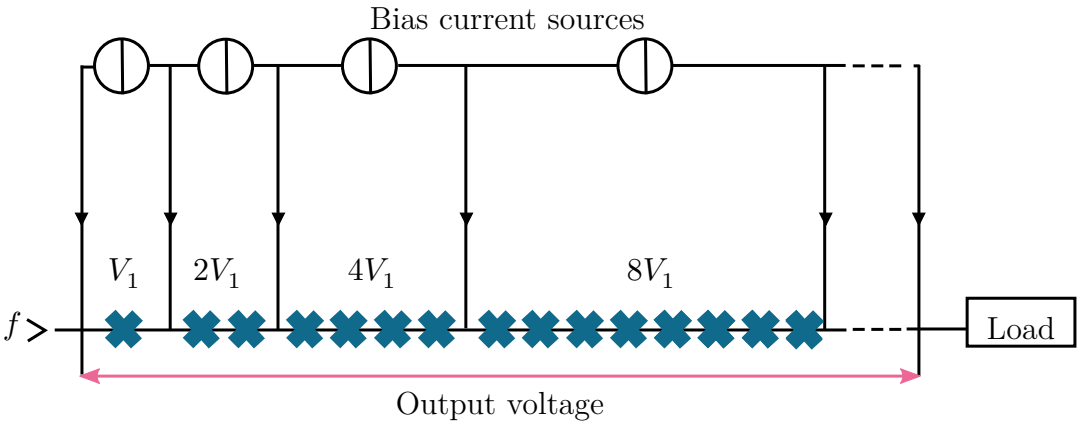

Figure A.1: Schematic circuit of a Josephson array binary segmented (PJVS).

(SINIS) [94]. In [87], figure 1, the categories in which the Josephson junctions can be distinguished are well represented.

A.1.1 Programmable Josephson voltage standard (PJVS)

In order to select the voltage steps in a quick and precise manner, a new circuit was developed to program the voltage output of a Josephson array. The system is based on overdamped Josephson junctions divided in a binary sequence of arrays (segments) with an independent biasing. Each segment is irradiated with a microwave at frequency f.

As shown in figure A.1, by applying a bias current to the appropriate segments it can be generated an arbitrary output voltage which is the sum of the voltages developed by each junction in the segments. Since the number of junctions is programmed to rapidly change during the time, the voltage $U(t)$ is produced. It can be described as

$$U(t) = nM(t)f/K_{\mathrm{J}}, \tag{A.6}$$

being f the microwave frequency, M an integer number from 0 to the total number of the junctions in the array, and n the order of Shapiro steps (usually $n = 0, \pm 1$).

Therefore, it is possible to obtain an array which is a digital to analog converter with a fundamental precision [92]. This kind of arrays is called *programmable Josephson arrays* or *programmable Josephson voltage standards* (PJVSs). In particular, a PJVS can be employed to generate AC waveforms by switching rapidly the quantized steps of the Josephson junctions.

The accuracy of a PJVS was proved by comparing the output voltages with a conventional Josephson voltage standard. The agreement found between the two systems at 1 V was around parts in 10^{-10} [124, 125].

PJVSs employed in the PTB experiment

In the single-electron experiment described in chapter 6, two PJVSs were employed.

The PJVSs consist of two Josephson arrays made by 8192 SINIS Josephson junctions each, mounted on two chips with an area of 1 cm^2 and placed at the end of a cryogenic probe in a can of liquid helium at 4.2 K. They use an irradiation source at approximately 70 GHz: this leads the voltage amplitude of each array up to 1.2 V in steps of around 145 µV.

A picture of the system composed of the two PJVSs can be seen in figure A.2. The microwave source (L) generates a signal of 70 GHz which is split in two to reach the two arrays at the bottom of the probe inserted into the helium can (Q). The microwave source is connected to an EIP 578B Source Locking Counter (P) which sets the frequency of the signal to be generated. The EIP 578B takes a clean reference signal from an Agilent 33210A 10 MHz Function Generator (N) synchronized with the 10 MHz reference signal of the atomic clock. Two custom-made sources (R) generating the current bias for the two arrays are employed. The sources are powered by a double voltage source Voltcraft VLP-2403 PRO (S). The complete system is controlled remotely via an IEEE-488 bus by a PC.

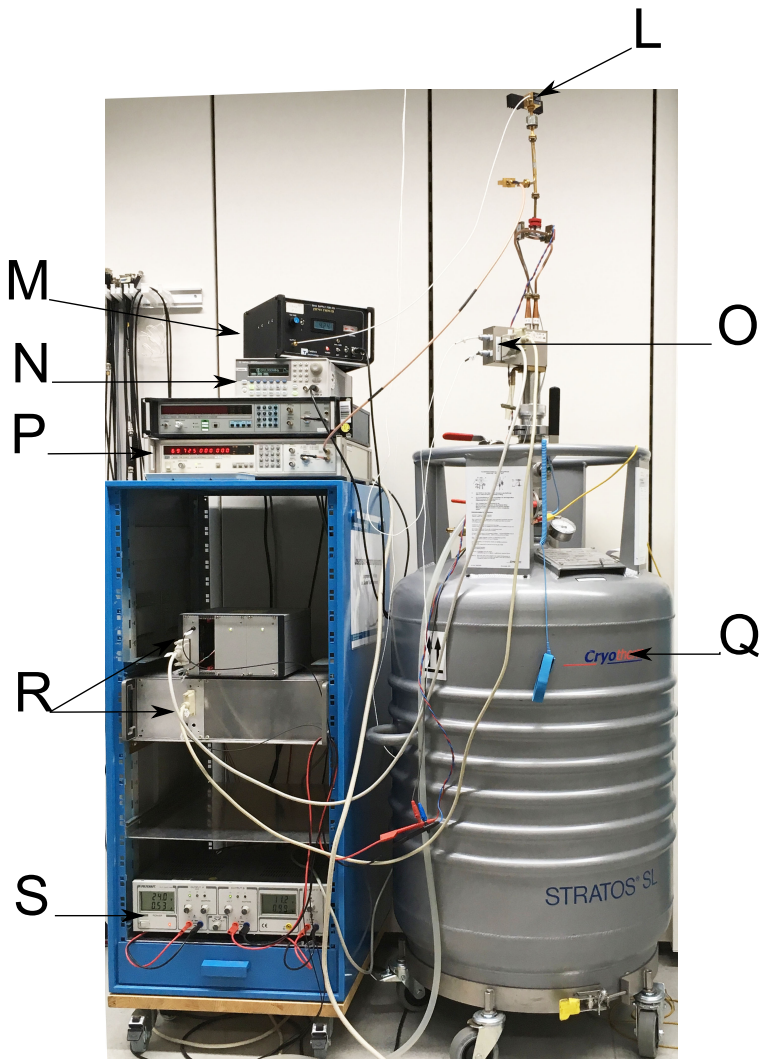

Figure A.2: Picture of the two PJVS system with 1 V output showing the microwave source (L) and its power supply (M), the waveform generator (N), the two output voltage signals from the PJVSs (O), the microwave counter (P), the can of liquid helium in which the Josephson arrays are cooled down (Q), the electronic for the bias (R) and the power supply for electronic (S).

Appendix B

B.1 Dilution refrigerators

To show the quantized current behaviour, single-electron devices require an operating temperature in the sub-kelvin region: for this purpose *dilution refrigerators* are employed. This name comes from their cooling power based on the mixing of two isotopes of helium: ^{3}He and ^{4}He.

In the so-called *mixing chamber*, the base temperature of the refrigerator is reached exploiting the phase transition of the isotopes mixture below the critical temperature of around 0.8 mK. In fact, under this temperature, the mixture separates into two liquid phases, which, due to the different densities of the isotopes, are floating one on top of the other. The one on top is called *concentrated phase* because of its richness in ^{3}He, while the other, rich in ^{4}He, is called *diluted phase*. By means of local heating of the dilute phase, some of the ^{3}He isotopes are removed from the mixing chamber: to restore the equilibrium ^{3}He isotopes migrate from the concentrated phase in the diluted phase. The energy necessary to transfer the isotopes from one phase to the other provides the cooling capacity of the refrigerator.

Thanks to this principle, dilution refrigerators represent the most important technology to reach the temperature interval between 1 K and 5 mK, and they are the only option to provide continuous refrigeration below 0.3 K [127].

Two types of dilution refrigerators are available: the *wet* and the *dry* ones. Since wet refrigerators require a pre-cooling and a purification of the ^{3}He entering in the cooling circuit, they do not need a pulse tube cryo-cooler as the dry ones. In this way, measurements performed in wet refrigerators are not affected by strong vibrations coming from the pulse tube, which can influence the results of high precision and high accuracy experiments.

For this reason, a wet dilution refrigerator produced by Oxford Instruments was employed to perform high accuracy measurements on single-electron pumps: the "KelvinoxTLM" dilution refrigerator.

B.2 The KelvinoxTLM dilution refrigerator

The KelvinoxTLM is a wet dilution refrigerator that can reach in the mixing chamber a base temperature of around 15 mK.

The key feature of this model is the top-loading process that allows the samples to be immersed directly into the liquid mixture obtaining a better thermalization with the cryogenic environment. Moreover, the isotope mixture cannot be removed during the process of unloading the sample, avoiding the risk of leaks and reducing the operation time.

Thanks to the superconducting solenoids in correspondence of the mixing chamber, in the KelvinoxTLM it is also possible to perform experiments with a magnetic field perpendicular to the surface of the samples up to 20 T.

B.3 New probe design

The overall length of the KELTLM34 Melcher probe 4 is 285.5 cm with a diameter that spans from 5 cm (maximum in the upper part) to approximately 3.5 cm (minimum at the bottom part). Its structure can be divided in four main parts which are listed below and represented in figure B.1: the correspondent length of each part is reported in table B.1.

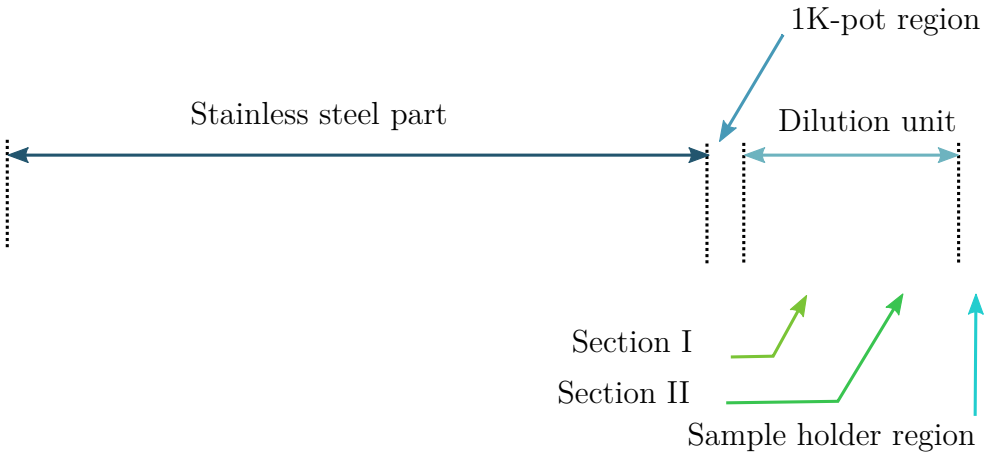

Figure B.1: Drawing of the KELTLM34 Melcher probe 4.

Stainless steel part It begins with a vacuum-tight top flange and ends in the 1K-pot region. Thus, it covers a temperature span ranging from room temperature to around 1 K. The stainless steel part is composed by two elements, one sliding into the other: it is necessary for the top-loading of the sample into the refrigerator. A valve allows to keep in vacuum all the inner part of the probe, including the sample, while the experiment is running.

Table B.1: Length of the main components of the TLM probe.

Part		Length/cm
Stainless steel part		210
1K pot region		12
Dilution unit	Section I	29
	Section II	30
Sample holder		3

1K-pot region Once the probe is inserted in the dilution refrigerator, this region corresponds to the 1K-pot part of the refrigerator, maintained ad approximately 1 K. The 1K-pot region is also made of stainless steel and it presents a cavity of 9 cm long and with a diameter of 3 cm (figure B.2 (a)). This cavity can be exploited to thermalize all the cabling system at around 1 kelvin before reaching lower temperature. This is done by means of the thermalization box, see section B.4.4.

Dilution unit When the probe is cooled down, the temperature across this part ranges from 700 mK to few mK, which is the refrigerator base temperature. The lowest section of the dilution unit is inserted directly into the isotope mixture and placed in correspondence of the superconducting magnets. For this reason it is made of glass fiber to avoid disturbances and interferences across the magnetic field region. The dilution unit can be separated in two different parts, both protected by a shell made of two half-cilindric sections of fiber glass fixed in place by brass screws. These parts are

1. **Section I** is a cilindric-shape part fully made of glass fiber blocks without any space between them.
2. **Section II** is also made of glass fiber blocks, and is separated by around 3 cm of empty space from the Section I. It also offers an empty region in which is placed the connector of the 24 DC lines (figure B.2 (b)). At the end part of the Section II is mounted the the sample holder.

Sample holder It is made of copper brass plated to increase the thermal diffusion and prevent the oxidation of the metal. The sample holder is made by three different parts especially designed to be integrated at the lower part of the dilution unit (figure B.3).

(a) Picture of the 1K-pot region. It is also shown the cavity used to thermalize the cables with the first prototype of thermalization box (section B.4.4).

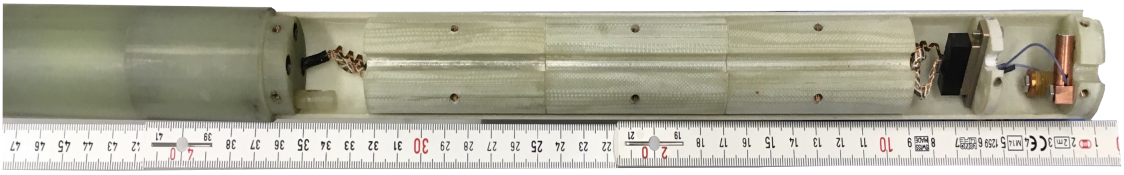

(b) Picture of the Section II of the dilution unit with the connector for the 24-DC lines. At the end there are also the RuO_2 thermometer and the heater for controlling the temperature on the sample.

Figure B.2: Picture showing details of the probe before the installation of the new cabling system.

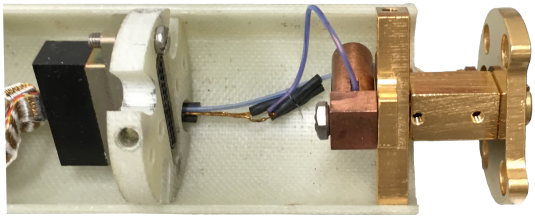

Figure B.3: Sample holder mounted at the end of the Section II.

B.4 New cabling system

B.4.1 RF lines

Cables employed As shown in figure B.4, the Elspec stainless steel cables were used in two regions of the probe cabling system: between the top flange until the beginning of the 1K-pot region and across the overall dilution unit until

the sample holder (figure B.5). On the other hand, the NbTi cables were employed across the 1K-pot region. To avoid the thermal expansion of the PTFE insulating the cables, both the types of cables were tempered before being installed in the probe.

The specifications of the cables are reported in table B.2, while the lengths of the single cables are listed in table B.3.

Figure B.4: Scheme of the RF line assembly: in light blue is represented the position of the stainless steel cables while in blue the location of the NiTi cables.

Connectors The connectors chosen are the Huber+Suhner Sub-Miniature version A (SMA) male and the Huber+Suhner Sub-Miniature Push-on (SMP).

Due to a lack in the Elspec cables length, the final segments across the dilution unit were divided in two parts in correspondence of the empty space between Section I and Section II. For this reason, an SMA adaptor Rosenberger female-female 32K601-K00L5 with 50 Ω impedance was used for line A, while for line B, an SMA female-female adaptor 32K101-K00L5 with 50 Ω impedance was employed (figure B.5).

B.4.2 Signal lines

Cables employed As shown in figure B.6, line RED and BLUE were both made by Lemo cables running from the top flange to around the half of the stainless steel part, then semi-rigid Thermocoax® cables were connected to reach the 1K-pot region. In the thermal box, the Thermocoax® were connected to NbTi

Figure B.5: Picture of the line A (top) and line B (bottom) in the Section II. In the picture are clearly visible the SMA (left) and SMP (right) connectors and two adaptors.

wires as thermal decoupler. After that, other Thermocoax® were used until Section II. For the last part of the Section II two short Lemo cables were used as adaptors to be plugged directly in the PCB sample holder. The specification of the coaxial cables are reported in table B.4, while the lengths of the single cables are listed in table B.5.

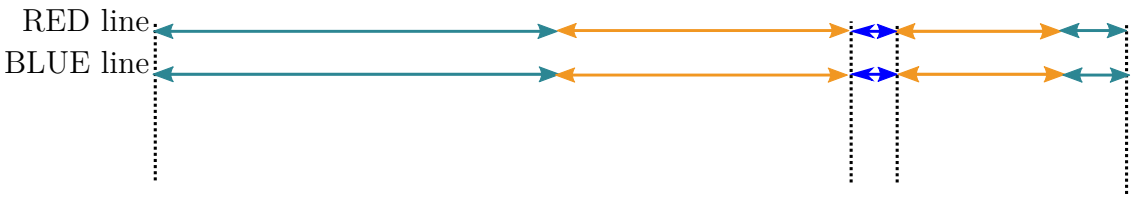

Figure B.6: Scheme of the signal line assembly: in green are represented the Lemo cables, in orange the Thermocoax® and in blue the NiTi wires.

Connectors The connectors used for the Lemo cables in the upper part of the probe are Huber+Suhner SMA male and Rosenberger Micro coaxial connector (MCX) female, both of them with 50 Ω impedance.

The Thermocoax® mount by default their MCX male connectors at both ends: for this reason the NbTi wires, placed inside the thermalization box, have MCX female connectors (figure B.10).

The Lemo cables across the last part of the Section II are equipped with Rosenberger MCX female connectors and with Huber+Suhner SMP to be plugged into the sample holder PCB (figure B.7).

B.4.3 24 DC lines

As shown in figure B.8, the 24 DC lines were filtered by means of the low-pass filter PCB and they are terminating on the sample holder, where the single-electron

Figure B.7: Picture of the signal lines and the 24 DC lines. For what concerns the signal lines are visible the wrapped Thermocoax® and the Lemo cables reaching the sample holder. For the 24 DC lines the woven loom wires and the connector are shown.

pump will be placed (figure B.9).

Figure B.8: Picture of the terminal part of the probe. It shows the RF lines (bottom), the signal lines (top), the low-pass filter PCB and the sample holder.

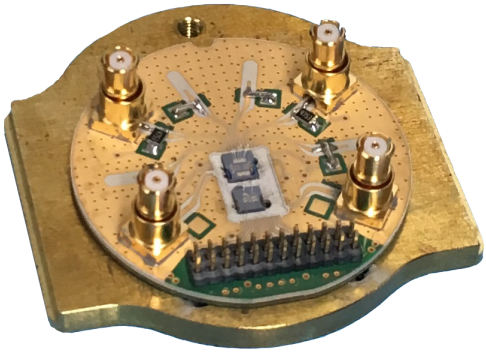

Figure B.9: Detail of the sample holder with, in the middle, the single-electron pump (on top) and the cross switch chip (bottom) bonded on it. On the top of the sample holder are shown the MCX female connectors dedicated to the ULCA lines. The same connectors on the bottom are used for the RF lines while the pins are devoted for plugging the low-pass filter PCB directly on the sample holder.

B.4.4 Thermalization Box

The purpose of this box, installed in the cavity of the 1K-pot region, is to provide a place where the cables can be thermally anchored to reduce their heat load before reaching the sample holder.

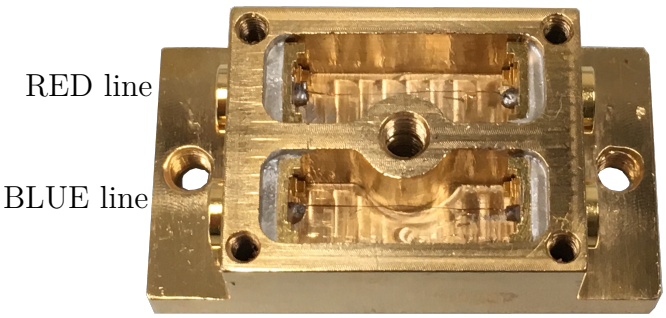

Figure B.10: Picture of the NbTi wires of both the signal lines in the thermalization box. The MCX connectors for the Thermocoax® cables are visible on both sides of the box.

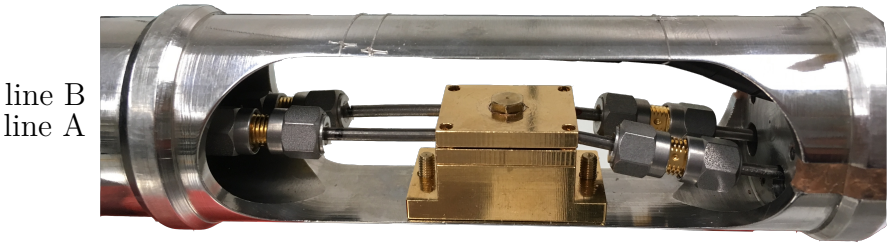

Figure B.11: Picture of the thermalization box placed in the cavity. It shows also the RF lines NbTi cables passing through its upper part.

It is made by copper brass plated and it is divided in two sections: the top part is dedicated to the thermalization of the RF lines, while the bottom is for the signal lines. It is placed in correspondence of the NbTi cables/wires both for the RF lines and signal lines (figure B.10). As shown in figure B.11, the NbTi cables of the HF lines were slightly bended to ensures more flexibility of the HF lines in case of thermal compression or expansion during the cooling down or warming up processes.

After installing the thermalization box, all the holes in the 1K-pot cavity were closed with small brass plates and the remaining chink filled with plasticine to increase the thermal impedance. After that all the cavity was wrapped in mylar tape to reduce the thermal dispersion.

B.5 Bedea coaxial cable

For every ULCA amplifer connected to the top of the probe, a coaxial cables Bedea MXR of 1 m length is used: the specifications are reported in table B.6).

Table B.2: Specifications of the cables employed for the RF lines.

Name		Elspec SS mod. AN50085	NbTi mod. SC-219/50
Inner conductor	Material	StCuAg	NbTi
	Diameter/mm	0.51	(0.51±0.013)
Dielectric	Material	PTFE	PTFE
	Diameter/mm	1.68	(1.67±0.0254)
Outer conductor	Material	Cu/304SS	NbTi
	Diameter/mm	2.19	(2.19±0.0254)
Characteristic impedance/Ω		(50±1)	(50±2)
Cutoff frequency/GHz		61	61
Capacitance/(pF/m)		95.1	95.2
Attenuation/(dB/m) at 300 K	at 0.5 GHz:	0.45	2.7
	at 1.0 GHz:	0.64	3.9
	at 5.0 GHz:	1.51	8.6
	at 10.0 GHz:	2.21	12.2
	at 20.0 GHz:	3.29	17.3
Attenuation/(dB/m) at 4 K			>0.3
Thermal conductivity/(W cm/K)			$>2.64 \times 10^{-5}$

Table B.3: Semi-rigid coaxial cables lengths for the RF lines.

Line	Type of cable	Length/cm
A	Elspec stainless steel	210
A	Coax Co., LTD NbTi	8
A	Elspec stainless steel	34
A	Elspec stainless steel	32
B	Elspec stainless steel	210
B	Coax Co., LTD NbTi	8
B	Elspec stainless steel	35
B	Elspec stainless steel	33

Table B.4: Specifications of the cables employed for the signal lines.

Name		Lemo mod. 280630	Thermocoax® mod. 1 Nc Ac 0.5
Inner conductor	Material	Cu strand	NiCr
	Diameter/mm	7	0.17
Dielectric		PVC	MgO powder
Outer conductor	Material	Cu wires	stainless steel
	Diameter/mm	32	0.5
Sheath		PVC	–
Capacitance/(pF/m)		100	490

Table B.5: Cable composition of the signal lines.

Line	Type of cable	Length/cm
RED, BLUE	Lemo mod. 280630	110
RED, BLUE	Thermocoax®	100
RED, BLUE	NbTi wire	1.5
RED, BLUE	Thermocoax®	100
RED, BLUE	Lemo mod. 280630	10

Table B.6: Specifications of the Bedea coaxial cables.

Name		Bedea MXR
Inner conductor	Material	Cu strand
	Diameter/mm	7
Dielectric		PE
Outer conductor	Material	Cu braid
	Diameter/mm	32
Sheath		PVC
Capacitance/(pF/m)		120

Nomenclature

Roman Symbols

2DEG Two-dimensional electron gas

304SS Stainless steel grade 304

BIPM Bureau international des poids et mesures

CGPM Conférence générale des poids et mesures

CIPM Comité international des poids et mesures

CODATA Committee on Data for Science and Technology

CrAu Chromium-gold

CrSi Chromium-silicon

DC Direct current

ECCS Electron-counting capacitance standard

HF High frequency

INRiM Istituto Nazionale di Ricerca Metrologica

JVS Josephson voltage standard

LNE Laboratoire National de Métrologie et d'Essais

MCX Micro coaxial connector

MIKES Mittatekniikan keskus

NbTi Niobium-titanium

NiCr Nickel-chromium

NIST National Institute of Standards and Technology

NMI National metrology institute

op amp operational amplifier

PCB Printed circuit board

PE Polyethene

PJVS Programmable Josephson voltage standard

PTB Physikalisch-Technische Bundesanstalt

PTFE Polytetrafluoroethylene

PVC Polyvinyl chloride

QD Quantum dot

QMT Quantum metrology triangle

SEM Scanning electron microscope

SET Single-electron transport

SI Système international d'unités

SINIS Superconductor-insulator-normal metal-insulator-superconductor

SMA Sub-miniature version A

SMP Sub-miniature push-on

SNS Superconductor-normal metal-superconductor

SQUID Superconducting quantum interference device

StCuAg steel copper silver-plated

ULCA Ultrastable low-noise current amplifier

Bibliography

[1] D. W. Allan. "Statistics of atomic frequency standards". In: *Proceedings of the IEEE* 54.2 (1966), pp. 221–230.

[2] D. W. Allan. "Should the classical variance be used as a basic measure in standards metrology?" In: *IEEE Trans. Instrum. Meas.* 1001.2 (1987), pp. 646–654.

[3] D. B. Percival and A. T. Walden. *Wavelet methods for time series analysis*. Vol. 4. Cambridge university press, 2006.

[4] Donald B Percival. *On the Sample Mean and Variance of a Long Memory Process*. Tech. rep. Washington University, Seattle, 1985.

[5] D. W. Allan et al. "Time and frequency (time-domain) characterization, estimation, and prediction of precision clocks and oscillators". In: *IEEE Trans. Ultrason. Ferroelectr. Freq. Control.* 34.6 (1987), pp. 647–654.

[6] J. A. Barnes and D. W. Allan. *Variances based on data with dead time between the measurements*. Tech. rep. 1987.

[7] J. A. Barnes et al. "Characterization of frequency stability". In: *IEEE Trans. Instrum. Meas.* 1001.2 (1971), pp. 105–120.

[8] J. Beran. *Statistics for long-memory processes*. Routledge, 2017.

[9] J. Lehtinen. "Quantum fluctuations in superconducting nanostructures". ISBN: 978-951-39-5688-9. PhD thesis, p. 42. URL: http://www.jyu.fi/static/fysiikka/vaitoskirjat/2014/Lehtinen-Janne-2014.pdf.

[10] E. Mykkänen et al. "Reducing current noise in cryogenic experiments by vacuum-insulated cables". In: *Rev. Sci. Instrum.* 87.10 (2016), p. 105111.

[11] A. Rossi et al. "An accurate single-electron pump based on a highly tunable silicon quantum dot". In: *Nano Lett.* 14.6 (2014), pp. 3405–3411.

[12] G. Yamahata et al. "Gigahertz single-electron pumping in silicon with an accuracy better than 9.2 parts in 10^7". In: *Appl. Phys. Lett.* 109.1 (2016), p. 013101.

[13] R. Zhao et al. "Thermal-error regime in high-accuracy gigahertz single-electron pumping". In: *Phys. Rev. Appl.* 8.4 (2017), p. 044021.

[14] R. S. Popovic and M. Lany. "Electrical measurements in nanotechnology using single electron bipolar avalanche transistors". In: *Proc. MIEL*. IEEE. 2010, pp. 51–56.

[15] G. Cheng et al. "Anomalous transport in sketched nanostructures $LaAlO_3/SrTiO_3$ at the Interface". In: *Phys. Rev. X* 3.1 (2013), p. 011021.

[16] *Variable Gain Sub Femto Ampere Current Amplifier*. Data sheet. FEMTO Messtechnik GmbH. URL: https://www.femto.de/images/pdf-dokumente/de-ddpca-300.pdf.

[17] H. Scherer et al. "Introducing Joint Research Project «Quantum Ampere» for the realisation of the new SI ampere". In: *EPJ Web of Conferences*. Vol. 77. EDP Sciences. 2014, p. 00004.

[18] D. Drung et al. "Ultrastable low-noise current amplifier: A novel device for measuring small electric currents with high accuracy". In: *Rev. Sci. Instrum.* 86.2 (2015), p. 024703.

[19] H. Scherer and B. Camarota. "Quantum metrology triangle experiments: a status review". In: *Meas. Sci. Technol.* 23.12 (2012), p. 124010.

[20] D. Drung and C. Krause. "Ultrastable low-noise current amplifiers with extended range and improved accuracy". In: *IEEE Trans. Instrum. Meas.* 66.6 (2017), pp. 1425–1432.

[21] C. Krause, D. Drung, and H. Scherer. "Measurement of sub-picoampere direct currents with uncertainties below ten attoamperes". In: *Rev. Sci. Instrum.* 88.2 (2017), p. 024711.

[22] C. Krause et al. "Noise-optimized ultrastable low-noise current amplifier". In: *Rev. Sci. Instrum.* 90.1 (2019), p. 014706.

[23] E. Enrico et al. "Simple thermal control of dc low-current amplifiers improves stability". In: *Meas. Sci. Technol.* 30.3 (2019).

[24] E. O. Göbel and U. Siegner. *Quantum Metrology: Foundation of Units and Measurements*. John Wiley & Sons, 2015.

[25] T. Gerster et al. "Robust formation of quantum dots in GaAs/AlGaAs heterostructures for single-electron metrology". In: *Metrologia* 56.1 (2018).

[26] L. Jacak, P. Hawrylak, and A. Wójs. *Quantum dots*. Springer Science & Business Media, 2013.

[27] D. Bimberg, M. Grundmann, and N. N. Ledentsov. *Quantum dot heterostructures*. John Wiley & Sons, 1999.

[28] L. P. Kouwenhoven et al. "Electron transport in quantum dots". In: *Mesoscopic electron transport*. Springer, 1997, pp. 105–214.

[29] Y. Nagamune et al. “Single electron transport and current quantization in a novel quantum dot structure”. In: *Appl. Phys. Lett.* 64.18 (1994), pp. 2379–2381.

[30] H. Van Houten et al. “Submicron conducting channels defined by shallow mesa etch in GaAs-AlGaAs heterojunctions”. In: *Appl. Phys. Lett.* 49.26 (1986), pp. 1781–1783.

[31] M. Moskalets and M. Büttiker. “Floquet scattering theory of quantum pumps”. In: *Phys. Rev. B* 66.20 (2002), p. 205320.

[32] B. Kaestner et al. “Single-parameter nonadiabatic quantized charge pumping”. In: *Phys. Rev. B* 77.15 (2008), p. 153301.

[33] S. J. Wright et al. “Enhanced current quantization in high-frequency electron pumps in a perpendicular magnetic field”. In: *Phys. Rev. B* 78.23 (2008), p. 233311.

[34] B. Kaestner et al. “Single-parameter quantized charge pumping in high magnetic fields”. In: *Appl. Phys. Lett.* 94.1 (2009), p. 012106.

[35] J. D. Fletcher et al. “Stabilization of single-electron pumps by high magnetic fields”. In: *Phys. Rev. B* 86.15 (2012), p. 155311.

[36] S. P. Giblin et al. “Towards a quantum representation of the ampere using single electron pumps”. In: *Nat. Commun.* 3 (2012), p. 930.

[37] A. Hartland. “The quantum Hall effect and resistance standards”. In: *Metrologia* 29.2 (1992), p. 175.

[38] B. Jeckelmann, A. D. Inglis, and B. Jeanneret. “Material, device, and step independence of the quantized Hall resistance”. In: *IEEE Trans. Instrum. Meas.* 44.2 (1995), pp. 269–272.

[39] F. Piquemal et al. “Fundamental electrical standards and the quantum metrological triangle”. In: *Cr. Phys.* 5.8 (2004), pp. 857–879.

[40] H. Scherer and H. W. Schumacher. “Single-electron pumps and quantum current metrology in the revised SI”. In: *Annalen der Physik* 531.5 (2019), p. 1800371.

[41] V. Kashcheyevs and J. Timoshenko. “Modeling of a tunable-barrier nonadiabatic electron pump beyond the decay cascade model”. In: *2014 Conference on Precision Electromagnetic Measurements (CPEM)*. IEEE. 2014, pp. 536–537.

[42] F. Piquemal and B. Jeckelmann. *Quantum metrology and fundamental constants*. Vol. 172. EDP Sciences, 2009.

[43] A. B. Zorin. “The thermocoax cable as the microwave frequency filter for single electron circuits”. In: *Rev. Sci. Instrum.* 66.8 (1995), pp. 4296–4300.

[44] H Dalsgaard Jensen and John M Martinis. "Accuracy of the electron pump". In: *Phys. Rev. B* 46.20 (1992), p. 13407.

[45] S. P. Giblin et al. "Evidence for robustness and universality of tunable-barrier electron pumps". In: *arXiv preprint arXiv:1901.05218* (2019).

[46] S. P. Giblin and G. Lorusso. "Exploring a new ammeter traceability route for ionisation chamber measurements". In: *arXiv preprint arXiv:1808.09217* (2018).

[47] G. Yamahata et al. "High-accuracy current generation in the nanoampere regime from a silicon single-trap electron pump". In: *Sci. Rep.* 7 (2017), p. 45137.

[48] S. P. Giblin et al. "Robust operation of a GaAs tunable barrier electron pump". In: *Metrologia* 54.3 (2017), p. 299.

[49] S. P. Giblin et al. "Error detection in a tunable-barrier electron pump". In: *arXiv preprint arXiv:1809.10249* (2018).

[50] M. Milton, J. M. Williams, and A. B. Forbes. "The quantum metrology triangle and the redefinition of the SI ampere and kilogram; analysis of a reduced set of observational equations". In: *Metrologia* 47.3 (2010), p. 279.

[51] D. B. Percival and A. T. Walden. *Spectral analysis for physical applications*. Cambridge University press, 1993.

[52] W. Poirier and F. Schopfer. *Quantum Metrology and Fundamental Constants*. Eur. Phys. J. Spec. Top. 172, 2009.

[53] L. P. Kouwenhoven et al. "Single electron charging effects in semiconductor quantum dots". In: *Z. Phys. B* 85.3 (1991), pp. 367–373.

[54] S. Nakamura et al. "Single-electron pumping by parallel SINIS turnstiles for quantum current standard". In: *IEEE Trans. Instrum. Meas.* 64.6 (2015), pp. 1696–1701.

[55] H. S. Knowles, V. F. Maisi, and J. P. Pekola. "Probing quasiparticle excitations in a hybrid single electron transistor". In: *Appl. Phys. Lett.* 100.26 (2012), p. 262601.

[56] G. Rietveld et al. "1:30000 cryogenic current comparator with optimum SQUID readout". In: *IEEE Trans. Instr. Meas.* 52.2 (2003), pp. 621–625.

[57] N. Feltin et al. "Progress in measurements of a single-electron pump by means of a CCC". In: *IEEE Trans. Instr. Meas.* 52.2 (2003), pp. 599–603.

[58] H. Scherer, J. Schurr, and F. J. Ahlers. "Electron counting capacitance standard and quantum metrology triangle experiments at PTB". In: *Metrologia* 54.3 (2017), p. 322.

[59] M. W. Keller. "Current status of the quantum metrology triangle". In: *Metrologia* 45.1 (2008), p. 102.

[60] M. W. Keller et al. "A capacitance standard based on counting electrons". In: *Science* 285.5434 (1999), pp. 1706–1709.

[61] F. Piquemal and G. Genevès. "Argument for a direct realization of the quantum metrological triangle". In: *Metrologia* 37.3 (2000), p. 207.

[62] M. W. Keller, N. M. Zimmerman, and A. L. Eichenberger. "Uncertainty budget for the NIST electron counting capacitance standard, ECCS-1". In: *Metrologia* 44.6 (2007), p. 505.

[63] M. W. Keller et al. "Accuracy of electron counting using a 7-junction electron pump". In: *Appl. Phys. Lett.* 69.12 (1996), pp. 1804–1806.

[64] M. W. Keller et al. "Metrology triangle using a Watt balance, a calculable capacitor and a single-electron tunnelling device". In: *Metrologia* 45.3 (2008), p. 330.

[65] B. Camarota et al. "Electron counting capacitance standard with an improved five-junction R-pump". In: *Metrologia* 49.1 (2011), p. 8.

[66] H. Scherer et al. "Progress towards the electron counting capacitance standard at PTB". In: *IEEE Trans.Instrum. Meas.* 58.4 (2009), pp. 997–1002.

[67] G. Rietveld, P. de la Court, and H. E. van den Brom. "Internally damped CCC for accurate measurements of small electrical currents". In: *IEEE Trans. Instr. Meas.* 58.4 (2009), pp. 1196–1201.

[68] F. Gay, F. Piquemal, and G. Geneves. "Ultralow noise current amplifier based on a cryogenic current comparator". In: *Rev. Sci. Instrum.* 71.12 (2000), pp. 4592–4595.

[69] L. Devoille et al. "Quantum metrological triangle experiment at LNE: measurements on a three-junction R-pump using a 20000: 1 winding ratio cryogenic current comparator". In: *Meas. Sci. Technol.* 23.12 (2012), p. 124011.

[70] B. M. Wood and S. Solve. "A review of Josephson comparison results". In: *Metrologia* 46.6 (2009), R13.

[71] S. J. Wright et al. "Parallel quantized charge pumping". In: *Phys. Rev. B* 80.11 (2009), p. 113303.

[72] D. V. Averin and J. P. Pekola. "Nonadiabatic charge pumping in a hybrid single-electron transistor". In: *Phys. Rev. Lett.* 101.6 (2008), p. 066801.

[73] A. Kemppinen et al. "Experimental investigation of hybrid single-electron turnstiles with high charging energy". In: *Appl. Phys. Lett.* 94.17 (2009), p. 172108.

[74] N. M. Zimmerman et al. “Error mechanisms and rates in tunable-barrier single-electron turnstiles and charge-coupled devices”. In: *J. Appl. Phys.* 96.9 (2004), pp. 5254–5266.

[75] H. Pothier et al. “Single-electron pump based on charging effects”. In: *EPL (Europhysics Letters)* 17.3 (1992), p. 249.

[76] N.-H. Kaneko, S. Nakamura, and Y. Okazaki. “A review of the quantum current standard”. In: *Meas. Sci. Technol.* 27.3 (2016), p. 032001.

[77] J. P. Pekola et al. “Hybrid single-electron transistor as a source of quantized electric current”. In: *Nat. Phys.* 4.2 (2008), p. 120.

[78] W. K. Clothier et al. “A determination of the volt”. In: *Metrologia* 26.1 (1989), p. 9.

[79] T. Funck and V. Sienknecht. “Determination of the Volt with the Improved PTB Voltage Balance”. In: *IEEE Trans. Instrum. Meas.* 40 (1991), p. 158.

[80] A. Jeffery et al. “Determination of the von Klitzing constant and the fine-structure constant through a comparison of the quantized Hall resistance and the ohm derived from the NIST calculable capacitor”. In: *Metrologia* 35.2 (1998), p. 83.

[81] B. Kaestner and V. Kashcheyevs. “Non-adiabatic quantized charge pumping with tunable-barrier quantum dots: a review of current progress”. In: *Rep. Prog. Phys.* 78.10 (2015), p. 103901.

[82] I. K. Harvey. “A precise low temperature dc ratio transformer”. In: *Rev. Sci. Instrum.* 43.11 (1972), pp. 1626–1629.

[83] K. Grohmann et al. “Current comparators with superconducting shields”. In: *Cryogenics* 14.9 (1974), pp. 499–502.

[84] B. D. Josephson. “The discovery of tunneling supercurrents”. In: *Science* 184.4136 (1974), pp. 527–530.

[85] L. Essen and J. V. L. Parry. “An atomic standard of frequency and time interval: a caesium resonator”. In: *Nature* 176.4476 (1955), p. 280.

[86] S. Shapiro. “Josephson currents in superconducting tunneling: The effect of microwaves and other observations”. In: *Phys. Rev. Lett.* 11.2 (1963), p. 80.

[87] R. Behr et al. “Development and metrological applications of Josephson arrays at PTB”. In: *Meas. Sci. Technol.* 23.12 (2012), p. 124002.

[88] C. A. Hamilton et al. “A practical Josephson voltage standard at 1 V”. In: *IEEE Electron Device Lett.* 6.12 (1985), pp. 623–625.

[89] F. L. Lloyd et al. “A Josephson array voltage standard at 10 V”. In: *IEEE Electron Device Lett.* 8.10 (1987), pp. 449–450.

[90] W. C. Stewart. "Current-voltage characteristics of Josephson junctions". In: *Appl. Phys. Lett.* 12.8 (1968), pp. 277–280.

[91] D. E. McCumber. "Effect of ac impedance on dc voltage-current characteristics of superconductor weak-link junctions". In: *J. Appl. Phys.* 39.7 (1968), pp. 3113–3118.

[92] C. A. Hamilton, C. J. Burroughs, and R. L. Kautz. "Josephson D/A converter with fundamental accuracy". In: *IEEE Trans. Instrum. Meas.* 44.2 (1995), pp. 223–225.

[93] S. P. Benz et al. "Stable 1 volt programmable voltage standard". In: *Appl. Phys. Lett.* 71.13 (1997), pp. 1866–1868.

[94] H. Schulze et al. "Design and fabrication of 10 V SINIS Josephson arrays for programmable voltage standards". In: *Supercond. Sci. Technol.* 13.9 (2000), p. 1293.

[95] J. Niemeyer, J. H. Hinken, and R. L. Kautz. "Near-zero bias arrays of Josephson tunnel junctions providing standard voltages up to 1 V". In: *IEEE Trans. Instrum. Meas.* 34.2 (1985), pp. 185–187.

[96] R. Pöpel. "The Josephson effect and voltage standards". In: *Metrologia* 29.2 (1992), p. 153.

[97] *Keysight 3458A Multimeter Shattering performance barriers of speed and accuracy*. Data sheet. Keysight Technology, 2014. URL: http://literature.cdn.keysight.com/litweb/pdf/5965-4971E.pdf.

[98] R. Behr et al. "Direct comparison of a 1 V Josephson arbitrary waveform synthesizer and an ac quantum voltmeter". In: *Metrologia* 52.4 (2015), p. 528.

[99] H. L. Störmer et al. "Two-dimensional electron gas at a semiconductor-semiconductor interface". In: *Solid State Commun.* 29.10 (1979), pp. 705–709.

[100] D. Drung et al. "Validation of the ultrastable low-noise current amplifier as travelling standard for small direct currents". In: *Metrologia* 52.6 (2015), p. 756.

[101] M. Götz, E. Pesel, and D. Drung. "A compact 14-bit cryogenic current comparator". In: *2014 Conference on Precision Electromagnetic Measurements (CPEM)*. IEEE. Aug. 24–29, 2014, pp. 684–685.

[102] M. Götz et al. "Calibrating Ultrastable Low-Noise Current Amplifiers of the 2^{nd} Generation by Means of a Cryogenic Current Comparator". In: *2018 Conference on Precision Electromagnetic Measurements (CPEM)*. IEEE. July 8–13, 2018, pp. 674–675.

[103] Martin Götz et al. “Calibrating ultrastable low-noise current amplifiers of the second generation with a cryogenic current comparator”. In: *IEEE Trans. Instrum. Meas.* (2018).

[104] F. J. Ahlers, K. Pierz, and M. Götz. “Direct comparison of fractional and integer quantized Hall resistances: Status and perspectives”. In: *2016 Conference on Precision Electromagnetic Measurements (CPEM)*. IEEE. July 10–15, 2016, pp. 1–2.

[105] D. Drung et al. “Aspects of application and calibration of a binary compensation unit for cryogenic current comparator setups”. In: *IEEE Trans. Instrum. Meas.* 62.10 (2013), pp. 2820–2827.

[106] M. Götz and D. Drung. “Stability and Performance of the Binary Compensation Unit for Cryogenic Current Comparator Bridges”. In: *IEEE Trans. Instrum. Meas.* 66.6 (2017), pp. 1467–1474.

[107] K. Grohmann et al. “Ironless cryogenic current comparators for ac and dc applications”. In: *IEEE Trans. Instrum. Meas.* 23.4 (1974), pp. 261–263.

[108] J. M. Williams and P. Kleinschmidt. “A cryogenic current comparator bridge for resistance measurements at currents of up to 100 A”. In: *IEEE Trans. Instrum. Meas.* 48.2 (1999), pp. 375–378.

[109] S. P. Giblin et al. “Scaling the current from a GHz electron pump using a CCC”. In: *2016 Conference on Precision Electromagnetic Measurements (CPEM)*. IEEE. 2016, pp. 1–2.

[110] J. Clarke and A. Braginski. *The SQUID handbook: Applications of SQUIDs and SQUID systems*. John Wiley & Sons, 2006, pp. 95–137.

[111] D. Drung et al. “Improving the traceable measurement and generation of small direct currents”. In: *IEEE Trans. Instrum. Meas.* 64.11 (2015), pp. 3021–3030.

[112] T. J. Witt. “Practical methods for treating serial correlations in experimental observations”. In: *Eur. Phys. J. Special Topics* 172.1 (2009), pp. 137–152.

[113] R. Vessot, L. Mueller, and J. Vanier. “The specification of oscillator characteristics from measurements made in the frequency domain”. In: *Proceedings of the IEEE* 54.2 (1966), pp. 199–207.

[114] D. W. Allan and J. A. Barnes. “A modified “Allan variance” with increased oscillator characterization ability”. In: *Proc. 35th Ann. Freq. Control Symposium, USAERADCOM, Ft. Monmouth, NJ 07703* (May 1981).

[115] B. Kaestner et al. “Robust single-parameter quantized charge pumping”. In: *Appl. Phys. Lett.* 92.19 (2008), p. 192106.

[116] D. B. Sullivan et al. *Characterization of clocks and oscillators*. National Institute of Standards and Technology(NIST), Technical Note, 1990.

[117] B. Kaestner et al. "Characterization of a GHz non-adiabatic single-electron pump using a cryogenic current comparator". In: *2012 Conference on Precision electromagnetic Measurements (CPEM)*. IEEE. 2012, pp. 706–707.

[118] M. Götz et al. "Improved cryogenic current comparator setup with digital current sources". In: *IEEE Trans. Instrum. and Meas.* 58.4 (2009), pp. 1176–1182.

[119] F. Stein et al. "Validation of a quantized-current source with 0.2 ppm uncertainty". In: *Appl. Phys. Lett.* 107.10 (2015), p. 103501.

[120] V. Kashcheyevs and B. Kaestner. "Universal decay cascade model for dynamic quantum dot initialization". In: *Phys. Rev. Lett.* 104.18 (2010), p. 186805.

[121] F. Stein et al. "Robustness of single-electron pumps at sub-ppm current accuracy level". In: *Metrologia* 54.1 (2016), S1.

[122] L. Dubeck and K. S. L. T. Setty. "Thermal conductivity of niobium-titanium". In: *Phys. Lett.* 27A.6 (1968), p. 334.

[123] R. Behr et al. "Josephson arrays at 70 GHz for conventional and programmable voltage standards". In: *IEEE Trans. Instrum. Meas.* 48.2 (1999), pp. 270–273.

[124] J.-P. Lo-Hive et al. "Characterization of binary Josephson series arrays of different types at BNM-LNE and comparisons with conventional SIS arrays". In: *IEEE Trans. Instrum. Meas.* 52.2 (2003), pp. 516–520.

[125] B. Jeanneret, A. Rufenacht, and C. J. Burroughs. "Comparison between the SNS and SIS Josephson voltage standards at OFMET". In: *2000 Conference on Precision Electromagnetic Measurements (CPEM)*. IEEE. May 14–19, 2000, pp. 389–390.

[126] B. Jeckelmann, B. Jeanneret, and D. Inglis. "High-precision measurements of the quantized Hall resistance: Experimental conditions for universality". In: *Phys. Rev. B* 55.19 (1997), p. 13124.

[127] F. Pobell. *Matter and methods at low temperatures*. Berlin Heilderberg: Springer Science & Business Media, 2007, p. 153. ISBN: 3-540-58572-9.

[128] M. H. Bae et al. "Precision measurement of a potential-profile tunable single-electron pump". In: *Metrologia* 52.2 (2015), p. 195.

[129] L. Callegaro et al. "Generation of reference DC currents at 1 nA level with the capacitance charging method". In: *IEEE Trans. Instr. Meas.* 63.7 (July 2014), pp. 1779–1782.

[130] L. Callegaro et al. "Techniques for traceable measurements of small currents". In: *IEEE Trans. Instr. Meas.* 56.2 (Apr. 2007), pp. 295–299.

[131] L. Callegaro, V. D'Elia, and B. Trinchera. "A current source for picoammeter calibration". In: *IEEE Trans. Instr. Meas.* 56.4 (Aug. 2007), pp. 1198–1201.

[132] R. A. Pease. "Understand capacitor soakage to optimize analog systems". In: *Electronic Design* (1982), pp. 125–129.

[133] L. Callegaro. *Electrical impedance: principles, measurement, and applications*. in Sensors. ISBN: 978-1-43-984910-1. Boca Raton, FL, USA: CRC press: Taylor & Francis, 2013.

[134] B. D. Josephson. "Possible new effects in superconductive tunnelling". In: *Phys. Lett.* 1.7 (1962), pp. 251–253.

[135] S. P. Benz and C. A. Hamilton. "Application of the Josephson effect to voltage metrology". In: *Proceedings of the IEEE* 92.10 (2004), pp. 1617–1629.

[136] I. Finardi and L. Callegaro. "Calibration setup for ultralow-current transresistance amplifiers". In: *Proceedings of Instrumentation and Measurement Technology Conference (I2MTC), 1st-6th July* (2017), pp. 774–778.

[137] B. N. Taylor et al. "On the use of the ac Josephson effect to maintain standards of electromotive force". In: *Metrologia* 3.4 (1967), p. 89.

[138] B. D. Inglis. "Frequency dependence of electrode surface effects in parallel-plate capacitors". In: *IEEE Trans. Instr. Meas.* 24 (2 June 1975), pp. 133–150.

[139] S. P. Giblin, G. D. Willenberg, and N. E. Fletcher. "Frequency dependence of gas-dielectric capacitors used in sub-nA reference current generators". In: *2010 Conference on Precision Electromagnetic Measurements (CPEM) Digest*. Daejeon, Korea, June 13–16, 2010, pp. 318–319.

[140] G. Rietveld, N.M. Zimmerman, and H.E. van den Brom. "First experimental results of the frequency dependence of a Vacuum-Gap Capacitor between 1 kHz and 0.02 Hz". In: *2012 Conference on Precision Electromagnetic Measurements (CPEM) Digest*. July 1–6, 2012, pp. 708–709.

[141] I. Finardi and L. Callegaro. "Calibration setup for ultralow-current transresistance amplifiers". In: *IEEE Trans. Instr. Meas.* 67.11 (Nov. 2018), pp. 2676–2683.

[142] G.-D. Willenberg. "EUROMET.EM-S24: Supplementary comparison of small current sources". In: *Metrologia* 50.1A (2013), p. 01002.

[143] J. F. Hersh. "A highly stable reference standard capacitor". In: *General Radio Experim.* 37.8 (1963), pp. 1–8.

[144] W. Bich and F. Pennecchi. "On the in-use uncertainty of an instrument". In: *Advanced Mathematical and Computational Tools in metrology*. Ed. by P. Ciarlini et al. Vol. VI. Singapore: Woirld Scientific, 2004, pp. 159–169.

[145] G. Rietveld et al. "1:30 000 Cryogenic Current Comparator With Optimum SQUID Readout". In: *IEEE Trans. Instr. Meas.* 52.2 (2003), pp. 621–625.

[146] G.-D. Willenberg, H. N. Tauscher, and P. Warnecke. "A traceable precision current source for currents between 100 aA and 10 pA". In: *IEEE Trans. Instr. Meas.* 52.2 (Apr. 2003), pp. 436–439.

[147] H. van den Brom, P. de la Court, and G. Rietveld. "Accurate subpicoampere current source based on a differentiating capacitor with software-controlled nonlinearity compensation". In: *IEEE Trans. Instr. Meas.* 54.2 (Apr. 2005), pp. 554–558.

[148] N. E. Fletcher et al. "New capability for generating and measuring small DC currents at NPL". In: *IEEE Trans. Instr. Meas.* 56.2 (Apr. 2007), pp. 326–330.

[149] Bureau International des Poids et Mesures. *SI Brochure: the International System of Units (SI), draft of the 9th edition*. BIPM, 2018. URL: https://www.bipm.org/utils/en/pdf/si-revised-brochure/Draft-SI-Brochure-2018.pdf.

[150] Bureau International des Poids et Mesures. *26th CGPM: resolutions adopted*. Versailles: BIPM, 2018. URL: https://www.bipm.org/utils/common/pdf/CGPM-2018/26th-CGPM-Resolutions.pdf.

[151] A. Manninen et al. "Towards direct closure of the quantum metrological triangle". In: *2008 Conference on Precision Electromagnetic Measurements Digest*. IEEE. June 8–13, 2008, pp. 630–631.

[152] Bureau International des Poids et Mesures. *SI Brochure: the International System of Units (SI)*. (Paris: Stedi Media): BIPM, 2006. URL: https://www.bipm.org/utils/common/pdf/si_brochure_8_en.pdf.

[153] Bureau International des Poids et Mesures. *Mise en pratique for the definition of the ampere and other electric units in the SI, Draft for Appendix 2 of the SI Brochure for the Revised "SI"*. BIPM, 2017. URL: https://www.bipm.org/utils/en/pdf/si-mep/MeP-a-2018.pdf.

[154] Bureau International des Poids et Mesures. *24th meeting of the General Conference on Weights and Measures. On the possible future revision of the International System of Units, the SI, resolution 1*. BIPM, 2011. URL: https://www.bipm.org/utils/en/pdf/24_CGPM_Resolution_1.pdf.

[155] M. D. Blumenthal et al. "Gigahertz quantized charge pumping". In: *Nat. Phys.* 3.5 (2007), p. 343.

[156] Bureau International des Poids et Mesures. *Comptes Rendus de la 11a CGPM*. (Paris: Gauthier-Villars): BIPM, 1961. URL: https://www.bipm.org/utils/common/pdf/CGPM/CGPM11.pdf.

[157] Bureau International des Poids et Mesures. BIPM, 2007. URL: https://www.bipm.org/en/publications/mises-en-pratique/electrical-units.html.

[158] Bureau International de Poids et Measures. *Proc. of the 25th meeting of the General Conference on Weights and Measures (November 2014)*. BIPM. Imprimerie Centrale, Luxembourg, 2015. URL: https://www.bipm.org/utils/common/pdf/CGPM/CGPM25.pdf.

[159] JCGM 200:2008. *International vocabulary of metrology — Basic and general concepts and associated terms (VIM)*. 3rd. JCGM. Paris, 2008. URL: http://www.bipm.org/en/publications/guides/vim.html.

[160] *See related material available on the BIPM web page https://www.bipm.org.* URL: https://www.bipm.org.

[161] T. J. Quinn. "Primary methods of measurement and primary standards". In: *Metrologia* 34.1 (1997), p. 61.

[162] P. Giacomo. "News from the BIPM". In: *Metrologia* 25.2 (1988), p. 113.

[163] M. J. T. Milton and T. J. Quinn. "Primary methods for the measurement of amount of substance". In: *Metrologia* 38.4 (2001), p. 289.

[164] T. J. Quinn. "News from the BIPM". In: *Metrologia* 26.1 (1989), p. 69.

[165] P. J. Mohr, B. N. Taylor, and D. B. Newell. "CODATA recommended values of the fundamental physical constants: 2010". In: *J. Phys. Chem. Ref. Data* 84.4 (2012), p. 1527.

[166] P. J. Mohr, D. B. Newell, and B. N. Taylor. "CODATA recommended values of the fundamental physical constants: 2014". In: *J. Phys. Chem. Ref. Data* 45.4 (2016), p. 043102.

[167] K. K. Likharev and A. B. Zorin. "Theory of the Bloch-wave oscillations in small Josephson junctions". In: *J. Low Temp. Phys.* 59.3-4 (1985), pp. 347–382.

[168] R. Davis. "The SI unit of mass". In: *Metrologia* 40.6 (2003), p. 299.

[169] T. J. Quinn. "The kilogram: the present state of our knowledge". In: *IEE Trans. Instrum Meas.* 40.2 (1991), pp. 81–85.

[170] B. N. Taylor. "The possible role of the fundamental constants in replacing the kilogram". In: *1990 Conference on Precision Electromagnetic Measurements(CPEM)*. IEEE. June 11–14, 1990, p. 168.

[171] I. M. Mills et al. "Redefinition of the kilogram: a decision whose time has come". In: *Metrologia* 42.2 (2005), p. 71.

This Ph.D. thesis has been typeset by means of the TEX-system facilities. The typesetting engine was LuaLATEX. The document class was `toptesi`, by Claudio Beccari, with option `tipotesi=scudo`. This class is available in every up-to-date and complete TEX-system installation.